Investigations of Higher Order Multipole Effects within the Context of Quantum Electrodynamics

James E. Frost

A thesis submitted in partial fulfilment of the requirements for the degree of Doctor of Philosophy

University of East Anglia
School of Chemistry

October 2022

Abstract

It has been known for some time that effects of terms of a higher order than the dipole can have a strong influence on the rate and efficiency of energy transfer in some systems. This led to an initial desire to investigate and understand the impact of higher order multipole terms in resonance energy transfer (RET). Towards that objective this thesis presents three different computational models developed in order to investigate such effects. In chapter two, a computational analysis of the quantum electrodynamical (QED) coupling profiles between a pair of J-aggregate dye molecules is presented. Two sets of calculations were carried out: one with and one without the inclusion of the next term beyond the dipole in the multipole expansion, namely the transition quadrupole moment. The results indicate that in some relative orientations the quadrupole terms could play an important role in accurately describing the RET process. Having explored the influence of the transition quadrupole moment computationally on a physical system, the subsequent two chapters are much more fundamental in nature, looking to analyse the characteristics of the transitions governed by a quadrupole as well as the moment itself in more detail. This is achieved through an examination of the emitted electromagnetic fields. In chapter three a novel application is produced to examine the electric field structure through its phase for dipole and quadrupole transitions in the hydrogen atom. These results provide pictorial insights into how angular momentum (AM) associated with a photon is encapsulated in the electric field. This work led to a

desire to consider similar processes using an alternative picture, namely by considering spherical fields generated using vector spherical harmonics (VSHs) in a methodology dubbed the spherical wave (SW) approach. In chapter four, an extensive analysis of the SW approach was carried out in order to create a sophisticated piece of software that was developed and the results related to previously derived analytical solutions. The new computational program offers significant new insight that addresses some of the nuances raised in chapter three. These new computational approaches provide opportunities to garner new insights into multipolar processes and address both fundamental and practical questions in optics and chemical physics.

Access Condition and Agreement

Each deposit in UEA Digital Repository is protected by copyright and other intellectual property rights, and duplication or sale of all or part of any of the Data Collections is not permitted, except that material may be duplicated by you for your research use or for educational purposes in electronic or print form. You must obtain permission from the copyright holder, usually the author, for any other use. Exceptions only apply where a deposit may be explicitly provided under a stated licence, such as a Creative Commons licence or Open Government licence.

Electronic or print copies may not be offered, whether for sale or otherwise to anyone, unless explicitly stated under a Creative Commons or Open Government license. Unauthorised reproduction, editing or reformatting for resale purposes is explicitly prohibited (except where approved by the copyright holder themselves) and UEA reserves the right to take immediate ‘take down’ action on behalf of the copyright and/or rights holder if this Access condition of the UEA Digital Repository is breached. Any material in this database has been supplied on the understanding that it is copyright material and that no quotation from the material may be published without proper acknowledgement.

Contents

List of Figures

List of Tables

Acknowledgements

First and foremost I would like to express my thanks to my primary supervisor Dr Garth Jones. Without his continued patience, guidance and general support this thesis would not have been possible. Through the ups and the downs Garth has remained optimistic and enthusiastic, constantly offering his time to provide valuable scientific and personal advice. Thank you Garth for sticking with me. I must also thank my secondary supervisor, Professor Stephen Ashworth, for encouraging me to push right through to the end. The encouragement the both of them have provided for me to persevere has been incredibly important and I will be forever grateful for their long-standing support.

Next I would like to say thank you to all the colleagues I have had the pleasure of working alongside over the years. A special thank you goes out to Dr Roger Grinter. His eagerness to engage with the work has helped make this thesis what it is. A memorable period in this PhD was getting the chance to travel and broaden my horizons through an enjoyable collaboration. I would like to express my deepest gratitude to Professor Mark T. Lusk for giving me the opportunity to work with him, as well as for supporting my application to the RSC to fund the trip. His commitment, assistance, encouragement and friendliness made it an experience I will cherish for the rest of my life. I must also thank the RSC for the award of the researcher mobility grant that allowed me to undertake the three-month research visit to Colorado School of Mines in Golden, Colorado, USA.

This PhD was made possible with the funding provided by the EPSRC. I am extremely grateful for their support. The majority of the research presented in this thesis was carried out on the High Performance Computing Cluster supported by the Research and Specialist Computing Support service at the University of East Anglia. I am thankful to the entire team for operating and maintaining the HPC as well as for providing quick and comprehensive support to my enquiries.

Finally I would like to thank and dedicate this work to the people I hold most dear: my parents. Their tireless and enduring patience, love and support are what have carried me through some of the deepest and darkest moments I have ever experienced. Thank you for your sacrifices and commitment to help see me through this PhD. Know that I am so grateful and wish for you to share in this success.

1

Introduction

1.1 Electronic Energy Transfer

Electronic (excitation) energy transfer (EET), sometimes referred to as Resonance Energy Transfer (RET), is an important process exploited in nature. While often used interchangeably, as is the case throughout this work, it is noted that the precise definitions sees RET as a specific case of the more general EET, where the separation distances preclude any significant wavefunction overlap [1]. With the complete procedure summarised in Fig. 1.1.1, EET describes the mechanism which mediates the relocation of energy from a species such as an atom, molecule, or chromophore that is in an electronically excited state (the so-called excited state donor (D)), to a nearby species which is present in its ground electronic state (the so-called acceptor (A)). As a result of this transfer of energy, the donor returns to its ground electronic state while the acceptor enters an excited state. Naturally, the acceptor then possesses the ability to behave as a donor and transfer its excited energy to another species, or, it may undergo photoluminescence through which a real photon is emitted. The whole process is only able to occur after photoexcitation of the donor via UV/visible radiation and is exemplified in nature at the start of the photosynthetic mechanism.

Photosynthesis is the complex, multi-staged process employed in the natural world to

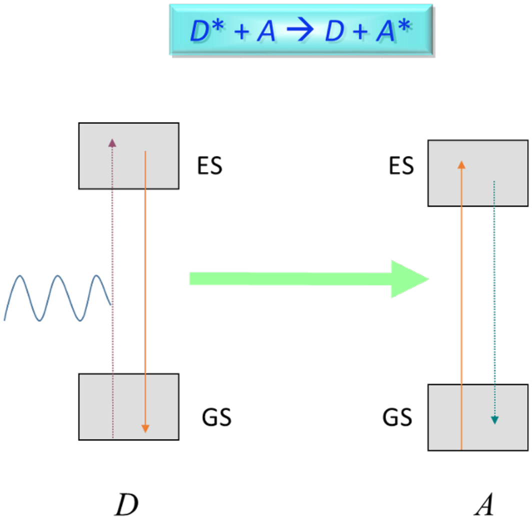

Figure 1.1.1: Schematic of the total energy transfer process. Each grey box represents an electronic state, either the ground (GS) or excited (ES) state of the donor (D) or acceptor (A). Moving from left to right, light (a photon), represented by the blue wavy line, excites the donor before the energy is transferred via a virtual photon to the acceptor, indicated by the green arrow. With each successive downward electronic transition the energy slightly decreases due to losses via intramolecular vibrations. Figure courtesy of Professor David Andrews.

generate chemical energy and synthesise complex organic molecules from light energy [2, 3]. The light energy is captured in order to drive the light-dependent reactions. It is used to excite the so-called “special pair” of chlorophyll or bacteriochlorophyll molecules with the resulting excited electron transferred to a nearby acceptor creating an initial charge separation [3, 4]. Further electron transfer reactions then take place to aid in the eventual creation of an electrochemical gradient across a biological membrane [3, 5]. This provides the energy required for the chemical reactions thereafter, as well as ultimately for nearly all life on Earth [3, 5]. All of this occurs in the reaction centre. Surrounding this hub of chemical activity are pigment protein complexes containing hundreds of chlorophyll molecules, which absorb the solar energy and transfer it to the special pair. These light-harvesting (or antenna) complexes combined with the reaction centre come together to create a photosynthetic unit [6–9]. In an excellent analogy given by Cogdell and Lindsay, the photosynthetic unit can be likened to a radiotelescope such that the light-harvesting complexes are analogous to the large collecting dish, while the reaction centre can be thought of as the transducer [9]. With this comparison in mind, it is apparent that the purpose of these antenna complexes is to increase the effective cross-sectional area of light capture for each of the individual reaction centres. Once absorbed, it is the process of EET that enables this energy to be transferred to the site where it can be exploited. This pooling of the captured light energy means the reaction centre is supplied at an enhanced rate. The antenna complexes also allow for a wider spectral range of light to be absorbed compared to the consideration of a reaction centre on its own [9]. As such, these light-harvesting complexes and EET are incredibly important for the success of photosynthesis as even in bright sunlight, the special pair on its own would only receive approximately one excitation per second [5]. These chlorophyll antenna complexes are known to increase this rate by a factor of 200–300, and it has been found that in some organisms, they are able to transfer the light energy to the reaction centre with a quantum yield of $> 90\%$ [5, 10, 11]. As a result of this high efficiency and the increasing demand for renewable energy sources, considerable research has been carried out, both experimentally and theoretically, into this remarkable process [12–16].

An important aspect to better understanding the process and mechanism behind the transfer of excited energy is to study it theoretically and generate computational models that build on the mathematical principles. This allows us to predict key facets and compare with experimental outcomes. In order to create a representative model of EET, an essential consideration is the description that is to be employed for the electronic coupling between the donor and the acceptor [17–21]. It is this coupling (or interaction) of the electronic character of the two species that serves to promote the transfer of energy between them. As pointed out by Scholes in a rather comprehensive review in 2003 on RET in molecular systems, an important distinction to be made when discussing the theory of EET is the difference between weak, intermediate and strong electronic coupling [19]. In the case of strong electronic coupling, the electronic states of the donor and the acceptor species interact to such an extent that they generate new, delocalised states [19]. As a consequence, the concept of EET between two separate entities vanishes. When it comes to discussing EET, we are primarily concerned with the weak coupling limit, where it is assumed that any coupling to a bath (surrounding environment) is greater than the coupling between the donor and the acceptor, and equilibration of the bath following excitation of the acceptor is on a timescale that is considerably faster than the energy transfer process itself [19]. This ensures that the transfer of energy is both incoherent and irreversible [19]. The description of the coupling can also be split into two separate contributions based on the distance between the interacting species, a Coulombic contribution and a so-called “short” contribution. As one would expect, the short contribution tackles the description of the coupling when the distances between the donor and the acceptor are very small, such that the primary consideration is the degree of overlap between their molecular orbitals [19]. When it comes to studying and describing systems that exhibit the EET process, the molecules are generally in close proximity, but beyond wavefunction overlap. This coupling has, for many years, been commonly represented by the theory first described by Förster back in 1948 [22] formulated for the weak coupling limit and it is assumed that this description is essentially equivalent to the purely Coulombic contribution [19]. One of the key attributes of Förster’s theory that underpins the most commonly studied and widely used form of the electronic coupling, is that this Coulombic coupling is readily approximated as a dipole–dipole interaction between the transition dipole moments of the coupling species [19, 23]. This so-called ideal dipole approximation, where the transfer of energy from a donor to an acceptor is mediated by the quantum mechanical coupling of the transition dipole moments associated with each chromophore, is widely considered to only hold when the distance between the donor and the acceptor is much larger than the size of the transition dipole moments themselves [17, 24–26]. As advances have been made, both with regard to the study of natural systems and new synthetic materials that are able to play host to the valuable process of EET, it has emerged that more accurate descriptions are required [17, 18, 24, 26–28].

1.2 EET and Molecular Quantum Electrodynamics

One of the most important aspects seen in any deviations from Förster theory, is the distance between the donor and the acceptor (as well as other molecules that may constitute the system such as the medium) and the subsequent influence this has on the coupling [24, 28–30]. This distance dependency of the EET process has recently been highlighted in work that utilised the unified theory of EET that results from the application of molecular quantum electrodynamics (QED) [31]. As the distance between the species that are set out in a rigid lattice increases, prominent differences in the coupling and exciton dynamics compared to those predicted by Förster theory are seen [31]. These differences occur as a result of terms present in the unified theory that describe the coupling between molecules over intermediate- $1/R^2$ ($1/R^4$ in terms of the rate of RET) and far-zone $1/R$ ($1/R^2$ in terms of the rate) distance regimes, which are absent in Förster theory. While the use of QED to study RET can be dated back to work by Avery in 1966, it starts with the work of Power, Zienau and Woolley and since then plenty of studies have been carried out to evolve the theory further including those by Thirunamachandran, and Craig that provided a pivotal understanding of the near- ($1/R^3$, or $1/R^6$ in terms of the rate) and far-zone mechanisms of RET [32–36]. It was the work of Andrews and colleagues that resulted in the unified theory of RET, highlighting the importance of the intermediate-zone term [37, 38]. As shown in the work by Frost and Jones, as well as other work by Lock *et al.*, this term is dominant when the distances between chromophores is of the order of the reduced wavelength, $\lambda = \frac{\lambda}{2\pi}$, of the mediating photon [31, 39]. Much more on RET and the application of QED can be found in a comprehensive review by Jones and Bradshaw [40]. The conversation will also be continued in Chapter 2 with a greater view to the application of the unified theory to the problem at hand. For now, we discuss the need for more accurate descriptions of the theory, such as that offered by QED, and also the strive to generate enhanced models of RET that better describe more varied systems. Before doing so it is noted that, while the initial motivation for the work presented here was aimed solely at RET, over time a more fundamental approach to the research being considered was taken. Even so, the theoretical description of RET from QED serves as the theory that is utilised throughout this thesis, with the difference ultimately being whether one considers a virtual photon (for a coupling interaction) or a real photon that is emitted/absorbed.

1.3 EET and the Multipole Expansion

While it is often adjudged that Förster theory and the general concept of the ideal dipole approximation is a good description of EET, it is not flawless. It is known that as the separation between chromophores decreases, deviations from the characteristic Förster $1/R^3$ distance dependence on the coupling is seen [24]. It is at these distances that traditional descriptions of the energy transfer process break down, as the ideal point dipole approximation is no longer valid and a more accurate description Coulombic interaction contribution to the electronic coupling is required. Thus, although it has proven to be useful and more often than not formed a predominantly accurate model for numerous complex systems, our attention is drawn to an important aspect that is necessary when trying to obtain a complete understanding of the RET process [19]. Recall that EET only occurs after photoexcitation of the donor. Therefore the energy that is to be transferred always corresponds to the energy difference between the ground and excited electronic states of the energised species. With this excitation of the donor, the electronic many-body wavefunction changes [41]. In order to generate a strong interpretation of the energy that is being transferred, not just know the absolute value, and to comprehend the character of the coupling species, it is the change in the wavefunction that needs to be examined [41]. One common, and useful, approach is to look at the transition density [24, 41, 42]. The (one-electron) transition density matrix associated with a transition couples the electronic excited state, e, and the electronic ground state, g, and is defined as $\rho_{eg} = |e\rangle\langle g|$ [24, 41, 42]. This equates to a superposition of the two states and a real space representation of the 3D matrix offers a visualisation of the nature of the transition in the form of a molecular orbital-like picture of the charge distribution that occurs upon excitation [24, 41, 42]. Examples of this can be found in Fig. 1 of Ref. [24] and Figs. 4 and 5 of Ref. [17]. This is the important aspect that is key to forming a detailed interpretation of EET and underpins the whole process of energy transfer. Upon interacting, the two atoms, molecules, or chromophores, "see" each other's electronic character (or "shape" as Beljonne *et al.* put it) in the form of transition densities, not well defined individual transition dipoles [24]. Thus, when referring to the coupling that promotes the process, a conceptually pleasing view is to think of it as a coupling of the transitions, rather than a coupling of the species in their respective electronic states acting as a precursor to the relocation of the excited energy.

The potential (electric) of a charge distribution at a point outside it is described by the multipole expansion, Eq. (1.3.1). As has already been mentioned, the coupling that promotes EET is commonly referred to as being a Coulombic contribution. As such it is easy to equate the interaction to a Coulombic potential energy of interaction and thus when describing electronic transitions, the transition density can be expressed in the same way, namely as an expansion of separate multipole terms,

$$P_E = \frac{1}{4\pi\varepsilon_0}\frac{q_{tot}}{r} + \frac{1}{4\pi\varepsilon_0}\frac{\mu_\alpha r_\alpha}{r^3} + \frac{1}{4\pi\varepsilon_0}\frac{\Theta_{\alpha\beta} r_\alpha r_\beta}{2r^5} + \cdots, \tag{1.3.1}$$

with μ_α and $\Theta_{\alpha\beta}$ representing the dipole and quadrupole moments respectively of a set of point charges and α and β indicating the Cartesian components through the implied summation convention. While the description of transition densities offers a conceptually pleasing perspective of what the multipole expansion is describing, one must not forget that RET is fundamentally a quantum mechanical process. As Andrews *et al.* stress, using transition densities and referring to the coupling as 'Coulombic' has the large potential to be misleading as it evokes the notion of a classical charge distribution [43]. The reality is that, for the most part, discrete transition dipole moments are involved in describing the electronic coupling [43]. It is the multipole expansion of the electronic coupling that is the subject of investigation in this work, knowing that inclusion of higher order multipoles has the ability to remedy some of the departures from Förster theory that are observed [17, 43]. These terms may provide important additions to the description of energy transfer in such cases as when dipole transitions are forbidden, as has been seen in the coupling between chlorophylls and carotenoids, whose $S_1 \leftarrow S_0$ transition is dipole forbidden, or, for systems in the condensed phase, when the distances between species are no longer large compared to the size of the chromophores [23, 28, 44]. For example, in order to generate an accurate model of energy transfer in the condensed phase, whether for synthesised materials or natural photosynthetic systems, efforts thus far have focussed on the creation of quantum mechanical methods to account for the electronic coupling when the point dipole approximation is no longer valid [17, 45–47]. Other work in the past has looked to describe the transition density through transition monopoles, however the quantum mechanical descriptions provide a more complete method for calculating the coupling [17, 48].

The higher multipole terms can readily be incorporated into the unified theory that is described further in Chapter 2 [5, 31]. With this, we present a series of computational research projects aimed at identifying the significance of the next highest order term in the multipole expansion, the transition quadrupole moment. It starts in Chapter 2 with an investigation pertaining to RET, looking at the impact this term may have. Subsequently, driven by the desire to uncover certain characteristics of a transition governed by a quadrupole moment, we shine the spotlight on the quadrupole itself by considering the electric and magnetic fields that emanate from such a transition. This is the topic of Chapters 3 and 4.

2

A Multipole Approach to EET

2.1 Introduction

In recent years, much research has been conducted into semiconductor nanocrystals or quantum dots (QDs). As a result of their tunable electronic properties, these materials have the potential to be employed in many applications, several of which utilise the process of Förster Resonance Energy Transfer (FRET) [49–51]. One particular example is for light harvesting materials or solar cells, and an important aspect in order to create efficient devices from QD species, is to understand and accurately predict the energy transfer process between them [52–54]. QDs are relatively large when compared to typical dye molecules that take part in EET, ranging from around 2 to 8 nm [27, 55]. Consequently, the distance between donor and acceptor QDs is no longer significantly larger than the size of the species — even though QDs generally only approach as close as approximately 4 nm centre-to-centre, this is comparable to their size, which is unlike the distances encountered in typical molecules that are able to carry out EET, which are often approximately 1 nm in size and 0.5 to 4 nm apart [26, 55]. Therefore, for these materials, it is generally thought that the ideal dipole approximation is no longer valid and that higher multipole contributions should be considered [26, 56]. This has led to more research into understanding and describing the energy transfer process between QDs [26, 27, 57, 58]. In one such example, the distribution of the dipole moment over the whole volume of the QD was considered, rather than using the higher order multipole terms [26]. In other work, the Förster theory was extended to treat the electronic structure of the nanocrystals, thus explicitly considering the donor and acceptor to be QDs [27]. In Ref. [27], the dipole-dipole, and dipole-quadrupole couplings were calculated on the basis of electrostatics of dielectric materials, and, although the dipole-dipole contribution was always larger than the dipole-quadrupole contribution, they found that the latter is non-negligible at short (contact) distances (2 – 5 nm) and thus concluded that these should be taken into account for a complete description [27]. As a result of this intricate interplay of the distances between QDs and the coupling and subsequent energy transfer between them, the unified theory of EET that results from the principles of QED may serve to provide a complete description of the process in QD systems. In the work by Zheng *et al.*, it was found that for distances between CdSe QDs of less than 10 nm, the point dipole approximation underestimates the resulting FRET rate [26]. In previous work that employed the unified theory in the dipole approximation, it was for these sorts of distances that it was found that the extra distance dependent terms present as compared to the coupling description developed by Förster manifested themselves [31]. Therefore, by considering the higher order terms of the multipole expansion in the Coulombic contribution to the electronic coupling in the unified theory of EET, the resultant model may prove to be effective in accurately describing the energy transfer process between QDs as a result of their larger size, and the distances commonly seen between them.

By initial consideration of the next order terms in the multipole expansion, that is the dipole-quadrupole interactions, this work aims to investigate their importance within the context of the unified theory of EET, and the possible impact they have on the coupling and subsequent exciton dynamics. Any effects that may be seen could have consequences in accurately describing energy transfer in the condensed phase, or QD systems, and may warrant further investigation into the inclusion of subsequent higher order multipole terms.

Another group of materials that have seen extensive research in recent years with respect to their optical properties are those containing lanthanide elements [59–61]. As well as offering advantages over typical FRET systems to applications such as the spectroscopic ruler and biosensing/bioimaging techniques, lanthanide materials also have the potential to create efficient solar cells [62–64]. To understand energy transfer in lanthanide compounds, a new theoretical methodology has been reported which aimed to provide insight into the $\mathrm{Ln}^{3+} \rightarrow \mathrm{Ln}^{3+}$ ET process [65]. In the work by Malta, emphasis was put on dipole-dipole, dipole-quadrupole and quadrupole-quadrupole mechanisms, while in other work by Rodrigues *et al.* it was reported that the $\mathrm{Tb}^{3+} \rightarrow \mathrm{Eu}^{3+}$ ET processes, are predominantly governed by dipole-dipole and dipole-quadrupole mechanisms [64, 65]. Considering these materials, we hope that by extending this work into a more detailed investigation of the dipole-quadrupole terms associated with the unified theory of EET, an insight into when exactly the dipole-quadrupole contributions are important will be gained. The quantum electrodynamical theory of energy transfer and the versatility of rare earth doped materials to engage in EET to higher orders beyond a donor and acceptor has already been brought to the fore in work published by Andrews *et al.* [66]. Extension of the work presented here to include lanthanides could have the potential to lead to consequences in designing efficient lanthanide based materials through consideration of the relative orientations and positions of the compounds that make up the system.

This chapter is structured in the following way. After a brief introduction, the next section gives an outline of the important aspects of the unified theory for EET in a vacuum that results from QED. Both the dipole approximation and the inclusion of the next highest order terms are discussed, with focus placed on the key elements employed in this work. In Section 2.3.1 the computational details underpinning the work that has been undertaken are provided. Finally, in Sections 2.3.2 and 2.3.3 the results are presented alongside a detailed analysis.

2.1.1 QED and the Unified Theory of Energy Transfer

For many years, it was commonly regarded that the process of energy transfer between two species separated by a distance beyond wavefunction overlap, in general occurred through one of two mechanisms [5]. The first was that described by Förster, while the second is radiative transfer which occurs over long distances, characterised by an R^{-1} distance dependence (far-zone). It is now understood that these two descriptions are merely limits to a wider portrayal that can be applied over all distances [5, 37, 38, 67, 68]. This unified theory stems from the framework of molecular quantum electrodynamics (QED) yielding the complete, correct description of EET [36, 68].

QED represents the most precise and widely applicable theory for looking at the interaction of light and matter, where both are treated quantum mechanically in a closed dynamical system [36]. Within this theory, the Coulombic interaction between the species involved in the energy transfer process comes about by the propagation of virtual photons. Virtual (as opposed to real) photons are created through vacuum fluctuations of the electric and magnetic fields leading to a non-vanishing quanta of electromagnetic field energy. The energy transfer process itself is a second-order one, whereby a virtual photon is emitted from one species and subsequently absorbed by another species. In order to determine the coupling between a donor and an acceptor, within the context of QED, the transition matrix element that connects the initial and final states of the overall system is calculated, a term that therefore contains the second-order transition operator. The result from this unified theory interestingly yields three distance dependent terms in the coupling derived after employing the dipole approximation. Two of these are consistent with the distance dependencies of the two distinct mechanisms theorised before. These are the radiative (real photon propagation) and radiation-less (virtual photon propagation) processes that are now described by the long- and short-range asymptotes, respectively [68]. The third term has an inverse square-power distance dependence, resulting in an inverse fourth-power dependence for the rate of energy transfer, which operates at an intermediate range of the distance dependence in the process of EET. From this unified theory it is seen that one mechanism seamlessly accommodates the two mechanisms that were once thought of as describing energy transfer, with no competition between the two [68].

In the multipolar formalism of QED, intermolecular interactions occur solely through the propagation of photons with electric and magnetic fields disposed orthogonally with respect to **k**, the propagation vector, and are commonly refereed to as transverse photons [36, 39, 69]. On consideration of the two limits of the different distance regimes displayed in the unified theory, it becomes useful to consider these transverse photons in relation to the intermolecular displacement vector, **R**, as differences in the coupling are observed [31, 39]. In the near-zone, any photon that is created will quickly be annihilated as a result of the short path between donor and acceptor. As a result it is strongly subject to quantum uncertainty in its vector momentum (including the direction), and subsequent summation over all its possible modes yields virtual photons with fields that are both transverse and longitudinal with respect to the intermolecular displacement vector [39]. In contrast, in the far zone, the larger distance between the species reduces the uncertainty in the direction of propagation of the photon, and longitudinal (with respect to **R**) photons no longer contribute to the intermolecular interactions. Therefore, photons with **k** closely parallel to **R** dominate, meaning the fields are now transverse with respect to both the propagation vector and intermolecular displacement vector, a characteristic associated with 'real' photons [39].

It has been shown in previous work using the dipole approximation, that the intermediate- and far-zone terms in this unified theory play non-negligible roles in describing the coupling and subsequent dynamics of energy transfer in a lattice of J-aggregate-type molecules for distances approximately greater than 5 nm [31]. Interestingly it was also shown that even at a distance of 2 nm, contributions from these extra terms were seen, however these were quickly washed-out over the 100 fs dynamic trajectories. With the species employed in the simulations placed isotropically in a brickstone lattice, contributions of photons that have electric fields transverse or longitudinal to the intermolecular displacement vector could clearly be distinguished through the coupling landscapes reported [31].

As well as offering a complete description of the energy transfer process in terms of its distance dependency, the unified theory of EET formulated by Andrews from the framework of QED, is also able to incorporate higher multipole contributions to the retarded coupling between the transition moments of two species [5, 37, 69]. In work carried out by Scholes and Andrews a detailed QED treatment of the contributions of higher order multipole moments to the coupling in vacuum is presented, alongside a discussion on the implications to the different distance regimes connected through the unified theory [69]. By considering the axial components of different transition moments for the bacteriochlorophyll *a Qy* transition, they reported that interactions involving the transition quadrupole moment would be relatively small compared to those involving the dipole and octopole moments [69]. This is consistent with the analysis and results reported by Scholes and Ghiggino, whereby considering the leading terms in the multipole expansion to be those of the dipole-dipole, dipole-octopole and octopole-octopole interactions for chromophores with dipole allowed electronic transitions, they found that the dipole-octopole contributions may often need to be considered at separations less than 1 nm [18]. In the work by Scholes and Andrews, through examination of a pair of bactriochlorophyll *a* molecules, whose angles to the intermolecular displacement vector are such that the orientation factor for the dipole-octopole coupling is approximately 8 times larger than that for the dipole-dipole coupling, they showed that for a separation less than 1 nm, the dipole-octopole coupling is stronger than the dipole-dipole coupling, while in order to calculate accurate couplings, the expansion should be taken to fairly high order for separations less than 2 nm [69]. In other work carried out by Krueger, Scholes and Fleming, a method that uses transition density cubes (TDCs) to calculate the Coulombic coupling was presented [17]. It is reported that the method can, in principle, account exactly for the shape and size of the transition density and unlike the full multipole expansion, which also accounts for the shape and size of the transition density, is valid at all molecular separations [17]. They found that, by comparing the results of the TDC method with the ideal dipole approximation, the difference in the coupling can be of the order of the coupling itself even at separations greater than 2 nm, thus suggesting the higher order terms of the multipole expansion may be significant [17].

Using the description presented in [69], the coupling of species, and the dynamics of energy transfer in a brickstone lattice currently consisting of TC ($5,5'$-dichloro-$3,3'$-disulfopropyl thiacyanine) cyanine-dye molecules (Fig. 2.1.1) represented through their transition electric dipole and quadrupole moments, are to be

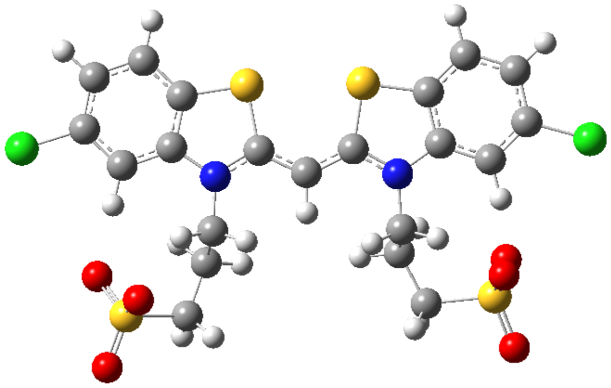

Figure 2.1.1: Structure of the TC, 5,5$'$-dichloro-3,3$'$-disulfopropyl thiacyanine, cyanine dye molecule being employed in the simulations through the use of its transition dipole and transition quadrupole moments

investigated through inclusion of the dipole-quadrupole coupling contributions to the retarded coupling between transition moments. The aim of this investigation is to determine the effect of including the dipole-quadrupole contributions on the energy transfer process as described by the unified theory of EET, before considering other higher multipole terms in an attempt to generate an accurate model of energy transfer in the condensed phase. Therefore, a comparison will be made between these results and those of simulations carried out employing the dipole-dipole coupling contributions alone. At present, the TC cyanine-dye J-aggregate model for the investigation was chosen in order to be consistent with our previous work which drew motivation from the work of Valleau *et al.* [31, 70].

2.2 Theory

The full derivation and description of the unified theory for EET which emerges from the framework of QED, as well as an investigation into the quantum pathways with which this theory describes the process may be found elsewhere [5, 37, 38, 67–69]. For completeness, the key equations and brief descriptions of the theory that are relevant to this work are given below. In order to determine the effect of the dipole-quadrupole contributions to the coupling and subsequent dynamics a comparison is required with the results of the simulations when just considering the dipole-dipole coupling. As a result this section has been split up. To start a brief description of the unified theory as a whole is given within the limits of the dipole approximation, as is consistent with the previous study conducted using this theory [31]. Following this, a description of how the theory is modified with the inclusion of the higher order multipole terms is presented.

2.2.1 The Unified Theory of Energy Transfer — Dipole Approximation

Within the multipolar formalism of QED, where intermolecular interactions are mediated by the propagation of transverse photons, the Hamiltonian for the closed dynamical system of light and matter is expressed as [5, 36]

$$H = H_{rad} + \sum_{X} H_{mol}(X) + \sum_{X} H_{int}(X), \tag{2.2.1}$$

where, $H_{mol}(X)$ is the Hamiltonian of molecule X and the summation over X implies the summation over all molecules in the system. H_{rad} is the Hamiltonian of the radiation field, Eq. (2.2.2), and $H_{int}(X)$ is the Hamiltonian describing the interaction of the radiation with the molecules, representing the coupling between the molecular subsystem and the quantized field. These interaction terms may be expressed in the electric dipole approximation, Eq. (2.2.3), however, as is discussed in the next section, higher multipole terms can readily be incorporated [5, 17, 69],

$$H_{rad} = \sum_{\mathbf{p},\lambda} a^{\dagger(\lambda)}(\mathbf{p}) a^{(\lambda)}(\mathbf{p}) \hbar c p + e_{vac}, \tag{2.2.2}$$

$$H_{int}(X) = - \varepsilon_0^{-1} \boldsymbol{\mu}(X) \cdot \mathbf{d}^{\perp}(\mathbf{R}_X). \tag{2.2.3}$$

In equation (2.2.2) the sum is taken over radiation modes with wave vector $\mathbf{p}$ and polarisation λ. The terms $a^{\dagger(\lambda)}(\mathbf{p})$ and $a^{(\lambda)}(\mathbf{p})$ are the operators for the creation and annihilation of a virtual photon, respectively, while e_{vac} is the energy of the photon vacuum. In equation (2.2.3) $\boldsymbol{\mu}(X)$ is the electric dipole operator of molecule X positioned at $\mathbf{R}_X$, while $\mathbf{d}^{\perp}(\mathbf{R}_X)$ is the electric displacement field operator.

For the energy transfer between a pair of chromophores comprising a donor (D) and an acceptor (A), the Hamiltonian given above may be simplified. When the effects of the molecules of the medium are not taken into account the Hamiltonian becomes

$$H = H_{rad} + H_{mol}(D) + H_{mol}(A) + H_{int}(D) + H_{int}(A). \tag{2.2.4}$$

In other words, this is the Hamiltonian associated with the transfer of energy between a pair of molecules in a vacuum. The initial and final state vectors of the process when energy is transferred from the excited donor to the acceptor are given by the two equations below where both are eigenvectors of the zero-order Hamiltonian, H^0,

$$|I\rangle = |D^*\rangle\,|A\rangle\,|0\rangle \qquad\qquad |F\rangle = |D\rangle\,|A^*\rangle\,|0\rangle\,. \tag{2.2.5}$$

The energies associated with these states are given by

$$E_I = e_{D^*} + e_A + e_{vac} \qquad\qquad E_F = e_D + e_{A^*} + e_{vac}, \tag{2.2.6}$$

where $|D^*\rangle\,, |D\rangle$ and $|A\rangle\,, |A^*\rangle$ are the initial and final states of the donor and acceptor, respectively, with the asterisk indicating an electronically excited state, while $|0\rangle$ refers to the photon vacuum. In the initial and final state energies, the terms e_{D^*}, e_D and e_A, e_{A^*} refer to the energies of the donor and acceptor respectively, in their initial and final states.

Typically, energy transfer appears as a first-order process, mediated by the Coulombic, Förster transition dipole coupling mechanism. This yields the characteristic near-zone distance dependency. From the QED theory, which treats both the matter and the radiation quantum mechanically, the energy transfer process emerges as second-order and the distance dependence is no longer limited to the near-zone separation like it was before. This is shown in the following description.

The rate of EET associated with the initial and final states given by the equations in

(2.2.5) above can be expressed using the Fermi Golden Rule

$$W_{FI} = \frac{2\pi}{h} | \langle F| T |I\rangle |^2 \delta(E_I - E_F), \tag{2.2.7}$$

where, $\delta(E_I - E_F)$ is the Dirac delta which enforces energy conservation and T is the transition operator, given by

$$T = V + V\left(\frac{1}{E_I - H^0 + is}\right) + \cdots = T^{(1)} + T^{(2)} + \cdots , \tag{2.2.8}$$

where $V = H_{int}(D) + H_{int}(A)$. The first order term, $T^{(1)}$, is identical to V and represents the single photon interaction events of photoabsorption and photoemission by individual molecules. Although important with respect to the initial excitation of a molecule and the possible dissipation of the excited energy, this term does not contribute to the energy transfer rate. As shown by the two separate, but equally valid, Feynman diagrams in Fig. 2.2.1, EET consists of two photon–matter interactions — a virtual photon is created at one species and annihilated at another species. As a result, it is the second-order term of the transition operator that produces the leading contribution for RET. The transition matrix element in equation (2.2.7) is therefore written as $\langle F| T^{(2)} |I\rangle$ and within this unified theory represents the coupling between two species. The calculation of this transition matrix element, often referred to as the quantum amplitude, is set up as follows and requires second-order perturbation theory [36],

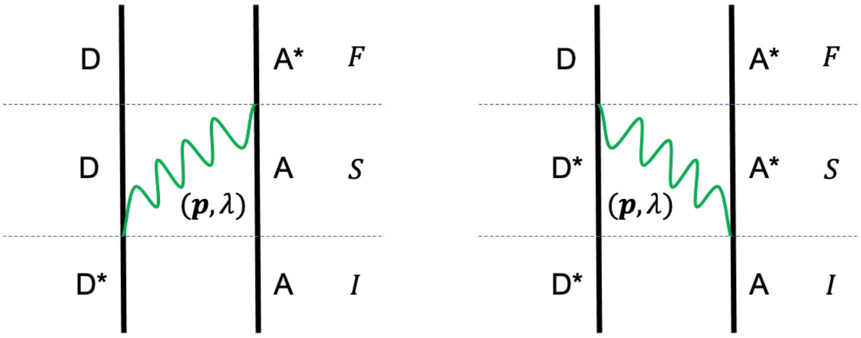

Figure 2.2.1: The two Feynman diagrams for energy transfer. D and A represent the donor and acceptor, respectively with * indicating the species is an electronically excited state. Starting from the bottom, I indicates the initial state of the molecule and radiation system when the donor is excited, the acceptor is in its ground state and no photon is present. S labels the intermediate state when there is a virtual photon present, as represented by the green wavy line, with wave vector $\boldsymbol{p}$ and polarisation λ, while F indicates the final state after the energy has passed from the donor to the acceptor.

$$\langle F| T^{(2)} |I\rangle = \sum_S \frac{\langle F| H_{int} |S\rangle \langle S| H_{int} |I\rangle}{(E_{I0} - \hbar ck)}, \tag{2.2.9}$$

where

$$\hbar ck = e_{A^*} - e_A = e_{D^*} - e_D > 0, \tag{2.2.10}$$

is the energy transferred in the process. Here, k is the wavenumber of the transferred energy, not the wavenumber corresponding to the virtual photon. This distinction is important as for the complete description, a sum over all possible virtual photon modes of wave vector **p** and polarisation λ is required. S represents the intermediate state in the process of which there are two types, as shown in Fig. 2.2.1. The most conceptually attractive view of the virtual photon being created at the donor which subsequently falls into its ground state is shown on the left. In this time ordering the intermediate state consists of both the donor and acceptor present in their ground state with one virtual photon present [36]. In the Feynman diagram on the right of Fig. 2.2.1, the virtual photon is created at the acceptor and annihilated at the donor, a pathway to the final state arising from the time-energy uncertainty principle [38]. The intermediate state in this time ordering comprises of both the donor and acceptor in their excited states with one virtual photon present [36]. These two possibilities are consistent. Although the first time ordering is the most dominant contribution to the quantum amplitude as the separation between the species increases, the full quantum amplitude requires the summation ($\sum_S$) of both time orderings, since the second Feynman diagram in Fig. 2.2.1 also leads to the same final, isoenergetic state [38].

Following on from equation (2.2.9), the quantum amplitude can be expressed in tensor form as [36, 38, 68],

$$\langle F| T^{(2)} |I\rangle = M^{dd} = \mu_{Ai}^{full} V_{ij}^{dd}(k, \mathbf{R}) \mu_{Dj}^{full}. \tag{2.2.11}$$

This assumes the summation convention over the repeated Cartesian coordinates i and j. As this work is modelling the dynamics in a 2D system, the values for both these Cartesian coordinates are x and y. The terms μ_D^{full} and μ_A^{full} are the transition dipole moments of the donor and the acceptor, respectively,

$$\boldsymbol{\mu}_D^{full} = \langle D | \, \boldsymbol{\mu}(D) \, | D^* \rangle \qquad \boldsymbol{\mu}_A^{full} = \langle A^* | \, \boldsymbol{\mu}(A) \, | A \rangle \,, \tag{2.2.12}$$

with the superscript $full$ indicating that both electronic and vibrational contributions are taken into consideration in the molecular state vectors of the transition dipoles.

Using the Bessel functions [69, 71],

$$h_0^{(1)}(kR) = -e^{ikR} \frac{i}{kR} \tag{2.2.13}$$

$$h_1^{(1)}(kR) = -e^{ikR} \left(\frac{1}{kR} + \frac{i}{k^2R^2} \right) \tag{2.2.14}$$

$$h_2^{(1)}(kR) = e^{ikR} \left(\frac{i}{kR} - \frac{3}{k^2R^2} - \frac{3i}{k^3R^3} \right) \tag{2.2.15}$$

$$h_3^{(1)}(kR) = e^{ikR} \left(\frac{1}{kR} + \frac{6i}{k^2R^2} - \frac{15}{k^3R^3} - \frac{15i}{k^4R^4} \right), \tag{2.2.16}$$

an expression for the electromagnetic coupling tensor for the retarded dipole-dipole coupling between a donor and an acceptor in a vacuum is obtained,

$$V_{ij}^{dd}(k, \mathbf{R}) = \frac{-ik^3}{4\pi\varepsilon_0} \left[\delta_{ij} h_0^{(1)}(kR) - \frac{1}{kR} \delta_{ij} h_1^{(1)}(kR) + \hat{R}_i \hat{R}_j h_2^{(1)}(kR) \right]. \tag{2.2.17}$$

Although the use of the Bessel functions provides a concise representation of the coupling tensor (something that becomes more necessary when considering the dipole-quadrupole interactions), it is useful to expand equation (2.2.17) in order to make clear the different distant dependent terms,

$$V_{ij}^{dd}(k, \mathbf{R}) = \frac{k^3 e^{ikR}}{4\pi\varepsilon_0} \left[(\delta_{ij} - 3\hat{R}_i \hat{R}_j) \left(\frac{1}{k^3R^3} - \frac{i}{k^2R^2} \right) - (\delta_{ij} - \hat{R}_i \hat{R}_j) \left(\frac{1}{kR} \right) \right] \tag{2.2.18}$$

where k is the same as above, R is the magnitude of the distance between the donor and the acceptor and $\hat{\mathbf{R}} = \mathbf{R}/R$, the unit vector along the donor-acceptor separation vector. The use of the summation convention of the Cartesian coordinates, represented by the subscripts i and j, results in the use of the unit vectors along the x and y directions. The final variable is the Kronecker delta, δ_{ij} which is equal to 1 when $i = j$ and equal to 0 when $i \neq j$.

It is this tensor that gives the three different distance dependencies of energy transfer. It contains the R^{-3} term characteristic of the radiation-less, near-zone ($kR \ll 1$) transfer of energy as well as the R^{-1} term, associated with the radiative transfer of energy in the far-zone ($kR \gg 1$), where the virtual photon propagating between the donor and the acceptor takes on more of a real character. The new distance dependent term that comes out of this unified theory contains an R^{-2} dependency, where the photon has reduced virtual character and its contribution plays an important role at critical retardation distances ($kR \sim 1$) [5, 67]. This occurs when the distance between the donor and the acceptor is approximately equal to the reduced wavelength ($\lambda/2\pi$) of the energy being transferred.

2.2.2 The Unified Theory of Energy Transfer — Dipole-Quadrupole Contributions

As with the electric dipole approximation form of the unified theory, the full QED representation of the coupling between transition moments incorporating the higher order multipole terms may be found elsewhere — the important aspects of the theory that are related to this work are presented here.

On consideration of the dipole-quadrupole coupling contributions, it is the interaction Hamiltonian, Eq. (2.2.3), that changes, with an extra term included for the quadrupole contributions [69],

$$H_{int}(X) = -\varepsilon_0^{-1}\mu_i(X)d_i^{\perp}(\mathbf{R}_X) - \varepsilon_0^{-1}\Theta_{ij}(X)\nabla_i d_j^{\perp}(\mathbf{R}_X). \tag{2.2.19}$$

Here, Θ_{ij} is the electric quadrupole transition moment tensor operator in Cartesian tensor notation for molecule X and is given by

$$\Theta_{ij}(X) = \frac{1}{2!}\sum_p e_p(\mathbf{r}_p - \mathbf{R}_X)_i(\mathbf{r}_p - \mathbf{R}_X)_j, \tag{2.2.20}$$

where $\mathbf{r}_p$ is the position vector of the charge e_p at point p and, as before, $\mathbf{R}_X$ is the position vector of molecule X. Using equation (2.2.9) the transition matrix element eventually follows as

$$\langle F| T^{(2)} |I\rangle = M^{dq} = [\mu_i^A \Theta_{jk}^B - \Theta_{jk}^A \mu_i^B] V_{ijk}^{dq}(k, \mathbf{R}). \tag{2.2.21}$$

In order to obtain a complete description of the dipole-quadrupole contributions to the coupling, both the situation where the dipole is the the transmitter and the quadrupole the acceptor (first term in the brackets) and the opposite scenario in which the quadrupole is the transmitter and the dipole the acceptor (second term in the brackets), have been taken into account [69, 72]. As before, the summation convention over Cartesian indices i, j and k is assumed and in order to obtain the complete coupling as described through the dipole-dipole and dipole-quadrupole interactions, equations (2.2.11) and (2.2.21) may simply be added to give

$$\langle F| T^{(2)} |I\rangle = M^{full} = \mu_i^A V_{ij}^{dd} \mu_k^B + [\mu_i^A \Theta_{jk}^B - \Theta_{jk}^A \mu_i^B] V_{ijk}^{dq}(k, \mathbf{R}). \tag{2.2.22}$$

The dipole-quadrupole coupling tensor (in vacuum) is then obtained and presented using the Bessel functions, (2.2.14)–(2.2.16), in similar fashion to the dipole-dipole coupling tensor, Eq. (2.2.17) [69, 72],

$$\begin{aligned} V_{ijk}^{dq}(k, \mathbf{R}) = \frac{ik^4}{4\pi\varepsilon_0} \Big[&\delta_{ij} \hat{R}_k h_1^{(1)}(kR) \\ &- \frac{1}{kR}(\delta_{ij}\hat{R}_k + \delta_{ik}\hat{R}_j + \delta jk \hat{R}_i) h_2^{(1)}(kR) + \hat{R}_i \hat{R}_j \hat{R}_k h_3^{(1)}(kR) \Big]. \end{aligned} \tag{2.2.23}$$

This tensor can be found expanded in separate works carried out by both Salam and Dávila Romero [73, 74]

2.2.3 Exciton Dynamics

Beyond inspecting the coupling itself, one of the most intuitive and informative ways of examining the influence of the dipole-quadrupole contributions to the coupling in the theory above is to model the movement of the energy. As an alternative to using the wavefunction and the time-dependent Schrödinger equation, the density matrix ρ and the Liouville–von Neumann equation have been employed to simulate the movement of a delocalised excitation, or exciton, a quasiparticle of bound electron-hole pairs initially situated on the central molecule in a brickstone lattice [70, 75],

$$\frac{\mathrm{d}\rho}{\mathrm{d}t} = -\frac{i}{\hbar}[H, \rho] = -\frac{i}{\hbar}H\rho + \frac{i}{\hbar}\rho H. \tag{2.2.24}$$

The coupling (M_{nm} and M_{mn}) corrected electronic Hamiltonian operator in the site basis that is employed in the simulations is expressed as

$$\hat{H} = \sum_{n=1}^{N} \epsilon_n \left|n\right\rangle \left\langle n\right| + \sum_{n,m\neq n}^{N} (M_{nm} \left|n\right\rangle \left\langle m\right| + M_{mn} \left|m\right\rangle \left\langle n\right|), \tag{2.2.25}$$

where, ϵ_n are the energies of the electronic excitations of the molecules at each site, n, in the lattice, corresponding to the diagonal elements of the Hamiltonian matrix, while M_{nm} and M_{mn} are the couplings between the monomers at sites n and m in the lattice consisting of a total of N monomers, corresponding to the off-diagonal elements of the matrix.

It has been found that, when incorporating the coupling that results from the unified theory of EET into the Hamiltonian (Eq. (2.2.25)), the Hamiltonian is not Hermitian. This has an important consequence on the dynamics routine as the population is no longer conserved. It is thought that this results from an ambiguity in the sign of the electromagnetic coupling tensor employed in the QED description of the coupling between a pair of species, Eq. (2.2.26).

$$V_{ij}^{\pm}(k, \mathbf{R}) = \frac{k^3 e^{\mp ikR}}{4\pi\varepsilon_0}\left[(\delta_{ij} - 3\hat{R}_i\hat{R}_j)\left(\frac{1}{k^3R^3} \pm \frac{i}{k^2R^2}\right) - (\delta_{ij} - \hat{R}_i\hat{R}_j)\left(\frac{1}{kR}\right)\right] \tag{2.2.26}$$

It is known that it is the imaginary part that displays the ambiguity in sign [38]. Therefore, since in an Hermitian Hamiltonian matrix the off-diagonal elements are complex conjugate to one another, it is likely that this ambiguity in the sign of the imaginary part of the coupling tensor is the cause of the non-Hermitian Hamiltonian that results from the use of the coupling described in the unified theory. The different signs describe the incoming and outgoing waves (i.e. the two Feynman diagrams that describe the process of resonance energy transfer) for a complete description of the process [38]. It is reported by Daniels *et al.* that $V_{ij}^{\pm}(k, \mathbf{R})$ is only part of a quantum amplitude which is not a measurable [38]. They go on to say that "so long as the observable offers an accurate model of experimental data, then ambiguity at the quantum amplitude level is perfectly acceptable" [38]. Therefore, in order to simulate the dynamics of energy transfer and 'offer an accurate model of experimental data', while employing couplings derived from molecular QED, the computational Hamiltonian is made Hermitian manually [38].

The density matrix is updated through the use of equation (2.2.24) alongside the higher order terms based on a truncated Taylor series expansion. This allows for the propagation of the exciton in the lattice to be studied. The information is then subsequently used to investigate the effect of including the dipole-quadrupole contributions to the coupling description, through a comparison to simulations that employ a coupling description based on dipole-dipole interactions alone. The diagonal elements of the density matrix, $\rho(t)$ represent the probability of the system being found in state n, that is to say, the probability of the exciton (which is the 'system' under investigation through this equation in these simulations) being found at site n of the lattice [75]. These are therefore referred to as populations. The off-diagonal elements of the density matrix represent the coherences between the coupled molecules [75].

2.3 Results and Discussion

The formalism that results in the unified theory of EET is perfectly capable of incorporating the higher multipole terms which may be important in accurately describing energy transfer in condensed phase systems, QD materials, lanthanide-containing materials and systems in which dipole transitions are forbidden. To initiate investigations into this more detailed depiction of the Coulombic interaction to the electronic coupling, this work looks at the next order terms in the multipole expansion, that is, the dipole-quadrupole interactions. These terms are included alongside the dipole-dipole interactions (Eq. (2.2.22), M^{full}), and through examination of the coupling and movement of energy through a lattice, their influence is examined by comparison with results obtained for which only the dipole-dipole interactions are considered (Eq. (2.2.11), M^{dd}).

2.3.1 Computational Calculations

In accordance with our previous investigation into modelling the energy transfer process using the unified theory of EET, the molecules employed in this work are all a cyanine dye molecule, TC (Fig. 2.1.1), that is known to form J-aggregates which have been extensively studied with respect to their light-harvesting capabilities [31]. J-aggregates are any collection of organic fluorescent dye molecules that are identified spectroscopically by the narrowing and shift to longer wavelengths (a bathochromic shift) of a specific absorption band upon aggregation [70]. In the simulations using the equations given above, each molecule is described through their transition moments and their excitation energy. This required data was determined through computational calculations using the Density Functional Theory (DFT) and the 6-31g* basis set, carried out with the Gaussian 09 program, after constructing the molecule in Gaussview and then optimising it to find the optimum geometry [76–78]. Following this, a time-dependent DFT (TDDFT) calculation was carried out, calculating the first 20 lowest energy singlet electronic excitations which ranged in energy from 1.93 eV to 3.91 eV. Based on the oscillator strengths (f values) for each of the states, which represent the intensity of a transition to that state, the most likely transition is to excited state 11. The energy of this state is 3.3 eV, which is in excellent agreement with the energy quoted by Valleau *et al.* for the same molecule [70]. The transition dipole and transition quadrupole data given in the output of the calculations for excited state 11 are reported in Tables 2.3.1 and 2.3.2 below, with the transition dipole moment also in reasonable agreement with that quoted by Valleau *et al.* [70].

State	$\mu_x(D)$	$\mu_y(D)$	$\mu_z(D)$	$\lvert\mu\rvert(D)$
11	8.6475	0.1029	-0.4242	8.6585

Table 2.3.1: Transition electric dipole moment data of excited state 11 for the TC cyanine dye

State	$\Theta_{xx}(D\text{Å})$	$\Theta_{yy}(D\text{Å})$	$\Theta_{zz}(D\text{Å})$	$\Theta_{xy}(D\text{Å})$	$\Theta_{xz}(D\text{Å})$	$\Theta_{yz}(D\text{Å})$
11	-0.0151	0.0351	-0.0034	1.7957	-0.0373	-0.1798

Table 2.3.2: Transition velocity quadrupole moment data of excited state 11 for the TC cyanine dye

It was noted that the transition quadrupole data given above is that of the transition velocity quadrupole moment, while that of the dipole data is the transition electric dipole moment. It is understood that transition dipole moment can be represented in two ways and that the former refers to the transition quadrupole moment in the velocity representation, while the latter is the transition dipole moment in the standard length representation [79]. In the length representation, the transition dipole moment is calculated through the use of the position operator, $\hat{\mathbf{r}}_i$, which obviously just uses the position vector of point i, while in the velocity representation, the momentum operator is employed, $-i\hbar\nabla$ [80]. As we are to use the quadrupole moments alongside the dipole moments, it is believed that, for consistency, the two moments should be employed in the same representation. As a result of being the more commonly used of the two representations, at the time, the length representation was chosen and consequently the quadrupole moments had to be converted. To do this, the relationship given in appendix A of work by Bernadotte, Atkins and Jacob (given below) has been employed [80],

$$\langle 0| \hat{Q}^{p}_{\alpha\beta} |n\rangle = -i\frac{E_{0n}}{\hbar} \langle 0| \hat{Q}_{\alpha\beta} |n\rangle . \tag{2.3.1}$$

The term, $\langle 0| \hat{Q}^{p}_{\alpha\beta} |n\rangle$, represents the electric quadrupole transition moment in the velocity representation, while $\langle 0| \hat{Q}_{\alpha\beta} |n\rangle$, is the transition quadrupole moment in the length representation, with E_{0n}, the electronic excitation energy.

Essentially, the same relationship is given in Ref. [80] for the transition dipole moments. To verify that these relations hold for the data that was given from the

Gaussian calculations, the transition dipole moments were used as these were given in both the length and velocity representations. It was found that the values quoted for the transition dipole moment in the velocity representation were consistently calculated as imaginary when using the relationship given in Ref. [80]. This implies that the electric transition dipole moment in the velocity representation is phase shifted from that in the length representation. As the work described below involves a comparison of results obtained from the use of Eq. (2.2.22) and those of Eq. (2.2.11), in order to ensure the only differences seen are from the influence of the dipole-quadrupole interactions, and not the particular representation of the moments, in calculating the transition quadrupole moments in the length representation, the value quoted by Gaussian has been taken to be imaginary in order to phase match the two representations. The equation employed in the simulations is given below which is just a rearrangement of Eq. (2.3.1) where$\langle 0| \hat{Q}^p_{\alpha\beta} |n\rangle$ represents the value of the transition quadrupole moment in the velocity representation quoted by Gaussian, and $\langle 0| \hat{Q}_{\alpha\beta} |n\rangle$ is the value calulated for the transition quadrupole moment in the length representation,

$$\langle 0| \hat{Q}_{\alpha\beta} |n\rangle = \langle 0| \hat{Q}^p_{\alpha\beta} |n\rangle \, i \frac{\hbar}{-iE_{0n}}. \tag{2.3.2}$$

The elements of the transition quadrupole moment in the length representation are given in Table 2.3.3.

State	$\Theta_{xx}(D\text{Å})$	$\Theta_{yy}(D\text{Å})$	$\Theta_{zz}(D\text{Å})$	$\Theta_{xy}(D\text{Å})$	$\Theta_{xz}(D\text{Å})$	$\Theta_{yz}(D\text{Å})$
11	-0.1242	0.2894	-0.027	14.8054	-0.3072	-1.4826

Table 2.3.3: Transition quadrupole moment data of excited state 11 in the length representation for the TC cyanine dye

2.3.2 Dipole-Quadrupole Influences on a Lattice

In an extension to our previous work on energy transfer and the unified theory of EET, an investigation into the effects on the coupling and energy transfer dynamics on inclusion of the dipole-quadrupole terms to the coupling description has been carried out using a 2D brickstone lattice of 25 times 25 TC cyanine dye molecules (Fig. 2.1.1) [31]. As described in Ref. [31], the brickstone lattice is characterised by three lattice parameters, the horizontal distance between each point, $\mathbf{r}_x$, the vertical distance between each row, $\mathbf{r}_y$, and the distance by which adjacent rows are offset, $\frac{1}{2}\mathbf{r}_x$. As has already been discussed, the most probable scenario for which the inclusion of the higher order multipole moments may become instrumental in accurately describing the electronic coupling between species is at short distances, when the ideal dipole approximation is no longer valid. As a crossover with our previous work, the lattice parameters chosen initially for the investigation are $\mathbf{r}_x = \mathbf{r}_y = 2$ nm with the distance adjacent rows are offset consequently being 1 nm, resulting in a lattice approximately 50 nm by 50 nm. The electronic couplings are calculated for every pairwise interaction within the lattice by employing Eq. (2.2.22) for dipole-dipole and dipole-quadrupole considerations and Eq. (2.2.11) for calculation of the coupling using dipole-dipole interactions alone. These are then subsequently used as the off-diagonal elements of the Hamiltonian employed in the Liouville–von Neumann equation, Eq. (2.2.24), and the dynamics of the energy transfer process studied through examination of the energy migration landscapes after the density matrix is initialised with population localised on the central molecule in the lattice. This molecule is commonly referred to as molecule 313 through the remainder in this work, based on a numbering system counting from left to right, bottom to top through the lattice, with the first molecule placed at the origin of a set of axes defining the lattice. The electronic excitation energy of the molecules employed in this work is currently 3.0 eV, consistent with our previous study which employed approximate data for the energy and dipole moments based on the average of three cyanine dye molecules [31, 70].

To begin with, the lattice employed consisted of identical molecules with identical orientations placed at the 625 points. On examination of the coupling, it was apparent that the dipole-quadrupole coupling for each pairwise interaction was zero. Through inspection of Eq. (2.2.21), this can be understood. As a consequence of accounting for both the scenarios where the electric dipole is the donor and the quadrupole is the acceptor and vice versa, two terms containing the Cartesian components of the transition dipole and quadrupole moments are present with the two being taken away from one another [72]. Although different in what they describe, the first term representing the dipole as the donor and the quadrupole as the acceptor while the second represents the opposite situation, for the lattice model employed in this simulation they are identical, because the molecules, and more importantly, the orientation of the molecules are all identical. So, the xx component of the quadrupole for the donor is exactly the same as that for the acceptor (which becomes the donor in the second scenario), and thus the dipole-quadrupole coupling is zero. Therefore, in systems where the orientation of each identical molecule is able to be highly controlled such that it is the same for each, the dipole-quadrupole interactions will not have an influence on the coupling or subsequent energy transfer dynamics.

Although an important feature of the dipole-quadrupole coupling employed in this work, rather than a lattice of identically oriented molecules, typically in condensed phase systems the orientation of the molecules within them is more random, and as a result the Cartesian components of the transition dipole and quadrupole moments will likely differ and therefore the dipole-quadrupole coupling will no longer be zero. Thus a more representative lattice model is required. Through the use of the rotation matrix each molecule in the lattice is rotated by a random angle (θ) between 0 and 2π. As a 2D lattice is being employed, a rotation in the xy plane is carried out and because the transition moments given from the Gaussian calculation do have z components, the rotation is viewed as a rotation about the z-axis using a 3D matrix (Eq. (2.3.3)). The rotation matrix on its own performs a rotation on a column vector, as we have for the transition dipole moment. However, the quadrupole moment is a rank-2 tensor so in order to carry out a rotation of this, the transpose of the rotation matrix ($\Theta_{ij}^{'}$) is also employed according to Eq. (2.3.4), where the elements Θ_{ij} are the values for the transition quadrupole moment elements calculated above,

$$\begin{bmatrix} cos\theta & -sin\theta & 0 \\ sin\theta & cos\theta & 0 \\ 0 & 0 & 1 \end{bmatrix} \tag{2.3.3}$$

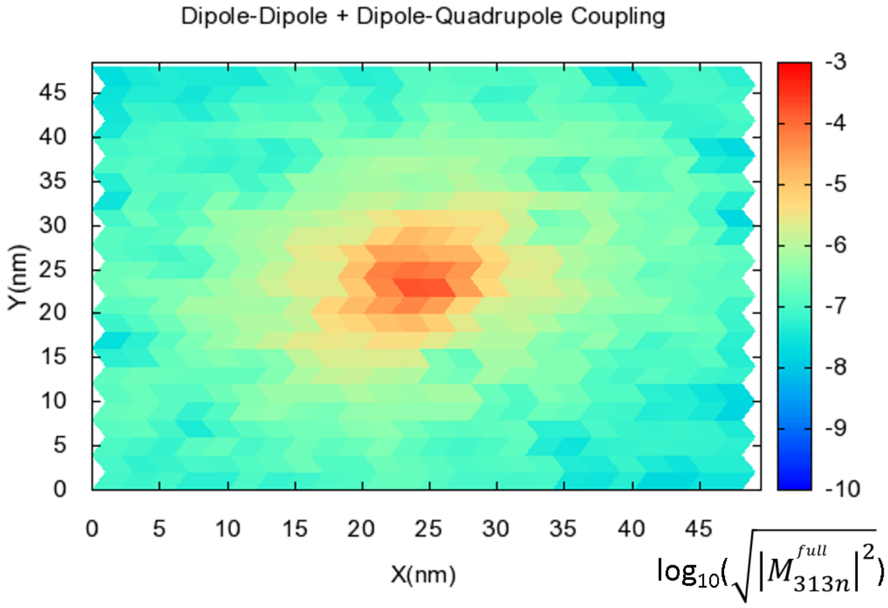

Figure 2.3.1: Coupling magnitude (on logarithmic scale) between the central molecule (313) and all other molecules in the lattice for a coupling description that considers both dipole-dipole and dipole-quadrupole interactions using lattice parameters of $r_x = r_y = 2$ nm.

$$\Theta'_{ij} = \begin{bmatrix} cos\theta & -sin\theta & 0 \\ sin\theta & cos\theta & 0 \\ 0 & 0 & 1 \end{bmatrix} \begin{bmatrix} \Theta_{xx} & \Theta_{xy} & \Theta_{xz} \\ \Theta_{yx} & \Theta_{yy} & \Theta_{yz} \\ \Theta_{zx} & \Theta_{zy} & \Theta_{zz} \end{bmatrix} \begin{bmatrix} cos\theta & sin\theta & 0 \\ -sin\theta & cos\theta & 0 \\ 0 & 0 & 1 \end{bmatrix} . \qquad (2.3.4)$$

Employing this new lattice where each molecule has its own, independent orientation, separate simulations were run using Eqs. (2.2.22) and (2.2.11), ensuring that the same angles were used in the calculations of the orientations at each site for both scenarios to allow a valid comparison to be made. The coupling of the central molecule (molecule 313) to all the other molecules in the lattice has been used to generate coupling landscapes that allow for the spatial dependency of the coupling to be examined. Figure 2.3.1 shows the coupling that results from consideration of both the dipole-dipole and dipole-quadrupole interactions (M^{full}), while Fig. 2.3.2 depicts the coupling as described through dipole-dipole interactions alone, (M^{dd}).

As a consequence of employing random orientations of each molecule in the lattice, a distinct pattern to the coupling explained through transverse and longitudinal (with respect to the intermolecular displacement vector) photons is no longer present, as was

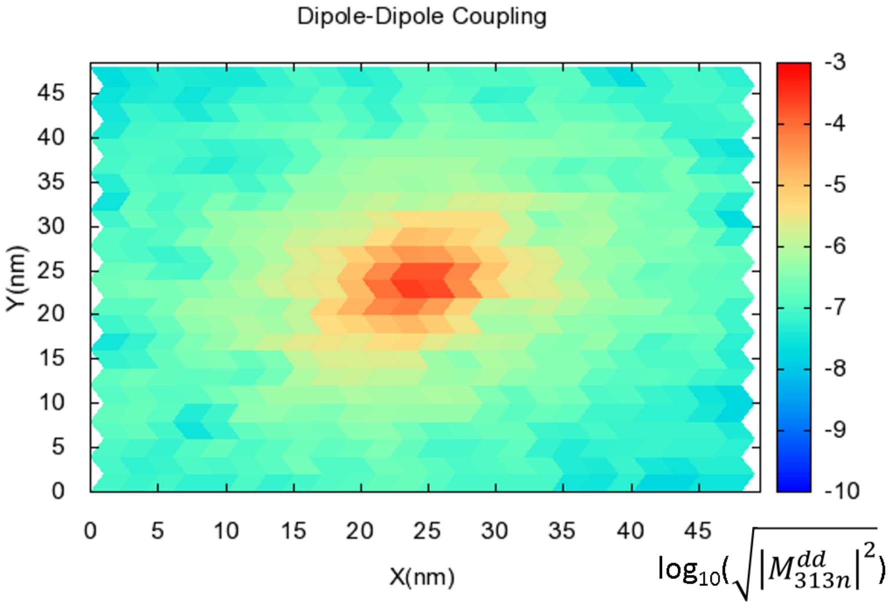

Figure 2.3.2: Coupling magnitude (on logarithmic scale) between the central molecule (313) and all other molecules in the lattice for a coupling description that considers only dipole-dipole interactions using lattice parameters of $r_x = r_y = 2$ nm.

the case in the previous work [31]. As one would expect, for both landscapes, a region of strong coupling is seen in the centre of the lattice and as the distance to the central molecule increases, the coupling decreases. Although a subtle change in the colour can be seen in the centre of the lattice, suggesting that the coupling resulting from M^{full} is weaker than that of M^{dd}, very little information on the influence of the dipole-quadrupole interactions is discernible from these plots. Figure 2.3.3 shows the difference (of the log values) between the M^{full} and M^{dd} landscapes. A positive value (orange and red colours in the plot) indicates that the inclusion of the dipole-quadrupole interactions (M^{full}) results in a stronger coupling, while a negative value shows that the coupling is weaker (light and dark blue colours).

Once more, there is no pattern to any differences that are seen. Much of the plot indicates essentially no difference in the coupling of the central molecule to the others in the lattice as described by M^{full} and M^{dd}, shown by the light green colour in the landscape. The differences that do occur, do so fundamentally on a point-by-point basis, and as the colours show, the differences don't appear to be very strong. In light of these results, the coupling of the central molecule to the others in the lattice was examined more closely

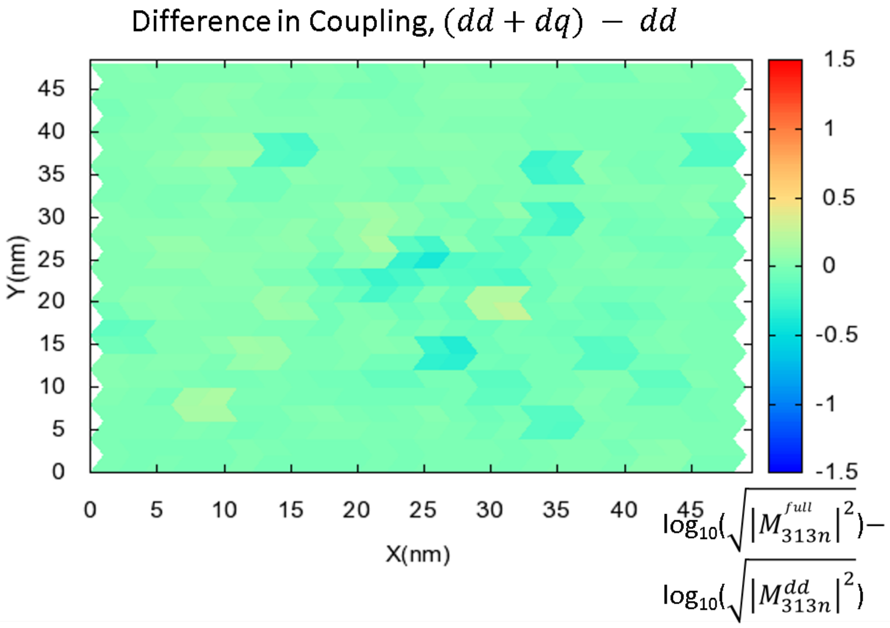

Figure 2.3.3: Difference in the coupling between that calculated using both dipole-dipole and dipole-quadrupole interactions and that caluclated using dipole-dipole interactions alone. A positive value implies the M^{full} (i.e. dipole-dipole- and dipole-quadrupole interactions) coupling is stronger than M^{dd} (dipole-dipole) coupling, while negative values indicate the opposite. The coupling is between the central molecule (313) and all other molecules in the lattice using lattice parameters of $r_x = r_y = 2$ nm.

by considering the coupling values as opposed to the log values being plotted. It was found that at the maximum difference M^{full} was 17.3 times as large as M^{dd}, while at the minimum of the difference between M^{full} and M^{dd}, M^{dd} was 17.5 times as large as M^{full}. Therefore, although the dipole-quadrupole coupling is in general smaller than the dipole-dipole coupling, these values show that it can have a significant effect on the complete coupling description. These particular results only occur at one site of the lattice (the coupling of 313 to 266 and 189, respectively), and excluding these and other one off values, we find that at the maximum, M^{full} is in general twice as big as M^{dd}, while at the opposite end, the minimum of the difference between M^{full} and M^{dd} most frequently encountered was approximately M^{dd} 2–2.5 times as large as M^{full}. This therefore explains the landscape shown in Fig. 2.3.3 — the difference being plotted is the difference in the log values of Figs. 2.3.1 and 2.3.2, thus, because the difference between M^{full} and M^{dd} are not commonly an order of magnitude different, the two coupling descriptions appear similar in the landscape. Any points of the lattice which do show an order of magnitude difference in the coupling are hidden in the landscape by

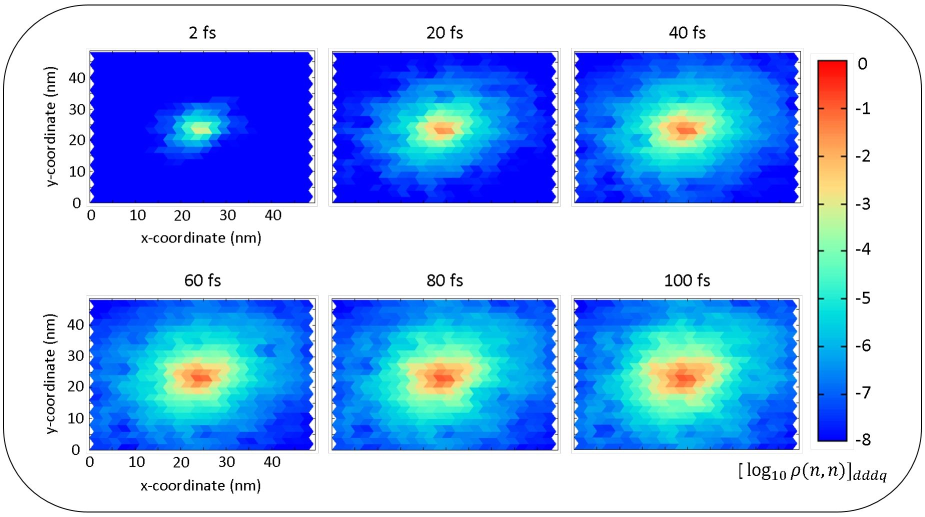

Figure 2.3.4: Plots of the exciton population (logarithmic scale) throughout the lattice at 2, 20, 40, 60, 80 and 100 fs of the 100 fs dynamic trajectories, driven by the M^{full} coupling (i.e. dipole-dipole and dipole-quadrupole interactions). Lattice parameters of $r_x = r_y = 2$ nm are being used.

the general coupling seen in the lattice.

To understand what these differences mean for the influence of the dipole-quadrupole interactions on the energy transfer process, the exciton dynamics driven by M^{full} and M^{dd} are considered through Eq. (2.2.24), employing the exact same lattice model used for the coupling investigations carried out above. The electronic excitation energy associated with the molecules is 3 eV and has been taken to correspond to the transferred energy in the simulated process. The density matrix is initialised such that 100 % of the exciton density is placed on the central molecule and the dynamic routines ran for a total of 100 fs. Figure 2.3.4 shows the exciton population across the lattice on a logarithmic scale at selected times during the dynamics for the simulation which employed the M^{full} coupling, while Figure 2.3.5 shows those results obtained through the use of the M^{dd} coupling.

As can be seen, the exciton density dissipates throughout the lattice as time passes. At the end of the 100 fs trajectory, distinct regions of exciton population are clearly visible, in particular a region of high exciton population spread unevenly around a 15 nm x 15 nm area in the centre of the lattice, in both cases. Further out from the centre, the exciton density decreases. Once more there is no distinctive pattern seen in the migration of the

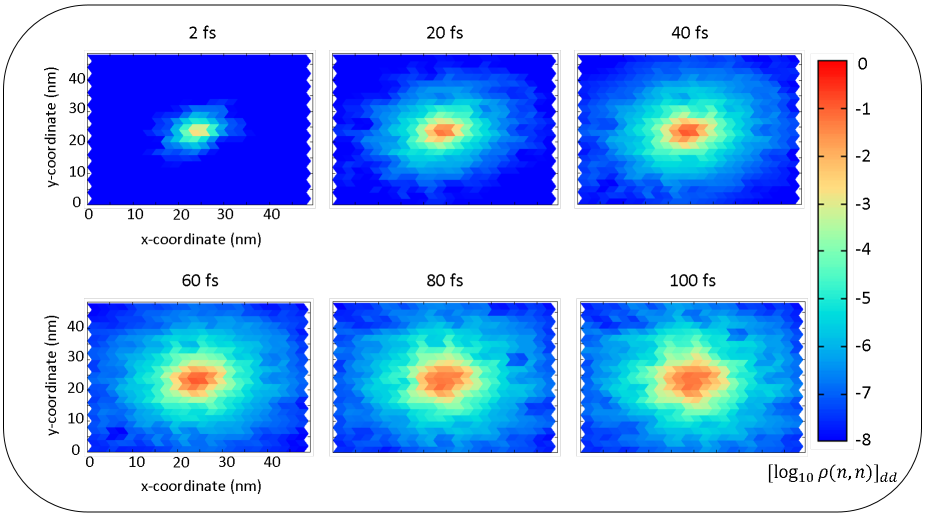

Figure 2.3.5: Plots of the exciton population (logarithmic scale) throughout the lattice at 2, 20, 40, 60, 80 and 100 fs of the 100 fs dynamic trajectories, driven by the M^{dd} coupling (i.e. dipole-dipole interactions only). Lattice parameters of $r_x = r_y = 2$ nm are being used.

exciton density as a result of the random orientations employed. Broadly speaking the plots in the two figures appear very similar to one another, especially at earlier times in the dynamics. However, on closer inspection of the plots at 100 fs, a few differences are noted. While covering the same area of the lattice, the shape of the central region is in fact seen to differ between the two coupling descriptions, with the colours indicating high exciton density extending more in the direction of the y-axis, while also shifting further to the right for the dynamics described through the dipole-dipole interactions alone. Comparing the 100 fs plots side-by-side, it becomes clearer that this and other differences occur as a result of the whole plot appearing to be ’rotated’ about the centre. In the 100 fs dynamics plot generated from the M^{full} coupling, there is a region of moderate exciton density that forms a hexagon around the centre and which extends from the bottom left corner to the top right, leaving regions of low exciton density in the top left and bottom right corners of the lattice. In the same plot described by M^{dd} coupling, the shape of the region of moderate exciton density has changed and now extends from the top left of the lattice to the bottom right, with the remaining corners of the lattice showing less exciton density. Although subtle differences were noted in the central regions of the coupling landscapes (Figs. 2.3.1 and 2.3.2), the differences further out in the lattice were not substantial enough to suggest the features seen in the dynamics. To try and understand these features a bit more, differences have been taken

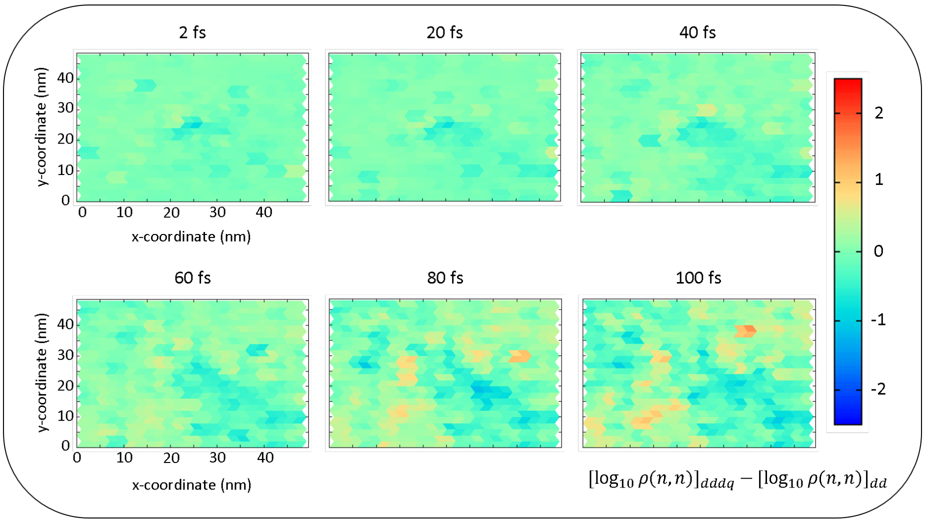

Figure 2.3.6: Plots of the difference in the exciton population (logarithmic scale) throughout the lattice between the trajectories driven by M^{full} and M^{dd} at 2, 20, 40, 60, 80 and 100 fs of the 100 fs dynamic routines. The dipole-dipole simulation is taken away from the dipole-dipole, dipole-quadrupole simulation, such that a negative value (bluer colour) indicates that the dipole-dipole coupling results in a larger population and a positive value (redder colour) indicates that M^{full} results in a larger exciton population. Lattice parameters of $r_x = r_y = 2$ nm are being used.

between corresponding times of the dynamics for the two coupling descriptions and are shown in Fig. 2.3.6. The logarithmic values of the exciton density resulting from M^{dd} were taken away from those described by M^{full}, meaning a positive value indicates that the exciton population resulting from M^{full} is larger than that resulting from M^{dd}, while a negative value is just the opposite.

As expected from the dynamics plots in Figs. 2.3.4 and 2.3.5, the plots in Fig. 2.3.6 show that at early times in the dynamic trajectories, there is little difference in the exciton density driven by the two coupling descriptions. As time evolves, after about 40 fs, differences at certain points throughout the lattice start to appear. Once again no distinctive pattern to the differences is immediately obvious, especially early on, and again this is explained by the use of random orientations for each molecule in the lattice. Considering the features highlighted above, the difference plot at 100 fs was examined more closely. Although not well-defined, it can be seen that on average in the bottom left and top right corners of the lattice, the inclusion of the dipole-quadrupole interactions results in greater exciton density. In the bottom right corner and to a lesser extent the top left corner of the lattice, the inclusion of these contributions results in lower exciton density, confirming the pattern discussed above. These initial results therefore hint that the dipole-quadrupole interactions may have an influence on the overall direction of energy transfer throughout a lattice. It is interesting to note that, even though random orientations are being employed for each molecule, this is a general pattern and therefore suggests that it is the relative position of the molecules that is having the strongest impact on the influence of the dipole-quadrupole contributions and that the orientation of the molecules themselves only dictates exactly how strong that contribution may be.

It should be noted that, as with the coupling landscape in Fig. 2.3.3, the differences are not very strong on the scale given, meaning differences involved are not of an order of magnitude. However, at certain points there is indeed an order of magnitude difference, hence the choice of scale, but these become hidden in the wider picture of the lattice as a whole. To therefore understand the features being seen, and the quantitative impact they may have, a better understanding of the dipole-quadrupole interactions is required, especially with respect to intricate relationship between the orientation of molecules relative to each other, the orientations of the individual molecules, and the distance between them. For this, an investigation has been carried out into the strength of the coupling between a pair of molecules as function of both the orientation of one of the molecules and the position between them. The results of this are in Section 2.3.3.

To complete the initial investigation into the dipole-quadrupole influences on the lattice, the population at specific sites were examined. Following on from the above discussion, the population of molecule 521 was plotted as a function of time for the two coupling descriptions employed (Fig. 2.3.7). This molecule lies diagonally from the centre in the top right corner of the lattice at 40 nm x 40 nm. As can be seen, the exciton population resulting from the consideration of the dipole-dipole and dipole-quadrupole terms in the coupling between species is greater than that seen when considering dipole-dipole interactions alone. This is consistent with the trends seen from the dynamics plots (Figs. 2.3.4, 2.3.5 and 2.3.6) and suggests that the relative position of the molecules is important in describing the influence of the dipole-quadrupole interactions on the coupling and subsequent energy transfer dynamics between species.

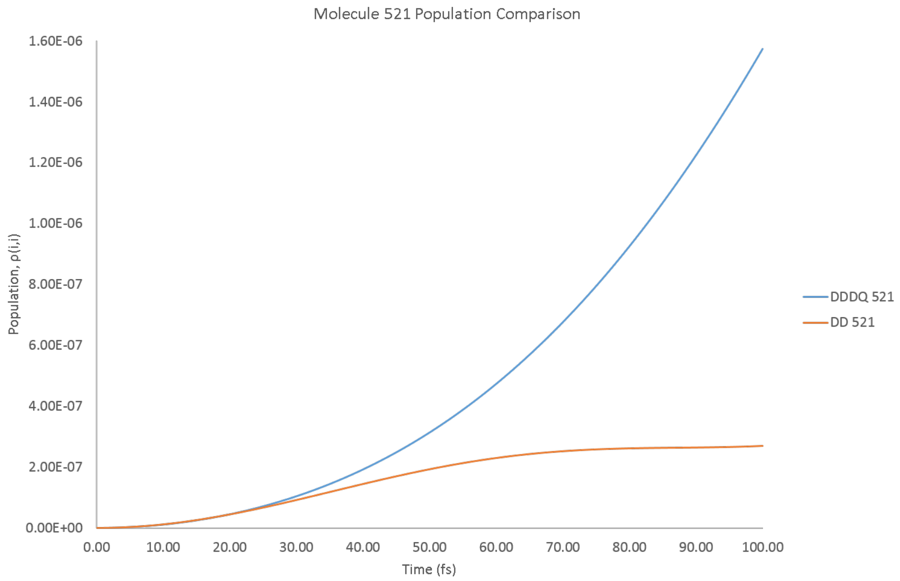

Figure 2.3.7: Plots of the exciton population at molecule 521 as a function of time for the two coupling descriptions employed in this work. Molecule 521 is located in the top right corner of the lattice at 40 nm x 40 nm, using lattice parameters of $r_x = r_y = 2$ nm. The blue line is the population as driven by the dipole-dipole and dipole-quadrupole interactions. The red line is the population driven by dipole-dipole interactions alone.

It should be noted that the population at molecule 521, irrespective of the specific coupling description employed, is small. Therefore the features in the plots of the dynamics that were described may not be that important when it comes to accurately describing energy transfer, however that depends on where exactly this directionality has an effect, and thus requires further investigation.

Of more significance would certainly be any differences seen in the central region of strong coupling and large exciton density. Figure 2.3.8 shows the population at molecule 313 as function of time for the two coupling descriptions employed in this work. This molecule is effectively at the centre (24 nm x 24 nm) and is the one on which 100 % of the exciton density was placed at the start of the dynamics routines. Figure 2.3.9 shows the exciton population at selected sites that are neighbours to, or at least close to, the central site.

From Fig. 2.3.8, it is evident that, by including the dipole-dipole interactions in the coupling description, the amount of energy (exciton density) that is transferred from the central site decreases. The plots in Fig. 2.3.9 show that, in general, the increase in

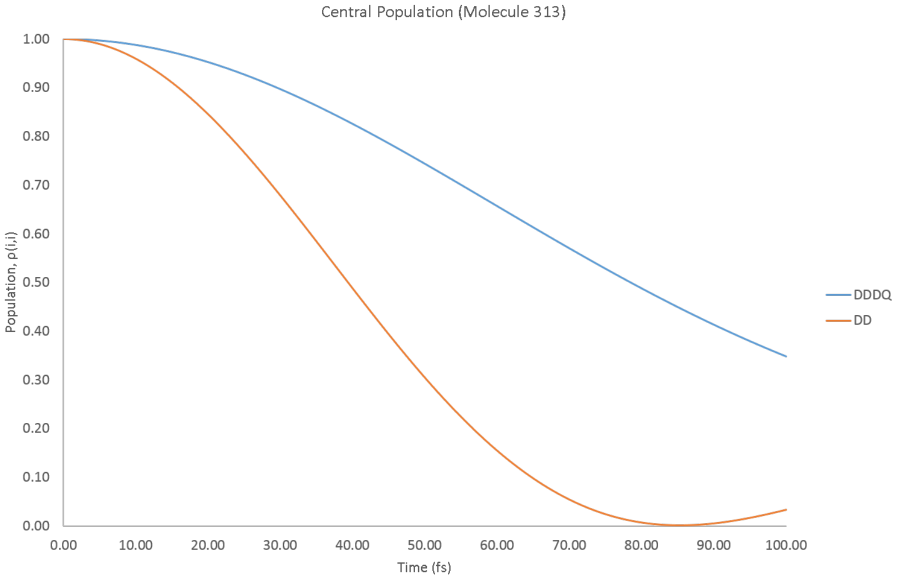

Figure 2.3.8: Plots of the exciton population at the central molecule (molecule 313) as a function of time for the two coupling descriptions employed in this work. This molecule is located at 24 nm x 24 nm, using lattice parameters of $r_x = r_y = 2$ nm. The blue line is the population as driven by the dipole-dipole and dipole-quadrupole interactions. The red line is the population driven by dipole-dipole interactions alone.

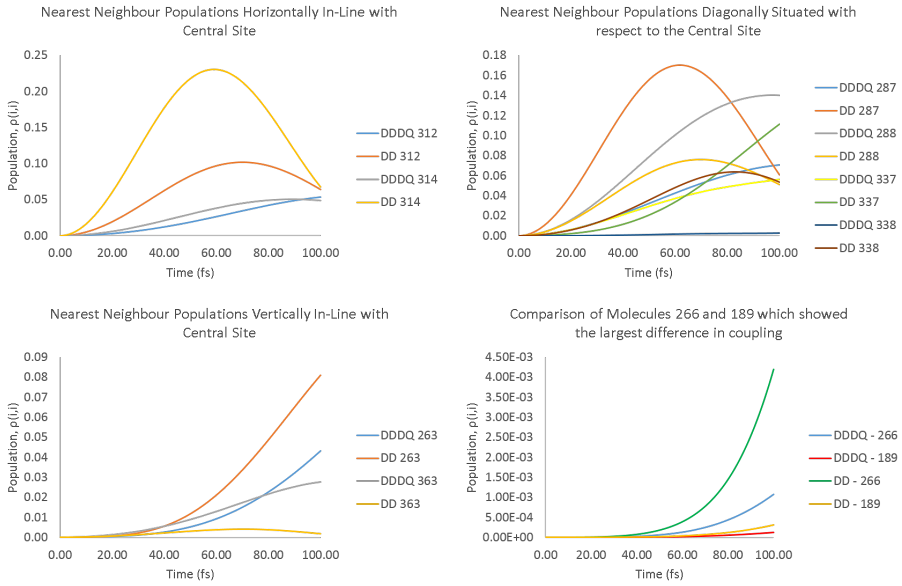

Figure 2.3.9: Plots of the exciton population at selected molecules around the centre site, as indicated by the legends for each plot.

population at the sites under consideration is less when the dipole-quadrupole interactions are taken into consideration, which is consistent with the decrease in the rate of energy transfer from the central site. The exceptions are molecules 288, 363 and initially 337. All three of these sites had had a coupling to molecule 313 that was bigger when the dipole-quadrupole interactions were taken in to consideration. None of the sites plotted in Fig. 2.3.9, lie along the diagonal of the lattice that runs from the bottom left corner to the top right, except for molecules 287 and 338. It is therefore difficult at this stage to deduce whether or not the pattern seen in the dynamics plots, whereby exciton density was larger for the coupling described by M^{full} in the bottom left and top right corners of the lattice, occurs in the region of high exciton density close to the centre. The molecules of 287 and 338 that do lie in this region have couplings to 313 that are much weaker when the dipole-quadrupole interactions are included and thus more data is required in order to develop this further. The other molecules investigated in Fig. 2.3.9, lie in regions that are suspected not to see greater exciton density with the inclusion of the dipole-quadrupole interactions, and thus far this, in general, remains the case. The exceptions being molecules 287 and 338, for which the coupling to 313 was actually stronger with the dipole-quadrupole interactions included.

From these initial investigations, it appears that the dipole-quadrupole interactions do indeed have an influence on the dynamics of the energy transfer process. While the plots of the dynamics suggest that there is a key relationship between the relative positions of the molecules and the contributions of the dipole-quadrupole interactions, this has yet to be fully understood and requires further work to fully appreciate the strength of the influences and where they occur. Regardless of this, the population data clearly shows a difference in the exciton dynamics driven by the coupling descriptions employed in this work. For sites close to the centre, where the exciton density is localised at the start, it appears that a coupling described by consideration of dipole-dipole interactions alone, may overestimate the dynamics of energy transfer, which is in contrast to the results reported by Zheng *et al.* on QD systems. Therefore the higher order terms of the multipole expansion may be influential in accurately describing the coupling between species and the subsequent energy transfer, however more work is required to fully appreciate their effect and understand their influence in particular systems.

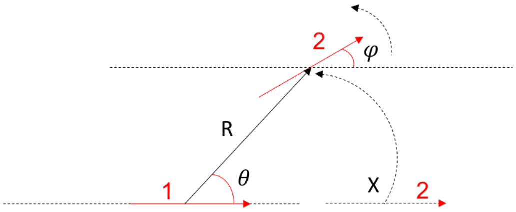

Figure 2.3.10: Schematic of the angles and routine performed to investigate the coupling as a function of the orientation and position of the donor–acceptor pair. X is the point at which $\theta = 0^\circ$ and $\varphi = 0^\circ$. R is the intermolecular separation.

2.3.3 The Orientational Impact of the Dipole-Quadrupole Term

While consideration of the exciton dynamics at long times did appear to illustrate some effects of including the dipole-quadrupole coupling term, much of the detail was lost by considering the lattice of randomly oriented molecules. As shown by the examination of the exciton population at selected sites, the next order terms in the description of the coupling can have a significant impact. These effects are saturated out when considering the whole lattice, and the real implication of the differences seen at individual sites is complicated by the fact that the relevant orientations of those molecules and of that at the centre are not known. Therefore, the strength of the coupling between a pair of the same molecules (TC cyanine dye molecules) is now examined as a function of the position and relative orientation between them. Please also note that in the figures $M^{dddq} \equiv M^{full}$.

The procedure that has been implemented computationally has one molecule remaining stationary with the same orientation throughout the routine, while the position of the second molecule is rotated anti-clockwise about angle θ. For each position, the orientation of the second molecule is rotated anti-clockwise about angle φ. This approach is shown in Fig. 2.3.10.

Our investigations have focussed on the variations in the magnitude of the coupling as a function of this orientational and positional dependency of the donor–acceptor pair. The coupling described by the dipole-dipole term, the dipole-quadrupole term, as well as a combination of the two has been calculated for various combinations of orientations and positions of one molecule with respect to the other. In order to visualise the data, and because the rate of energy transfer is dependent on the square of the coupling, the square modulus of the various terms under consideration is investigated. It should be noted that this is a different scale to the one employed when examining the coupling landscapes over the full lattice of molecules. All values of the coupling given in the figures are in atomic units.

As before, the first result to be noted is that when the two molecules are identically oriented ($\varphi = 0°$ and $360°$), the dipole-quadrupole coupling is 0 for all possible position angles. As explained previously, this is as a result of the sign in the dipole-quadrupole term of Eq. (2.2.22). For a complete picture of the energy transfer process, the two possibilities of dipole-quadrupole coupling whereby the dipole of one molecule is the donor and the quadrupole of the second molecule is the acceptor and vice versa have been taken into account. It has been established that these two contributions to the description of the dipole-quadrupole coupling are to be taken away from one another [9,18] and as a result, when the donor and the acceptor have the same orientation, there is no dipole-quadrupole coupling between the two. Thus for a lattice of identically oriented molecules, which was considered earlier, the dipole-quadrupole contribution has no effect.

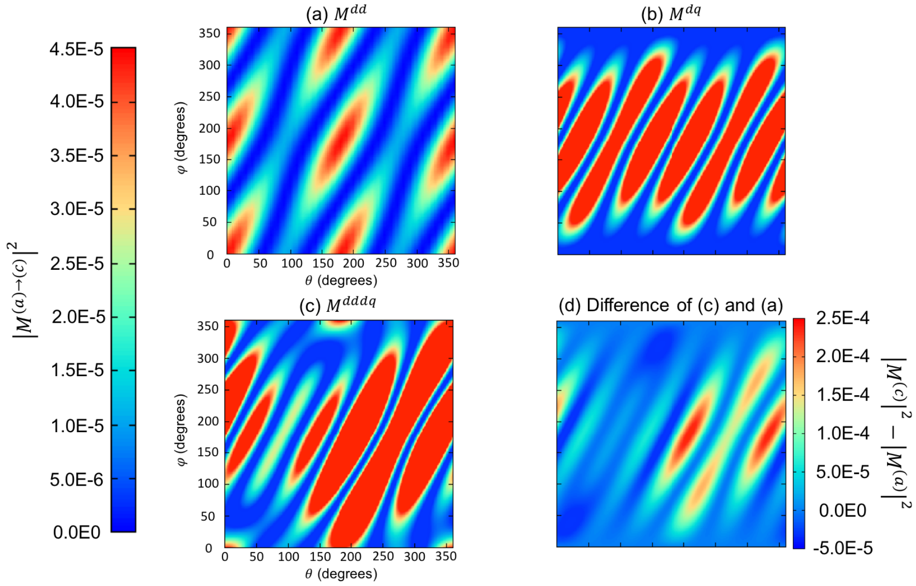

Figure 2.3.11: Square modulus of the coupling between a pair of molecules separated by 0.8 nm as a function of the position (θ) and orientation (φ) of one molecule with respect to the other. (a) The coupling described by the dipole approximation. (b) The coupling described by the dipole-quadrupole contributions alone. (c) The coupling described by the combination of the dipole-dipole and dipole-quadrupole coupling terms ($M^{dddq} \equiv M^{full}$). (d) The difference between plots (a) and (c).

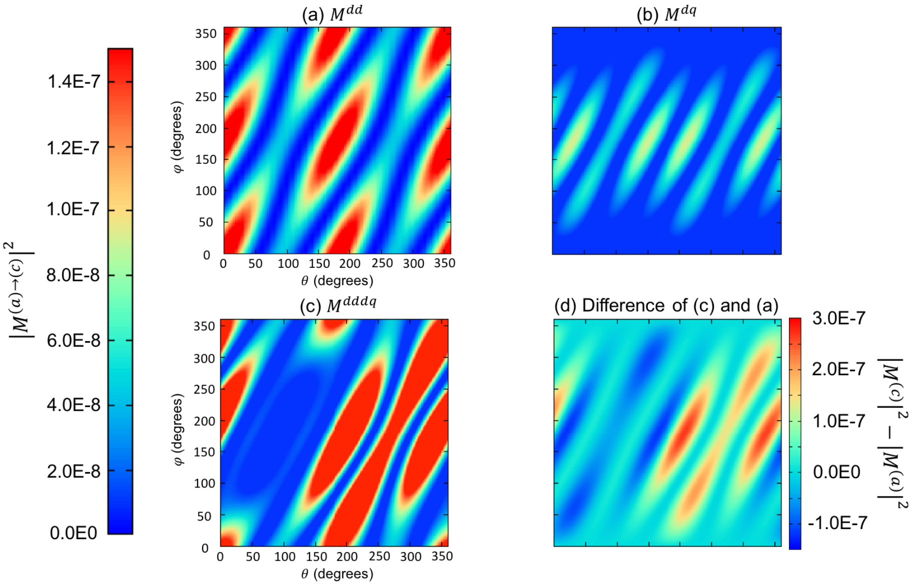

Figure 2.3.12: Square modulus of the coupling between a pair of molecules separated by 2.0 nm as a function of the position (θ) and orientation (φ) of one molecule with respect to the other. (a) The coupling described by the dipole approximation. (b) The coupling described by the dipole-quadrupole contributions alone. (c) The coupling described by the combination of the dipole-dipole and dipole-quadrupole coupling terms ($M^{dddq} \equiv M^{full}$). (d) The difference between plots (a) and (c).

To begin with two distances between the two molecules of 0.8 nm and 2.0 nm (Figs. 2.3.11 and Fig 2.3.12, respectively) are considered. From these sets of results it is apparent that an important combination of relative orientations and positions is centred around the angles $\theta = 90°$ and $\varphi = 180°$. As the distance is decreased from 2.0 nm to 0.8 nm, the coupling at this point increases more substantially than in other areas of the plots. This indicates that a pair of molecules in this region of relative orientation and position will see a more significant change in the rate of energy transfer as a function of the distance between them. The difference seen in this portion of the plots results from an interplay between the magnitude of the dipole-dipole and dipole-quadrupole coupling and their respective signs. At 2.0 nm separation, the dipole-dipole and dipole-quadrupole coupling have opposite signs but similar magnitudes. Therefore, when $M^{dddq}(\equiv M^{full})$ is calculated, its magnitude is small. At 0.8 nm, again, the two coupling terms have opposite signs, however, there is now a larger difference in the magnitude. As a result, $M^{dddq}(\equiv M^{full})$ increases significantly compared to that of the 2.0 nm calculation, indicating a more favourable coupling for EET.

A further point of interest is centred around $\theta = 270°$ and $\varphi = 180°$, where at both distances, there is an increase in the coupling on inclusion of the dipole-quadrupole contributions compared to consideration of the dipole-dipole coupling alone. This is shown in plot (d) of both Figs. 2.3.11 and 2.3.12. An increase in the coupling at $\theta = 200°$ and $330°$ on the horizontal line through the plot at $\varphi = 180°$ can also be seen.

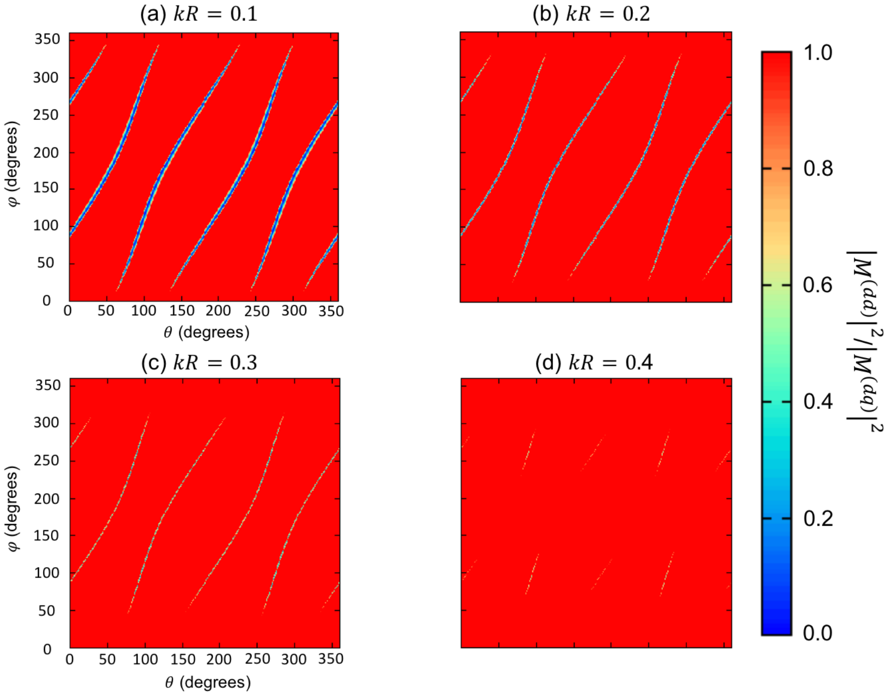

Figure 2.3.13: The ratio of the dipole-dipole and dipole-quadrupole square modulus couplings between a pair of molecules as a function of the position (θ) and orientation (φ) of one molecule with respect to the other for a series of kR values. (a) $kR = 0.1$ (b) $kR = 0.2$ (c) $kR = 0.3$ (d) $kR = 0.4$

Following on from this, in order to investigate when exactly the dipole-dipole approximation breaks down, further calculations were carried out in which the distance between the two molecules was varied based on a series of kR values ranging from 0.1 to 10.0 for an easier association to the near- and far-zones of energy transfer. To aid in the analysis, the ratio of $|M^{dd}|^2/|M^{dq}|^2$ has been taken. Selected plots are shown in Fig. 2.3.13. The colour scale of all four plots has been set to range from 0 to 1 in order to highlight the places where the dipole-quadrupole coupling is stronger than that of the dipole-dipole coupling. Although the calculation was carried out through to $kR = 10.0$, Fig. 2.3.13 only shows plots up to $kR = 0.4$. This is because it was found that beyond $kR = 0.5$, there are no instances where the square modulus of the dipole-quadrupole coupling is significantly larger than the square modulus of the dipole-dipole coupling. The energy transferred was taken to be 3.0 eV, thus a kR value of 0.5 corresponds to a distance of 32.89 nm between the two molecules.

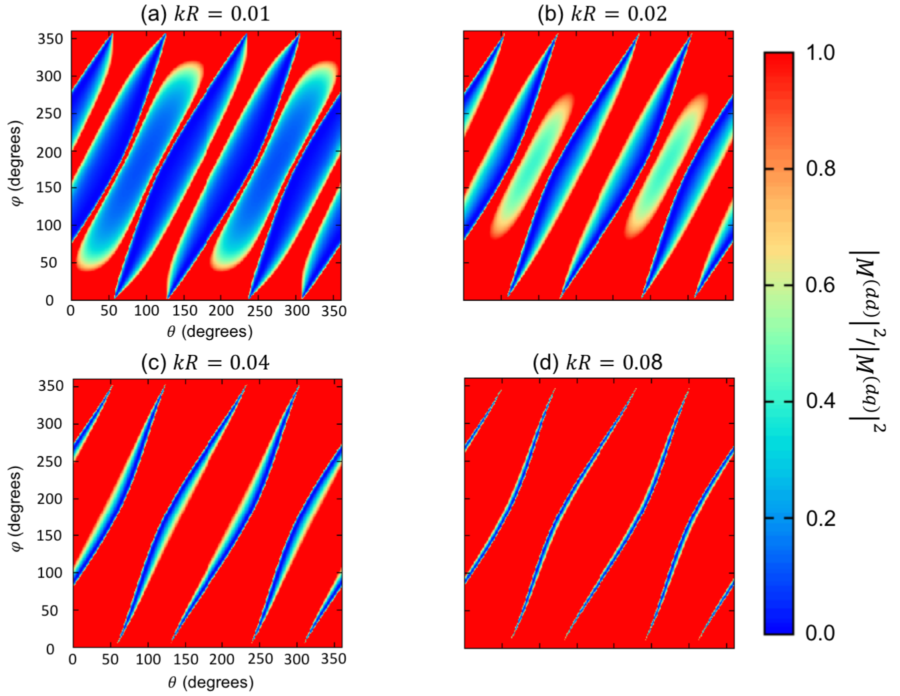

Figure 2.3.14: The ratio of the dipole-dipole and dipole-quadrupole square modulus couplings between a pair of molecules as a function of the position (θ) and orientation (φ) of one molecule with respect to the other for a series of kR values. (a) $kR = 0.01$ (b) $kR = 0.02$ (c) $kR = 0.04$ (d) $kR = 0.08$

We proceeded to look into the coupling in more detail, carrying out the same investigation for a series of values ranging from $kR = 0.01$ to $kR = 0.1$. Selected plots are shown in Fig. 2.3.14. As can be seen in Fig. 2.3.14 (a), which corresponds to a distance between the molecules of 0.66 nm, there are many combinations of relative orientation and position where the square modulus of the dipole-quadrupole coupling is significantly larger than that of the dipole-dipole coupling. From Fig. 2.3.14 (b), at $kR = 0.02$ (and therefore R = 1.32 nm), it appears that the dipole-quadrupole contributions may prove to be important in providing accurate descriptions of the coupling at the same sort of distances encountered between quantum dots in nanomaterials.

From these plots, it appears that, while the dipole-quadrupole contributions are seen to have an effect at distances from $kR = 0.4$ and below, the dipole approximation really begins to break down from around $kR = 0.05$. This corresponds to a distance of 3.29 nm. The importance of the curved line regions that remain above $kR = 0.05$ where the dipole-quadrupole coupling remains stronger than the dipole-dipole coupling is yet to be determined.

Although not immediately apparent when considering a large lattice of molecules, it has been shown that the inclusion of the next order terms involving the transition quadrupole moment in the description of the coupling between two species can have a significant impact. The results suggest that, while in a broad setting the quadrupole terms have a small influence on the overall landscape of the coupling, for certain combinations of different orientations and positions of a donor–acceptor pair their inclusion is of increased importance for an accurate description of the rate of energy transfer between them. Through these plots it has also been observed that, irrespective of the relative orientations and positions, the dipole-quadrupole coupling also has an impact at appreciable distances that are relevant in some nanomaterials. Overall, this work highlights the importance of including the next highest order terms in the description of the coupling in order to create more complete depictions of the rate of energy transfer. In addition, the orientational and positional dependency of the coupling terms may provide design cues for the fabrication of new materials that contain a strong quadrupole moment in order to optimise the rate of energy transfer. In this work, the transition of the TC cyanine dye molecule that has been considered has a well-defined transition dipole moment. In the future, the techniques presented here could readily be extended, first by examining a transition that isn't dominated by a dipole and secondly by exploring alternative molecules that are already known to have properties influenced by the transition quadrupole moment, such as hexahelicenes [81].

3

The Transition Quadrupole Moment and its Relation to Light

3.1 Introduction

Thus far the focus of this thesis has been centred around the transition quadrupole moment in the multipole expansion of the transition density associated with a chromophore and its importance in the description of the electronic coupling that governs the process of energy transfer. However, the significance of the higher order multipole terms isn't just realised in the coupling of two chromophores. Whether it is in the interaction between an electric quadrupole moment and electric fields generating quantum effects in a particle [82], or the fundamental link between the angular momentum properties of emitted electromagnetic radiation and the multipolar form of the transition density [83], the transition quadrupole moment has a lot to offer. The angular momentum of light, particularly that of so-called structured light which is light enriched with orbital angular momentum (OAM) beyond the separate spin angular momentum (SAM) associated with its polarisation, has attracted a great deal of attention in recent years [83–86]. The wide-ranging applications makes it a prosperous area of research. Further studies look to explore the interaction of light endowed with OAM and molecules [87–90]. The emission and absorption of an optical vortex and the transference of the OAM to the electronic motion of a chromophore is predominantly described through electronic transition moments of the quadrupole order and above [89, 91–93]. Once thought to be the only way a transfer of OAM could occur with the internal motion of matter, recent work by Forbes highlights this notion as being an artefact of the paraxial approximation and in the correct conditions (i.e. non-paraxial fields) the transfer of OAM can occur via dipole moments [94]. Importantly, however, electronic quadrupole transitions can play a notable role in the description of structured light. As such, examining the properties of the transition moment and viewing the emitted electromagnetic radiation not only affords the possibility of unique theoretical insight, but also offers potential of a practical importance with certain photonics applications.

Work published by Williams *et al.* showed that light endowed with OAM could be generated from the relaxation of a delocalised electronic exciton state that results from a particular arrangement of three or more chromophores [95, 96]. This light possessing a vortex, or so-called twisted light, was shown theoretically to result via consideration of the transition dipole moments of each molecule providing they are suitably placed so as to adhere to a certain set of symmetry groups [95, 96].

Rice *et al.* recently identified the spatial development in amplitude of the most common form of multipolar emission [72]. They highlighted the distinctive near-zone ($kR \ll 1$) properties of light and underlined the significant change in character as one moves to the far-zone where the distances involved are much greater than the optical wavelength. Initially, they consider the spatial and temporal development of the field emitted from an electric dipole, presenting equations for the electric field and plotting the transverse electric field in what is Fig. 1 of their work [72]. This shows the variation in the magnitude and phase of the field over a two-dimensional area with the dipole situated at the centre. They go on to examine the radial distribution of the magnitude of the electric field from an electric quadrupolar source, however they do not produce a figure similar to that of their Fig. 1 and thus do not show the development of the phase of the electric quadrupole radiation. Inspired by the fundamental connection with the OAM of light beams, in this chapter we take a step back from EET to explore the very nature of the transition quadrupole moment itself. This is achieved by obtaining the transition quadrupole moment matrix of a suitable atomic transition and subsequently examining the phase of the electric field that is emitted by such a multipole.

3.2 Theory

A full derivation of the theory employed in this chapter can be found in Refs. [68, 72]. Examining the work of Rice *et al.*, we see that their investigations into the radial properties of the electric field from different multipolar sources starts with the development of a formulation of emission and detection using QED [72]. Helpfully, as this surmounts to a transfer of energy, the theory is equivalent to the that previously presented in this thesis relating to EET, only now the photon being passed from the donor to the acceptor is considered to be real. The key equations pertinent to the theory and work discussed in this chapter are given below for the reader's convenience.

In order to examine the electric field emanating from an electric quadrupole source, Rice *et al.* evaluate the scenario whereby the emitted radiation is subsequently picked up by a dipole detector [72]. As such, it is, once again, the dipole-quadrupole coupling that is to be inspected. The interaction Hamiltonian presents itself as the most important Hamiltonian term in the complete description of the system and in the multipolar formalism employing the Coulomb gauge, is expressed as [36, 97]

$$H_{int} = -\varepsilon_0^{-1} \sum_{\xi} [\boldsymbol{\mu}(\xi) \cdot \boldsymbol{d}^{\perp}(\boldsymbol{R}_{\xi}) + \Theta_{\alpha\beta}(\xi) \nabla_{\alpha} d_{\beta}^{\perp}(\boldsymbol{R}_{\xi})], \tag{3.2.1}$$

where $\Theta_{\alpha\beta}(\xi)$ is the electric quadrupole operator for molecule ξ and $\boldsymbol{\mu}(\xi)$ is the electric dipole operator. The transverse electric field displacement operator, $\boldsymbol{d}^{\perp}(\boldsymbol{R}_{\xi})$ (in vacuum form) evaluated at the position of molecule ξ ($\boldsymbol{R}_{\xi}$), is given by [36, 97]

$$\boldsymbol{d}^{\perp}(\boldsymbol{R}_{\xi}) = i \sum_{\boldsymbol{p},\lambda} \left(\frac{\hbar c p \varepsilon_0}{2V} \right)^{\frac{1}{2}} [\boldsymbol{e}^{(\lambda)}(\boldsymbol{p}) a^{(\lambda)}(\boldsymbol{p}) e^{i\boldsymbol{p}\cdot\boldsymbol{R}_{\xi}} - \bar{\boldsymbol{e}}^{(\lambda)}(\boldsymbol{p}) a^{\dagger(\lambda)}(\boldsymbol{p}) e^{-i\boldsymbol{p}\cdot\boldsymbol{R}_{\xi}}], \tag{3.2.2}$$

where the sum is taken of all possible wave-vectors $\boldsymbol{p}$ and polarisations λ with the polarisation vector given by $\boldsymbol{e}^{(\lambda)}(\boldsymbol{p})$ and $a^{(\lambda)}(\boldsymbol{p})$ and $a^{\dagger(\lambda)}(\boldsymbol{p})$ are the annihilation and creation operators, respectively. Whether it is dipole-dipole coupling or dipole-quadrupole coupling, the quantum amplitudes for each interaction are often expressed in terms of the Green's function [38, 69, 98], for example the dipole-quadrupole interaction appears as

$$M^{dip-quad} + M^{quad-dip} = \frac{1}{4\pi\varepsilon_0}[\mu_\alpha^D \Theta_{\beta\gamma}^A - \Theta_{\beta\gamma}^D \mu_\alpha^A]\nabla_\gamma(\nabla^2\delta_{\alpha\beta} - \nabla_\alpha\nabla_\beta)G(k,R), \tag{3.2.3}$$

where

$$G(k,R) = \frac{e^{ikR}}{R}, \tag{3.2.4}$$

and consideration has been taken for the two scenarios whereby the dipole is the donor and the quadrupole is the acceptor and vice versa. As can be seen, the Green's function term remains the same for both scenarios and an interpretation of how this equation works for both is easily be gained by considering the order of operations.

After completing the vector calculus in Eq. (3.2.3), Scholes and others arrive at a simple expression for the complete quantum amplitude, which for the electric quadrupole-electric dipole interaction is

$$M^{dip-quad} + M^{quad-dip} = [\mu_\alpha^D \Theta_{\beta\gamma}^A - \Theta_{\beta\gamma}^D \mu_\alpha^A]V_{\alpha\beta\gamma}(k,\boldsymbol{R}), \tag{3.2.5}$$

with the full derivation provided elsewhere [69, 73]. As before, the full quantum amplitude has been split into two parts in order to account for both possible scenarios whereby the dipole could be the donor and the quadrupole is the acceptor and vice versa. Based on the problem set forth by Rice *et al.* it is clearly the second term in Eq. (3.2.5) that is considered most important, as that indicates emission from a quadrupole (the donor, D) with detection by a dipole (the acceptor, A). As we shall see, for this work investigating the emitted field the detector is not considered and the fact that there are two terms in Eq. (3.2.5) is unimportant here. As per Scholes *et al.*, the coupling tensor in truth encapsulates the vector calculus of the Green's function, via the expression $V_{i_1 i_2 \cdots i_n} = \nabla_{i_1} \cdots \nabla_{i_{n-2}}(\nabla^2\delta_{i_{n-1}i_n} - \nabla_{i_{n-1}}\nabla_{i_n})\frac{e^{ikR}}{R}$ [69]. Once the vector calculus has been performed, the dipole-quadrupole coupling tensor, as it is in Chapter 2, is given by

$$\begin{aligned} V_{\alpha\beta\gamma}(k,\boldsymbol{R}) = &\frac{ik^4}{4\pi\varepsilon_0}\left[\delta_{\alpha\beta}\hat{R}_\gamma h_1^{(1)}(kR) - \frac{1}{kR}\left(\delta_{\alpha\beta}\hat{R}_\gamma + \delta_{\alpha\gamma}\hat{R}_\beta + \delta_{\beta\gamma}\hat{R}_\alpha\right) h_2^{(1)}(kR)\right. \\ &\left. + \hat{R}_\alpha\hat{R}_\beta\hat{R}_\gamma h_3^{(1)}(kR)\right]. \end{aligned} \tag{3.2.6}$$

The tensor is defined using particular functions $h_1^{(1)}(kR)$, $h_2^{(1)}(kR)$, and $h_3^{(1)}(kR)$. Rice *et al.* report these as being spherical Bessel functions, and while they are indeed spherical Bessel functions of the third kind, it is much more helpful for use with computational programs and libraries such as Mathematica [99] and Numpy in Python [100], to label these as spherical Hankel functions of the first kind. These can be given in terms of ordinary Hankel functions ($H_n^{(1)}(z)$) by $h_n^{(1)}(z) \equiv \sqrt{\frac{\pi}{2z}} H_{n+(1/2)}^{(1)}(z)$ or via spherical Bessel functions of the first and second kind ($j_n(z)$ and $n_n(z)$, respectively) by the relation $h_n^{(1)}(z) = j_n(z) + i n_n(z)$ [101]. The functions of interest are given by [71]

$$\begin{aligned} h_1^{(1)}(kR) &= -e^{ikR}\left(\frac{1}{kR} + \frac{i}{k^2R^2}\right) \\ h_2^{(1)}(kR) &= e^{ikR}\left(\frac{i}{kR} - \frac{3}{k^2R^2} - \frac{3i}{k^3}R^3\right) \\ h_3^{(1)}(kR) &= e^{ikR}\left(\frac{1}{kR} + \frac{6i}{k^2R^2} - \frac{15}{k^3R^3} - \frac{15i}{k^4R^4}\right). \end{aligned} \tag{3.2.7}$$

It should be noted that the integer multiplier of i in the second term in the brackets associated with the equation for $h_3^{(1)}(kR)$ is different to that presented in both of the papers in which these functions have been used within the context of quadrupole-dipole coupling in a QED context [69, 72]. Through a built-in function of Mathematica [99], namely `SphericalHankelH1` it has been confirmed that the equation given here in this work is the correct version.

Although thus far the theory has been built around the same RET formulation encountered in Chapter 2, we are now turning our attention to investigating the emitted fields from the higher order transition multipole moments, for the time being limiting ourselves to the quadrupole. The reason why the fact there are two contrariwise terms in Eq. (3.2.5) is deemed unimportant is because the electric field associated with a quadrupole transition is given by the expression $E_\alpha^{quad} = \Theta_{\beta\gamma} V_{\alpha\beta\gamma}(k, \boldsymbol{R})$. As can be seen, the detector is not considered and $V_{\alpha\beta\gamma}(k, \boldsymbol{R})$ is the same for both terms in Eq. (3.2.5). Performing the double contraction gives

$$\begin{aligned} E_\alpha^{quad} =& \frac{ik^4}{4\pi\varepsilon_0}\left[\Theta_{\alpha\gamma}\hat{R}_\gamma h_1^{(1)}(kR) - \frac{1}{kR}(\Theta_{\alpha\gamma}\hat{R}_\gamma + \Theta_{\beta\alpha}\hat{R}_\beta + \Theta_{\gamma\gamma}\hat{R}_\alpha)h_2^{(1)}(kR)\right. \\ & \left. +\Theta_{\beta\gamma}\hat{R}_\alpha\hat{R}_\beta\hat{R}_\gamma h_3^{(1)}(kR)\right]. \end{aligned} \tag{3.2.8}$$

As Rice *et al.* go on to declare 'since the dummy indices are arbitrary and the transition quadrupole moment is traceless', the equation can be simplified to give Eq. (3.2.9) [72],

$$E_\alpha^{quad} = \frac{ik^4}{4\pi\varepsilon_0}\left[\Theta_{\alpha\gamma}\hat{R}_\gamma\left(h_1^{(1)}(kR) - \frac{2}{kR}h_2^{(1)}(kR)\right) + \Theta_{\beta\gamma}\hat{R}_\alpha\hat{R}_\beta\hat{R}_\gamma h_3^{(1)}(kR)\right]. \tag{3.2.9}$$

The phase of the electric field is then found by taking the argument of the complex number, returning the angle, typically in radians, from the positive real axis (counterclockwise) on the complex plane. As Rice *et al.* explain in their description associated with the dipole emission, the actual calculation of the phase is to take the inverse tangent (arctangent) of the ratio of the imaginary and real parts of the electric field [72]. With this, the phase (or argument) of the electric field in a particular direction (x, y, or z) can be plotted. It is noted that Williams *et al.* also employ this same calculation in their work plotting the phase of the electric field emitted from as series of chromophore arrays [95, 96].

Although we have obtained the equation for the electric field by considering the interaction of a dipole and a quadrupole and the associated coupling tensor $V_{\alpha\beta\gamma}$, it should be made clear once more that the electric field that is emitted is independent of the acceptor molecule [72]. While starting from the coupling between two molecules provides a useful narrative to the theory required to generate an equation for the electric field, it may give the impression that the electric field emitted is dependent on the acceptor.

Although the work presented here is focussed on the transition quadrupole, it is noted in passing that the electric field for dipole emission is calculated in a similar way, with $E^{dip}_{\beta} = -\mu^{D}_{\alpha} V_{\alpha\beta}(k, \boldsymbol{R})$ and the resulting equation after contraction is given by

$$E^{dip}_{\beta} = \frac{e^{ikR}}{4\pi\varepsilon_0 R^3}[3(\boldsymbol{\mu} \cdot \hat{\boldsymbol{R}})\hat{R}_{\beta} - \mu_{\beta}(1 - ikR) + \mu_{\beta} - (\boldsymbol{\mu} \cdot \hat{\boldsymbol{R}})\hat{R}_{\beta} k^2 R^2]. \qquad (3.2.10)$$

3.3 Computational Details

A three-month research visit to Colorado School of Mines in Golden, Colorado, USA was made possible through a Researcher Mobility Grant provided by the Royal Society of Chemistry (RSC). Started during that trip as part of a collaboration with Professor Mark T. Lusk, the Mathematica [99] program has been used to create a straightforward notebook that codes for the calculation of the electric field via Eq. (3.2.9). The phase of the z component of the electric field is then subsequently plotted. As input, the specialised Mathematica [99] code only requires data for a specific transition quadrupole moment in order to create a plot of the phase in a 2D plane. Through these plots we start an investigation into the precise nature of radiation emanating from a transition quadrupole moment and the relationship to structured light. A separate corresponding notebook has been created for the calculation of the emitted field from a transition dipole moment using Eq. (3.2.10). Its structure is identical to the main file of the transition quadrupole moment with the only difference being the transition multipole moment data that has to be entered.

The notebook begins by defining a couple of parameters, the wave vector (the magnitude of, k) and Coulomb's constant ($\frac{1}{4\pi\epsilon_0}$), in Atomic Units such that they both equal 1. The transition quadrupole moment is a symmetric matrix and although not always the case, as Rice *et al.* point out it can also be a traceless matrix [72]. This is because the traceless version omits the spherical component and any experimental measurement will only observe the part that is different from spherical because $\nabla \cdot E = 0$. The code is therefore set up such that just six elements of the 9x9 matrix are required as input to yield the full transition quadrupole moment. A position vector is then defined for the position of the 'molecule' and this is simply set to be the origin, `{0,0,0}`. While the position of a so-called absorption plane, the x, y-plane in which the phase of the electric field will be visualised, can be given at some distance above the transition moment along the z-axis (`zvec={0,0,z0}` where `z0=2`, for example), further refinement of the code led to a more generic implementation such that the electric field could be calculated at any point requested via three Cartesian coordinates.

Now that the scene has been set, the code proceeds to calculate the electric field. Looking at Eq. (3.2.9) (and Eq. (3.2.10)), having already defined the magnitude of the wave vector and Coulomb's constant, all that remains is to determine the vector between the position of the 'molecule' and the position at which the electric field will be calculated (the $\boldsymbol{R}$ vector). It is at this stage that variables such as the position vector are defined as functions which take the arguments x, y and z, the Cartesian coordinates of the point at which the electric field is to be calculated. The position vector of this point can either be defined by using the absorption plane, `{x,y,0}+zvec` or in the more general implementation, the position vector is simply given by the Cartesian coordinates of the point at which we want the calculation to take place, `{x,y,z}`. The $\boldsymbol{R}$ vector function is then defined, alongside its magnitude and the unit vector. The spherical Hankel functions are then calculated directly by coding for Eqs. (4.2.22). Although the built-in spherical Hankel functions (`SphericalHankelH1`) of Mathematica [99] could have been employed, as was the case when confirming an error seen in the equation for $h_3^{(1)}(kR)$, at the time, it was desired that the code matched up with all of the equations set forth in the theory. Finally, the Cartesian components are defined as functions at a given point, `{x,y,z}` with the calculation coded from Eq. (3.2.9) (or Eq. (3.2.10) in the case of investigating emission from a transition dipole moment). The phase of one of these Cartesian components of the electric field is then calculated and the data plotted in a 2D-plane using the function `ContourPlot`. Ultimately, through this Mathematica [99] notebook, the phase of any Cartesian component of the electric field can be calculated and viewed in any 2D plane (x, y, x, z, y, z). Since the convention in Refs. [72, 95, 96] is to plot the phase in the x, y-plane (for Refs. [95] and [96] this is based on symmetry arguments), the same plane has been chosen for this work, specifying that the viewer is looking down the z-axis. As a result, it was deemed sensible to focus on calculating the phase of the electric field through its z component.

The transition quadrupole moment matrix (or transition dipole moment vector) can easily be changed and is discussed in more detail below, however, it must be noted that this needs either to be known or calculated separately.

3.4 Results and Discussion

3.4.1 Selection of a Transition Quadrupole Moment

The plots presented in this section predominantly explore the phase of the z component of the electric field, while looking along the z-axis. However, before being able to plot the phase of the electric field, one needs to have a transition dipole moment vector, or a transition quadrupole moment matrix to hand. Initially, some fun was had arbitrarily choosing the six elements needed to build a symmetric and traceless matrix. At the time it was naively hoped that the impact of each element of the matrix could be discerned through the observations from a series of plots of the phase of the electric field. Although interesting as part of the build process, it was quickly established that no conclusions would ever be drawn as it was unclear as to how appropriate any one randomly chosen matrix would be. It is hoped that the research presented in this chapter could provide some fundamental insights into the nature of the radiation associated with the emission from a transition quadrupole moment. Clearly, in order to yield results that offered a greater potential for interpretation, it is of most benefit to consider a known transition quadrupole moment. In Chapter 2 transition quadrupole moment data was obtained for a molecule that was known to be incredibly relevant when studying the process of resonance energy transfer (RET). Before proceeding any further, solely out of curiosity, the phase of the z component of the electric field was calculated using the transition quadrupole matrix data presented in Table 2.3.3 of Chapter 2. Interestingly, while symmetric, the quadrupole moment matrix obtained from the Gaussian 09 [77] calculation is not traceless and it remains this way even after its manipulation as per the discussion in Chapter 2. Although not in its traceless form, the phase was plotted in the x, y-plane and the result is shown in Fig. 3.4.1.

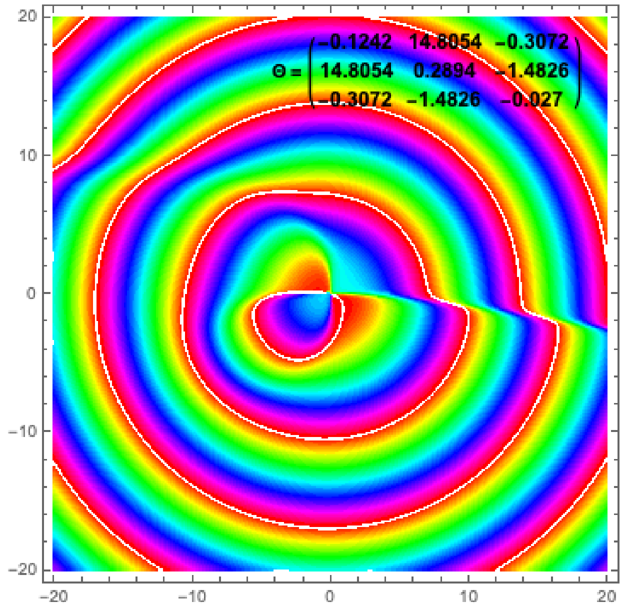

Figure 3.4.1: Plot of the phase of the z-component of the electric field emitted by the transition quadrupole moment associated with the transition of the TC cyanine dye molecule utilised in Chapter 2. The matrix for the transition quadrupole moment of this transition is superimposed in the top right.

While the phase shows some resemblance to a continuous spiral, it is far from smooth and upon reexamination of the output from the Gaussian 09 [77] calculation, this could be because the transition under investigation in the previous work was not a purely quadrupole transition. So although interesting to look at, there is not a lot to be learned from the plot in Fig. 3.4.1. Therefore, due to the fundamental nature of the research being presented in this chapter, it was decided that the most prudent approach for this investigation was to construct transition quadrupole matrices through the consideration of atomic transitions that are dipole-forbidden but do engage an electric quadrupole. Prior to this, we start by examining the selection rules and in turn start to focus on the connection with angular momentum that is so important in the discussions of structured light. For a dipole-allowed transition, the atomic spectroscopic selection rules are:

- $\Delta\ell = \pm 1$ — the Laporte selection rule — the azimuthal quantum number, or orbital quantum number that represents the magnitude of the orbital angular momentum, must change by 1.

- $\Delta m_\ell = 0, \pm 1$ — the magnetic quantum number, which represents the projection of the orbital angular momentum along a specified axis, can change by zero or 1.
- $\Delta m_s = 0$ — the electronic spin quantum number, which gives the projection of the spin angular momentum along a specified axis, does not change.

Given the selection rules presented above, a change in orbital angular momentum of more than 1 for the electron is dipole-forbidden. It is known that the selection rule for a quadrupole-allowed transition is $\Delta\ell = \pm 2$. The change in ℓ corresponds to a transition between particular orbitals. The simplest case for a change in ℓ of ± 2 is a transition from a d orbital ($\ell = 2$) to an s orbital ($\ell = 0$). For the s orbital, $m_\ell = 0$, while the set of d orbitals have $m_\ell = -2, -1, 0, 1, 2$. These, therefore, are the transitions that are to be considered in this work, and through the calculation of the transition quadrupole matrix elements means the results presented here simply consider the fields emitted by the hydrogen atom. A couple of Mathematica [99] notebooks were provided by Professor Mark T. Lusk, one for calculating the transition dipole moments of the hydrogen atom and the other for the transition quadrupole moments. It is only the latter that are considered in the results presented below and the calculation involved is the integration over all space shown in Eq. (3.4.1) for a one electron transition between the 3 and 1 energy levels, with the charge q equal to -1. However it is noted that the notebook was purely utilised as provided to yield the transition quadrupole matrices for the five possible transitions from the $3d$ orbitals to the $1s$ orbital of the hydrogen atom.

$$\Theta = q \int_{\text{all space}} \psi^*_{final}(3r_i r_j - ||\vec{r}||^2 \delta_{ij})\psi_{inital} dV \tag{3.4.1}$$

3.4.2 Observing the Electric Field Associated with Quadrupole Emission from the Hydrogen Atom

The five separate matrices calculated through the separate Mathematica [99] notebook have been applied to plot the phase of the z component of the electric field emitted from a corresponding transition quadrupole moment. The results can be seen in Figs. 3.4.2–3.4.7. The transition quadrupole matrix used to produce each plot has been superimposed in the top right of each figure.

The m_ℓ values represent the projection of the orbital angular momentum associated with each ℓ orbital along a specified axis. Therefore, with every transition from one of the five d orbitals to the single s orbital, the change in orbital angular momentum along that specified axis is indicated by the change in m_ℓ value. This means that a transition between the set of d orbitals and the s orbital may be accompanied by a change in (orbital) angular momentum along a specific axis of $0, \pm\hbar, \pm 2\hbar$. For all of the five transitions, the change in the orbital angular momentum quantum number will be equal to 2, as we are going from a d orbital ($\ell = 2$) to an s orbital ($\ell = 0$).

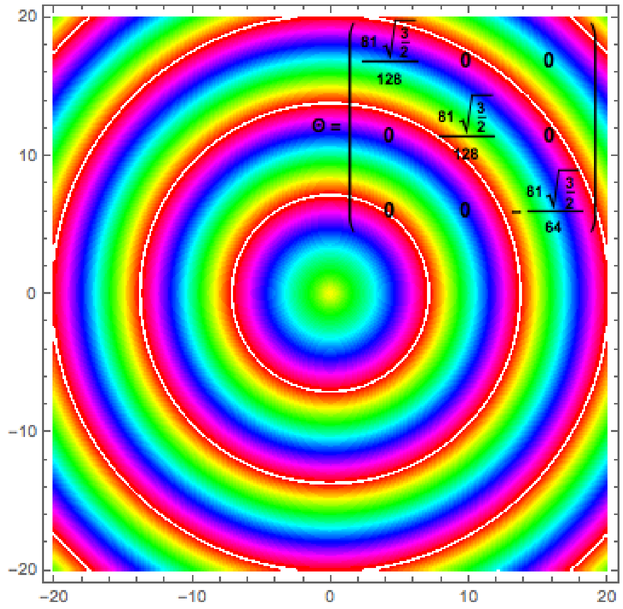

Figure 3.4.2: Plot of the phase of the z component of the electric field emitted by the transition quadrupole moment associated with the transition between the $3d_0$ and $1s$ atomic orbitals of hydrogen, looking down the z-axis. The matrix for the transition quadrupole moment of this transition is superimposed in the top right.

As per convention, when referring to the m_ℓ values, the axis of projection is the z-axis, and therefore the axis to be considered when examining the electric field is also the z-axis. Figures 3.4.2–3.4.7 show the phase of the z component of the electric field emitted along the z-axis by a quadrupole transition. The results seem to suggest that for certain transitions light may be generated with orbital angular momentum, and in all cases the number of units of OAM that the light possesses agrees precisely with the change in m_ℓ seen for the corresponding transition. Consider Fig. 3.4.2 in which there is no twist in the phase. This has been interpreted as the emitted radiation containing no OAM for a transition that involves a $\Delta m_\ell = 0$. This is consistent with the conservation of angular momentum along the specified z-axis. Understanding exactly how angular momentum is imparted onto the photon can be problematic. Now, it is important to bear in mind that the orbital angular momentum change associated with the transition does not indicate the change of OAM for the photon. The photon carries one unit of angular momentum in terms of spin in the direction of propagation and for all the $3d \rightarrow 1s$ transitions. In order to fulfil the law of conservation of angular momentum, for the transition described by Fig. 3.4.2, an OAM of ± 1 will compensate for the SAM of ∓ 1 [89]. This is because angular momentum is conserved along one axis. What Fig. 3.4.2 is showing is merely the projection of the angular momentum on the z-axis. This is interesting as up until now, based primarily on the work of Williams *et al.*, the interpretation was that viewing the phase of the electric field will showcase any units of OAM. At the moment, this doesn't appear to be case. One possibility is that, since only the z-component of the electric field emitted in the z-direction is being considered, we know nothing of the x- and y-components along their respective axes. These contributions may well be seen to be carrying OAM, however quick simulations carried out thus far have suggested that this isn't the case.

A similar argument is presented on consideration of Fig. 3.4.3, whereby light is seen to be emitted with a double twist in the phase of the electric field. This is again consistent with the change in the m_ℓ value seen for the transition from the $3d_2$ orbital to the $1s$ orbital. Early thoughts led to the belief that this photon would have two units of OAM, however, this would be nonsensical. For the field emitted by the $3d_2 \rightarrow 1s$ transition portrayed in Fig, 3.4.3, as per the law of conservation of angular momentum, the units of OAM and SAM will add up to match $\Delta m_\ell = +2$ [89].

Interestingly, when one considers the $3d_{\pm 1} \rightarrow 1s$ transitions, although the change in ℓ remains two, the photon is only thought to carry the unit of SAM, and yet Figs. 3.4.4 and 3.4.5 both show a twist (opposite in nature) in the phase of the electric field. Given

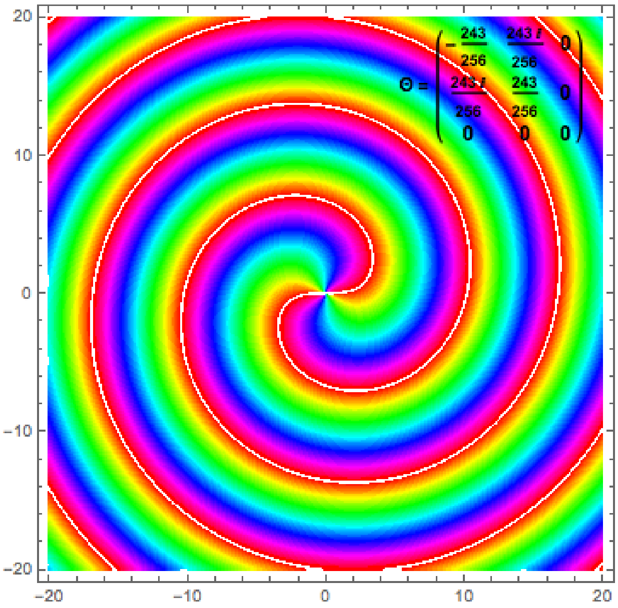

Figure 3.4.3: Plot of the phase of the z component of the electric field emitted by the transition quadrupole moment associated with the transition between the $3d_2$ and $1s$ atomic orbitals of hydrogen, looking down the z-axis. The matrix for the transition quadrupole moment of this transition is superimposed in the top right.

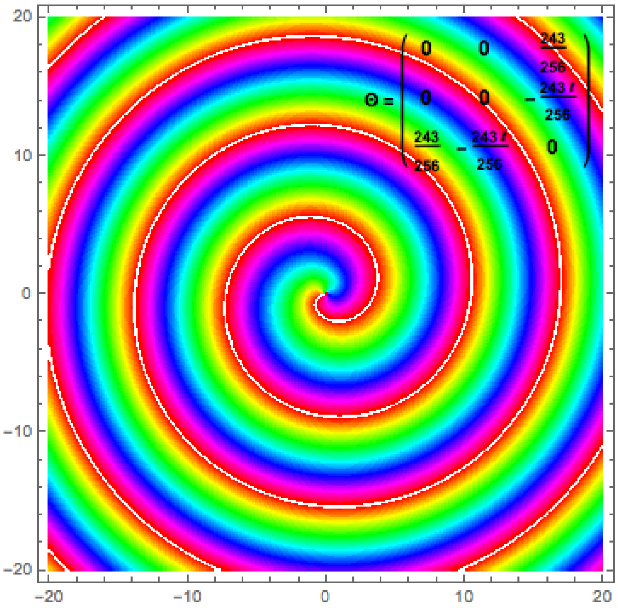

Figure 3.4.4: Plot of the phase of the z component of the electric field emitted by the transition quadrupole moment associated with the transition between the $3d_1$ and $1s$ atomic orbitals of hydrogen, looking down the z-axis. The matrix for the transition quadrupole moment of this transition is superimposed in the top right.

all of these results some questions do remain. Currently, the conservation of angular momentum is not fully comprehended for the $3d_{\pm1} \rightarrow 1s$ transitions and will require more thoughts. Beyond this, the fact that a twist is seen in the phase of the electric

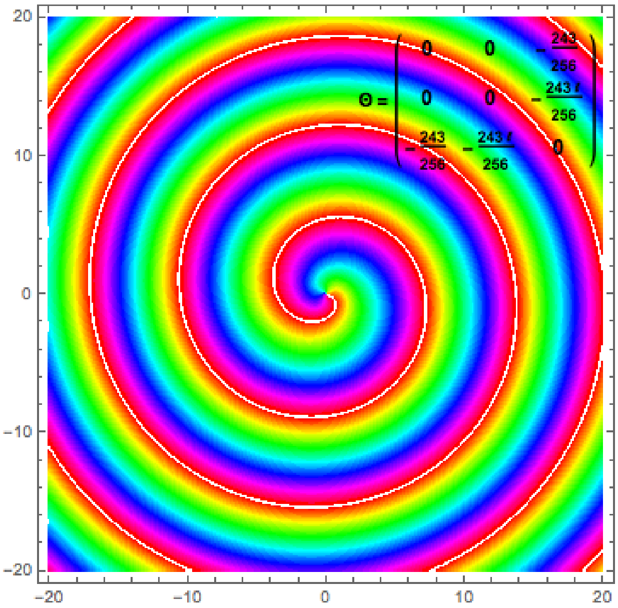

Figure 3.4.5: Plot of the phase of the z component of the electric field emitted by the transition quadrupole moment associated with the transition between the $3d_{-1}$ and $1s$ atomic orbitals of hydrogen, looking down the z-axis. The matrix for the transition quadrupole moment of this transition is superimposed in the top right.

field for the transitions involving the $3d_{\pm 1}$ orbitals (two twists in the cases of the $3d_{\pm 2}$ orbitals), leads to a question regarding whether the phase is able to discriminate between SAM and OAM. After our initial thoughts that a twist in the phase highlights units of OAM, these were somewhat unexpected results. Finally, it is pondered whether a better interpretation can be achieved by understanding the significance of the main axis. What is demonstrated by Figs. 3.4.2–3.4.5 is that the axis down which the field is viewed is key. Conventionally, SAM and OAM are discussed with respect to the direction of propagation. How this relates to the axis system and the choice of which Cartesian component of the electric field to utilise in the calculation of the phase, may prove to be inherent in the interpretation. Consider briefly Fig. 3.4.6. This is the phase of the electric field of the $3d_2 \to 1s$ transition as seen by looking down the z-axis (same as before), but with the phase calculated using the y component of the electric field. As can be seen this contains a twist.

Currently, it is not known what it means to examine the phase in such a way. Interestingly, through some experimentation it was found that the neat twists that appear in these plots seem only to do so when off-diagonal elements of the transition

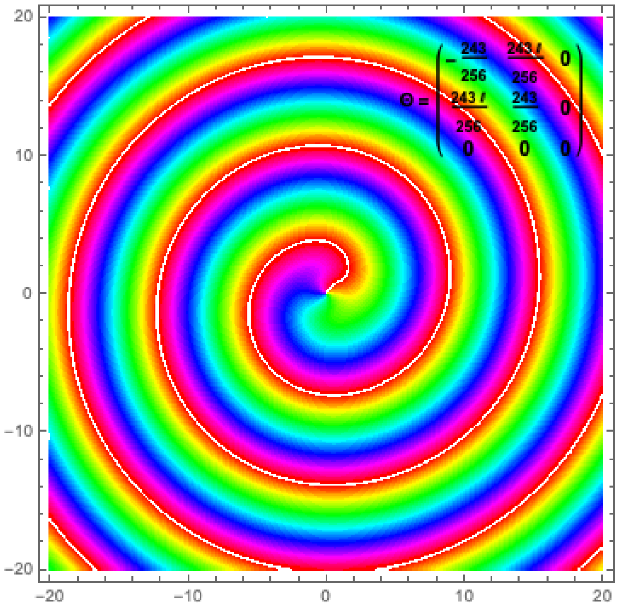

Figure 3.4.6: Plot of the phase of the y component of the electric field emitted by the transition quadrupole moment associated with the transition between the $3d_2$ and $1s$ atomic orbitals of hydrogen, looking down the z-axis. The matrix for the transition quadrupole moment of this transition is superimposed in the top right.

quadrupole matrix are imaginary. This has led to some interesting questions to be investigated in the future regarding the significance of viewing the orbitals in the spherical basis on a real axis (as required by the computer program). One could simply construct the transition quadrupole matrices of the 'real' orbitals from the ones in the spherical basis and carry out the same analysis. However, in doing so ambiguity would be created in the value of m_ℓ for those orbitals, thus the neat twists may no longer be seen at all. Although not presented here, a brief calculation to create a 'real' orbital transition from the $3d_{\pm 2} \rightarrow 1s$ transitions plus subsequent plotting of the phase in the same manner as before, produced a plot with four distinct segments with phase boundaries running along the diagonals. Broadly speaking it could be argued that it seemed similar to 3.4.3 but now divided instead of being smooth with the twists. Unsurprisingly, it appears almost identical to the experimental plots plotted (but not shown) that replaced the imaginary components of the transition quadrupole matrix, again leading to the question of the significance of imaginary components in the descriptions of light that may exhibit a twist.

Consideration of the $3d_{-2}$ to $1s$ transition has been included for completeness and is

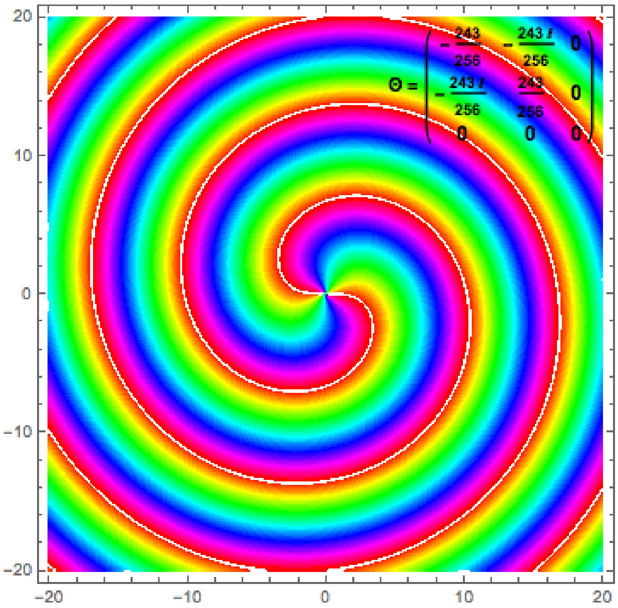

Figure 3.4.7: Plot of the phase of the z component of the electric field emitted by the transition quadrupole moment associated with the transition between the $3d_{-2}$ and $1s$ atomic orbitals of hydrogen, looking down the z-axis. The matrix for the transition quadrupole moment of this transition is superimposed in the top right.

shown in Fig. 3.4.7. Once again it can be seen that the angular momentum change along the axis is conserved, that is the change in m_ℓ matches the twist in the phase of the emitted light projected along the z-axis. The difference in comparison to the transition from the corresponding positive $3d_{m_\ell}$ orbital is an opposite rotation about the centre of the plot. As Williams *et al.* point out, a counterclockwise rotation, as seen in Figs. 3.4.4 and 3.4.3, is consistent with a positive angular momentum, or topological charge (the number of wave-front twists per unit wavelength), while a clockwise rotation of the phase progression (Figs. 3.4.5 and 3.4.7) indicates a negative topological charge [95].

In conclusion, some fascinating results have been obtained that offer the potential to yield important insights into the electric field emitted by a transition quadrupole moment and the interpretation of its phase. Clearly angular momentum is conserved along the z-axis, as the twists (or lack thereof) seen in the phase of the electric field correlate with the change in m_ℓ for each of the associated transitions of the hydrogen atom. However more work is required in order to understand the significance of the axis and the meaning behind the twists seen in the phase in relation to the AM of the photon. All of this inspired the work of the next chapter.

4

Electric Fields, Structured Light and Vector Spherical Harmonics

4.1 Introduction

Understanding the exact nature of light and electromagnetic radiation in general, as well as finding ways to manipulate it, has occupied the minds of scientists for centuries. Central to it all is the ability to describe the electromagnetic fields of photons mathematically. Motivated primarily by the work presented in the previous chapter, a different approach to the calculation of the electric field was desired in order to be able to create alternate depictions of the electric field, especially of its phase. The aspiration was to gain a greater comprehension of the results that had been generated as well as offer up some new physical insights. Through the work of Grinter, a highly applicable and functionally beneficial theoretical description was discovered [102, 103]. By far the biggest advantage of this alternative representation is that it facilitates the identification of the connection between the nature of a photon in terms of its angular momentum (AM) and the individual terms in the expansion of the exponential factor in the description of the electromagnetic plane wave [102]. In other words, the multipole order of the radiation itself is far more readily distinguishable throughout the equations involved and these are derived in such a way as to also provide a description of photonic AM. All of this is achieved through the use of spherical Hankel functions (initially Bessel functions were employed) and vector spherical harmonics (VSHs), identifying the individual multipole terms simply through a set of quantum numbers [103]. Recent studies have utilised the theory to investigate the transfer of angular momentum between a quadrupole emitter and a dipole acceptor, and also develop a new formulation of the resonance energy transfer (RET) process [1, 104]. The latter work showcases a number of advantages over the conventional plane wave (PW) approach, including the use of the spherical polar coordinate system, a key facet that is intended to be heavily exploited in this work [1]. Described in more detail in the next section, the alternative approach to the description of electromagnetic radiation has been dubbed the spherical wave (SW) approach. Although useful in offering a natural way to consider structured light and its AM, as Grinter and Jones point out, the SW approach is most effective when considering highly symmetric and isotropic systems with the example relating to RET being condensed phase solutions [1]. It also lacks the generality of the PW approach meaning currently, the only suitable application in order to gain insights into the fundamental nature of electromagnetic radiation from higher order transition multipole moments is to consider atomic transitions [105]. As such we once again solely consider hydrogen-like transitions, as was the case in the previous chapter. Although not relevant for our present purposes, it is interesting to note that while the reliance on spherical symmetry is an important limitation to the application of the SW approach, work by Jones and Grinter do provide some hope that wider areas of application may be possible in the future with the use of group-theoretical algebra [105].

The reliance on spherical polar coordinates within this theory makes the SW approach an ideal description to explore and ultimately achieve the objective of creating alternative depictions of the electric field, especially of its phase. This leads to the fundamental question that has driven the research presented in this chapter which was ‘what does the phase of the electric field look like when viewed on the surface of a sphere?’. It is also hoped that the different approach could provide some clarity on the results of the work from the previous chapter. In Ref. [105], Jones and Grinter provide a review comparing the PW and SW descriptions of electromagnetic radiation analytically. It was quickly realised that by applying the SW approach to view the fields, the combination with the work presented in Chapter 3, which utilised the conventional PW approach, could serve as a practical extension to the comparison. As such, the work presented in this chapter evolved over time to comprise a far more extensive analysis of the existing literature, namely Refs. [102] and [103], to gain a greater comprehension of theory with a view to its computational implementation. This complementary research to the analytical work already published should offer further insights into both fundamental and practical questions surrounding optical processes and chemical physics. The end result then looks to showcase the results of observing the phase of the electric field on the surface of a sphere, a concept that is more naturally suited to the SW description.

This chapter is outlined as follows. It starts with a thorough analysis of the SW approach, predominantly through Refs. [102] and [103]. Section 4.3 provides a detailed description of the computer program that has been developed. Finally, Section 4.4 presents and analyses the outcomes of the code with plots of the electric field, its phase and the magnetic field.

4.2 Theory

In Chapter 3 multipolar radiation emanating from selected transitions of the hydrogen atom was examined by utilising the work of Rice *et al.* and Andrews *et al.* through an intuitive source–detector picture developed by means of the theory of molecular quantum electrodynamics (QED) [68, 72]. This formulation evolves by initially considering a description of quantised electromagnetic radiation in terms of a mode expansion (Eq. (3.2.2)) based on the set of plane wave solutions, Eq. (4.2.2), to the wave equation, Eq. (4.2.1) derived from Maxwell's equations [36, 67, 105],

$$\nabla^2 \boldsymbol{X} - \frac{1}{c^2}\frac{\partial^2 \boldsymbol{X}}{\partial t^2} = 0, \tag{4.2.1}$$

$$\boldsymbol{X} = \boldsymbol{X}_0 e^{i\boldsymbol{k}\cdot\boldsymbol{r} - \omega t}, \tag{4.2.2}$$

where $\boldsymbol{X} = \boldsymbol{A}, \boldsymbol{E}$ or $\boldsymbol{B}$, that is the vector potential, electric field or magnetic field, respectively, in regions free of charges and currents [105]. $\boldsymbol{X}_0$ is an associated constant amplitude factor, ω is the angular frequency and $\boldsymbol{k}$ the wave vector.

The theory and work detailed in Chapter 3 focussed on a source-based description of the electric field of electromagnetic radiation. In this chapter, the theory being utilised pays far greater attention to the description of the radiation itself before considering the source. As such, we start by exploring the exponential term seen in Eq. (4.2.2), the plane wave description of electromagnetic radiation. Neglecting time-dependence, it is common, though not always necessary, to cast this exponential term in terms of a well-known series expansion based on

$$\boldsymbol{e}_{1n} e^{i\boldsymbol{k}\cdot\boldsymbol{r}} = \boldsymbol{e}_{1n} \left[\sum_n \frac{(i\boldsymbol{k}\cdot\boldsymbol{r})^n}{n!} \right] = \boldsymbol{e}_{1n} \left[1 + i\boldsymbol{k}\cdot\boldsymbol{r} + \frac{(i\boldsymbol{k}\cdot\boldsymbol{r})^2}{2!} + \frac{(i\boldsymbol{k}\cdot\boldsymbol{r})^3}{3!} + \cdots \right]. \tag{4.2.3}$$

As per the convention, $\boldsymbol{e}_{1n}$ is the polarisation vector, referring to the direction of the electric field component of the radiating wave [36]. It is easily thought of in relation to linearly polarised light, where the electric field of the plane wave has a specific polarisation aligned along one of the Cartesian coordinate axes, with $n = x, y$ or z. Equally, that same plane wave can be expressed as a linear combination of left- and right-circularly polarised light such that for a plane wave propagating along the z-axis and polarised along the x-axis,

$$\boldsymbol{e}_{1x} e^{ikz} = \frac{1}{\sqrt{2}} (\boldsymbol{e}_{1+1} + \boldsymbol{e}_{1-1}) e^{ikz}, \tag{4.2.4}$$

with $\boldsymbol{e}_{1+1}$, the positive unit vector, where $n = +1$, representing left-circularly polarised light and $\boldsymbol{e}_{1-1}$, the negative unit vector ($n = -1$), representing right-circularly polarised light [106]. Considering this, it is easy to associate the 1 in the notation of $\boldsymbol{e}_{1n}$ with the spin angular momentum quantum number of the photon. However, the notation stems from the fact that in the formulation being employed later on in this chapter, a vector field has unit spin and using the notation $\boldsymbol{e}_{1n}$ proves to be useful when considering the coupling of angular momenta [106].

The combination of the exponential with $\boldsymbol{e}_{1n}$ makes Eq. (4.2.3) a series approximation of the electric field associated with a plane wave. Analogous to the multipole expansion of the potential of an electric charge distribution at some point outside of it that was discussed in Section 1.3, the separate terms of Eq. (4.2.3) correspond to the different multipolar contributions to the description of the radiation. In this way, the first-order term on the right-hand side is associated with an electric dipole, the second-order term the electric quadrupole and/or magnetic dipole and so on. These individual contributions will in turn correlate with the associated transition moment describing the transition between two atomic or molecular states, however this is not sustained over all distances [83]. Typically, and as has already be shown in this thesis, the specific nature of an electric field is investigated by consideration of the source of the multipolar radiation, i.e. dipole radiation from a dipole, and so on. However, from the sole perspective of the radiation itself, it is only through the series expansion given in Eq. (4.2.3) that its multipolar nature can be examined.

Another basis for describing this electric field component for a plane wave is in terms of vector spherical harmonics (VSHs, $\boldsymbol{Y}_{J,l,M}(\theta,\phi)$) and Bessel functions (BFs, $j_l(kr)$). This surmounts to expanding the plane wave in terms of a set of spherical waves. Thus, even though the mode expansion for quantised electromagnetic radiation, and any description of the electric field in general that stems from it, remains based on the set of plane wave solutions to the wave equation, the theory outlined below using VSHs will, from henceforth, be referred to as the spherical wave (SW) approach. It starts with the expansion of the exponential term in terms of scalar spherical harmonics (SSHs). While once again disregarding time-dependence and combining with the polarisation vector for the direction of the electric field, the exponential function in Eq. (4.2.2) is expanded as

$$\boldsymbol{e}_{1n}e^{i\boldsymbol{k}\cdot\boldsymbol{r}} = 4\pi\sum_{l=0}^{\infty}\sum_{m=-l}^{+l} i^l j_l(kr)Y^*_{l,m}(\theta',\phi')Y_{l,m}(\theta,\phi)\boldsymbol{e}_{1n}, \tag{4.2.5}$$

where $Y_{l,m}(\theta,\phi)$ and $Y^*_{l,m}(\theta',\phi')$ are normalised SSHs for two sets of angular coordinates (more on that to follow) with $Y^*_{l,m}(\theta',\phi')$ being the complex conjugate. $Y_{l,m}(\theta,\phi)\boldsymbol{e}_{1n}$ can subsequently be expressed in terms of VSHs, for which one must consider the coupling of angular momenta. Considering the product of two states,

$|j_1 m_1\rangle$ and $|j_2 m_2\rangle$, of generalised angular momentum operator $\boldsymbol{J}$, with quantum numbers j and $m = j, j-1, \ldots, -j$, where

$$|j_1 j_2 m_1 m_2\rangle \equiv |j_1 m_1\rangle \, |j_2 m_2\rangle \,, \tag{4.2.6}$$

a linear combination of such states can be constructed to give

$$|JM\rangle = \sum_{m_1} \sum_{m_2} \langle j_1 j_2 m_1 m_2 \,|\, JM\rangle \, |j_1 j_2 m_1 m_2\rangle \,. \tag{4.2.7}$$

Conversely, $|j_1 j_2 m_1 m_2\rangle$ may be expressed in terms of $|JM\rangle$, a relationship required for our present purposes,

$$|j_1 j_2 m_1 m_2\rangle = \sum_{J} \sum_{M} \langle j_1 j_2 m_1 m_2 \,|\, JM\rangle \, |JM\rangle \,. \tag{4.2.8}$$

While $|j_1 j_2 m_1 m_2\rangle$ is not an eigenfunction of J^2, $|JM\rangle$ is. $\langle j_1 j_2 m_1 m_2 \,|\, JM\rangle$ are Clebsch–Gordan coefficients which arise from the combination of two angular momenta, with J representing the new total angular momentum. Typically $|j_1 j_2 m_1 m_2\rangle$ is referred to as an eigenfunction in the uncoupled representation, while $|JM\rangle$, which may also be represented as $|j_1 j_2 JM\rangle$, as an eigenfunction in the coupled representation. Substituting $|j_1 m_1\rangle = Y_{lm}$, $|j_2 m_2\rangle = \boldsymbol{e}_{1n}$ and $|JM\rangle = \boldsymbol{Y}_{J,l,M}$, a VSH, we find that

$$Y_{l,m}(\theta, \phi)\boldsymbol{e}_{1n} = \sum_{J} \sum_{M} \langle l1mn \,|\, JM\rangle \, \boldsymbol{Y}_{J,l,M}(\theta, \phi), \tag{4.2.9}$$

with the Clebsch–Gordan coefficients coupling the states with $j_1 = l$, $m_1 = m$, and $j_2 = 1$, $m_2 = n$, and are now represented by $\langle l1mn \,|\, JM\rangle$. As one can now see, this is where the labelling of the polarisation vector as $\boldsymbol{e}_{1n}$ becomes useful. The angular momentum of l associated with the SSH couples with the angular momentum of 1 associated with the polarisation vector field to give a total angular momentum of J. As will be described later, M is then related to both J and m and n. It is noted that, for each appearance of the Clebsch–Gordan coefficients in the equations presented here, a Wigner 3j symbol could also be used as an alternative [103, 105]. Applying Eq. (4.2.9) to Eq. (4.2.5) yields

$$\boldsymbol{e}_{1n}e^{i\boldsymbol{k}\cdot\boldsymbol{r}} = 4\pi\sum_{l}\sum_{m}\sum_{J}\sum_{M} i^l j_l(kr) Y^*_{l,m}(\theta',\phi') \left\langle l1mn \,|\, JM \right\rangle \boldsymbol{Y}_{J,l,M}(\theta,\phi). \tag{4.2.10}$$

Alternatively, this can be written as

$$\boldsymbol{e}_{1n}e^{i\boldsymbol{k}\cdot\boldsymbol{r}} = 4\pi\sum_{l}\sum_{m}\sum_{J}\sum_{M} i^l j_l(kr) \left| l, m(\theta',\phi') \right\rangle \left\langle l1mn \,|\, JM \right\rangle \left| J, l, M(\theta,\phi) \right\rangle. \tag{4.2.11}$$

These two equations are identical with the normalised scalar spherical harmonic, $Y^*_{l,m}(\theta',\phi')$, represented by $\left| l, m(\theta',\phi') \right\rangle$ in Eq. (4.2.11). Meanwhile, $\left| J, l, M(\theta,\phi) \right\rangle \equiv \boldsymbol{Y}_{J,l,M}(\theta,\phi)$ represents a vector spherical harmonic, an angular component, while $j_l(kr)$ is a spherical Bessel function, a radial component. Both of these representations of the electric field associated with a particular plane wave propagating in a general direction defined by the polar angles θ' and ϕ' are seen in the literature and have been given here to avoid any confusion. A key characteristic of this SW approach to representing electromagnetic radiation is the use of spherical polar coordinates, r, θ and ϕ. It is noted that in both equations, two sets of coordinates are employed. While θ' and ϕ' are the angular coordinates associated with the direction of the wave vector for a plane wave, θ and ϕ are the angular coordinates for the point of observation [106]. For example, if the direction of propagation is along the z-axis, $\theta' = 0$ and Eq. (4.2.10) becomes,

$$\boldsymbol{e}_{1n}e^{ikz} = \sum_{J}\sum_{l} i^l \sqrt{4\pi(2l+1)} j_l(kr) \left\langle l10n \,|\, Jn \right\rangle \boldsymbol{Y}_{J,l,n}(\theta,\phi), \tag{4.2.12}$$

with the angles θ and ϕ still to be chosen. The appearance of these coordinates in these equations, a feature that is utilised in the work presented in this chapter, is in contrast to the Cartesian coordinate system typically employed in the plane wave description. There will be more on the spherical polar coordinate system later in this section.

Before going any further, it is prudent at this stage to make note of the different letters invoked in Eqs. (4.2.10) and (4.2.11). The VSH, $\boldsymbol{Y}_{J,l,M}(\theta,\phi)$, an angular function, as it is employed in these equations, determines the angular momentum of the photon associated with the propagating radiation [102]. The indices J, l, and M that identify a particular VSH, are quantum numbers that characterise the state of the photon of the emitted/absorbed radiation [102]. This is a key detail that is important to remember, especially when one comes to consider the precise nature of the emitting/absorbing species (i.e. the orbitals involved in the atomic transition). J and M are simply the quantum numbers for the total angular momentum (of the photon) and the magnetic quantum number associated with J, the latter representing the projection of the angular momentum onto a specified axis (the polar axis, conventionally labelled the z-axis). $M = m + n$ and it has allowed values of $-J \leq M \leq J$ [106]. Although easy to think of as a quantum number since it takes on integer values, l is simply a number that is used to select the appropriate vector and scalar spherical harmonics for a particular photon state. While one would be forgiven for identifying l as the orbital angular momentum quantum number commonly associated with the atomic states and particular orbitals, it should be stressed that this is not the case within the context of these equations. This is apparent through examination of Sections 9 and 10 in Ref. [102]. m is the magnetic quantum number associated with the quantum number, l, and is employed in these equations for the selection of the required scalar spherical harmonics, such that l refers to the degree of the spherical harmonic, and m the order. m can take values in the range $-l \leq m \leq l$. n, as has already been mentioned, reflects the polarisation of the electric field. This takes on the form of a set of quantum numbers and is discussed in more detail later within the context of the calculation of the VSHs.

Getting back to the description of electromagnetic radiation, as is well established, the angular momentum involved in a transition is intrinsically connected to the multipolar character of the field or potential under consideration. This means that now, rather than being encapsulated and hidden in one term, the multipolar contributions to the description of the radiation, from the perspective of the radiation itself, are straightforwardly identified explicitly through the quantum numbers, mainly the total angular momentum, J, in Eqs. (4.2.10) and (4.2.11). Importantly, this information can easily be propagated through to the equations of practical use with a clear spotlight cast on the angular momentum properties of the photon involved. This is the key facet of the

SW approach that offers an alternative way of exploring the nature of the electric field as will be shown in this work. While remembering that these quantum numbers are associated with the photon, we note that $J = 1$ corresponds to the dipolar description of the field, both electric and magnetic. $J = 2$ corresponds to the quadrupolar description and so on, with the electric quadrupole being the highest order term under consideration in this work. Obviously, the angular momentum associated with the photon has to correspond to that involved in the transition that spawns it since the total angular momentum of the system has to be conserved. When it comes to correlating the photon state with the angular momentum associated with a particular atomic multipolar transition, one has to be slightly careful when considering the different quantum numbers involved. The quantum numbers labelling a particular photon state in this work are determined through consideration of the selection rules (both in terms of the quantum numbers and the parity) associated with a particular transition [102, 104]. Consider, for example, the $2p_0 \to 1s$ downward multipole transition of the hydrogen atom. The quantum numbers for the transition from the perspective of the atom are the (orbital) angular momentum quantum number, $l = 1$, since we are moving from a p to an s orbital, indicating a dipole transition, and the magnetic quantum number associated with l which is $m_l = 0$, as the transition involves the p_0 orbital. From the perspective of the photon, this means that the total angular momentum, $J = 1$. When it comes to M, we have already established that, from a purely quantum numbers perspective, M is thought of in terms of J with $-J \leq M \leq J$. This is important when establishing all of the possible VSHs that may be required for any calculation of the electric and magnetic fields of electromagnetic radiation, as will be discussed below. When it comes to the identification of a particular photon state, and the connection with the preceding atomic transition, however, the specific value of M required must be equal to the difference between the m_l values of the initial and final states at the source. This is most easily seen through Sections 9 and 10 of Ref. [102] where Grinter states '...it is useful at this point to remind ourselves that the angular parts of the initial and final states of the atom are [the SSHs] Y_{AC} and Y_{GH} respectively, while the interacting photon is characterised by the VSH $\boldsymbol{Y}_{J,l,M}$'. Comparing with the standard notation of SSHs, $Y_{l,m}$, we see C and H are the m_l values of the initial and final states, respectively of the atomic transition. Grinter proceeds to declare one selection rule for stimulated transition as being $M = H - C$. As such, for the example of the $2p_0 \to 1s$ transition currently under consideration, the value of M for that particular photon, is simply $M = 0 - 0 = 0$ since $m_l = 0$ for an s orbital and $m_l = 0$ for the p_0 orbital. Naturally, the values of M will still adhere to the possible values as dictated by J. Thus, to summarise, while M takes on multiple values according to J in order to define all the possible VSHs (see below), in the application to a particular photon state, only one value of M is involved [105]. l in Eqs. (4.2.10) and (4.2.11), as it relates to the photon, is not the same l that is associated with the atomic transition and takes on multiple values, the selection of which influencing the type of field being described. This is clarified further later on. Although not particularly demanding, with this example one can appreciate the attentiveness required when identifying and correlating the quantum numbers of the photon state with the more common interpretation of quantum numbers in terms of atomic states. Nevertheless, once employed, not only is the precise multipolar nature of the radiation readily established, but equally the connection and role of angular momentum and its exchange between light and electronic motion is simultaneously highlighted and preserved throughout the field equations presented thereafter.

Looking at the formulation of Eqs. (4.2.10) and (4.2.11), it is clear to see that central to the description are the VSHs and thus a way of calculating them is required. The construction of the VSHs and the transformation properties of a vector field are characterised by an angular momentum operator, $\boldsymbol{J}$ arising from the coupling of two angular momenta, specifically the orbital angular momentum operator, $\boldsymbol{L}$, and spin angular momentum operator, $\boldsymbol{S}$, of the field [106]. The eigenfunctions of L^2 are the scalar spherical harmonics, $Y_{l,m}$ [106]. The eigenfunctions of S^2 are $|SM_S\rangle$ and while the spin of a scalar field is 0, a vector field has unit spin, such that $S = 1$ and $M_S = 1, 0, -1$ [106]. As has already been mentioned via Eq. (4.2.7), eigenfunctions of J^2 can be formed by following the general rules for the coupling of angular momentum eigenfunctions [106]. In this way, a direct way of constructing the VSHs from the SSHs can be formed, although their calculation may be found in many texts [102, 106].

Applying the substitutions

$$|j_1 m_1\rangle = Y_{l,m}(\theta, \phi) \tag{4.2.13}$$

and

$$|j_2 m_2\rangle = |S M_S\rangle = \boldsymbol{e}_{1n} \tag{4.2.14}$$

and knowing $|JM\rangle \equiv \boldsymbol{Y}_{J,l,M}$, using Eq. (4.2.7) we find that

$$\boldsymbol{Y}_{J,l,M}(\theta, \phi) = \sum_{m=-l}^{+l} \sum_{n=-1}^{+1} \langle l1mn \,|\, JM\rangle \, Y_{l,m}(\theta, \phi) \boldsymbol{e}_{1n}. \tag{4.2.15}$$

Comparing this to Eq. (4.2.9), we see that (4.2.15) is simply the opposite relationship, providing the eigenfunction in the coupled representation in terms of the eigenfunctions in the uncoupled representation. A select number of VSHs can be found in Table 1 of Ref. [102] calculated using the same equation.

The calculation in Eq. (4.2.15) involves coupling the angular momenta of one or more SSH, depending on the value of l, with that of the vectors, $\boldsymbol{e}_{1n}$, leading to a state with angular momenta defined by J and M. As before, $\langle l1mn \,|\, JM\rangle$ are the Clebsch–Gordan coefficients associated with such coupling. Previously, in the context of the electric field of plane wave radiation (Eq. (4.2.10)), $\boldsymbol{e}_{1n}$ was identified as the polarisation vector. The VSHs can be interpreted by taking on the significance of an electric field, as Weissbluth points out on Pg. 189 of Ref. [106], in which case $\boldsymbol{e}_{1n}$ is still considered the polarisation vector. However, it is perhaps simpler, within the context of just calculating the VSHs, to consider $\boldsymbol{e}_{1n}$ as merely the directional components of the VSH, that form a set of unit field vectors, pointing along three coordinate axes in a spherical basis. That is $\boldsymbol{e}_{1+1}$, $\boldsymbol{e}_{10}$ and $\boldsymbol{e}_{1-1}$ [106]. The reason for this is that, in order to describe the electric field of a plane wave (Eq. (4.2.10)), or as we shall see, an electric field in general, the full set of VSHs are required beforehand. This means that multiple instances of n occur when considering Eqs. (4.2.10) and Eq. (4.2.15). The unit vectors in the spherical basis can be expressed in terms of the Cartesian coordinate unit vectors and vice versa through Eqs.

(4.2.16) and (4.2.17), respectively,

$$\boldsymbol{e}_{1-1} = \frac{1}{\sqrt{2}}(\boldsymbol{e}_{1x} - i\boldsymbol{e}_{1y}) \tag{4.2.16a}$$

$$\boldsymbol{e}_{10} = \boldsymbol{e}_{1z} \tag{4.2.16b}$$

$$\boldsymbol{e}_{1+1} = -\frac{1}{\sqrt{2}}(\boldsymbol{e}_{1x} + i\boldsymbol{e}_{1y}) \tag{4.2.16c}$$

$$\boldsymbol{e}_{1x} = -\frac{1}{\sqrt{2}}(\boldsymbol{e}_{1+1} - \boldsymbol{e}_{1-1}) \tag{4.2.17a}$$

$$\boldsymbol{e}_{1y} = \frac{i}{\sqrt{2}}(\boldsymbol{e}_{1+1} + \boldsymbol{e}_{1-1}) \tag{4.2.17b}$$

$$\boldsymbol{e}_{1z} = \boldsymbol{e}_{10}. \tag{4.2.17c}$$

Computationally, it is useful to consider $\boldsymbol{e}_{1n}$ in this way, simply as a set of three vectors to be summed. Nevertheless, it is still worthwhile putting their appearance into context. As we have discussed, the VSHs serve as a general description of the angular characteristics of electromagnetic radiation (not just the electric field as in the example described by Weissbluth [106]), identifying the state of the photon. As such, the unit vectors $\boldsymbol{e}_{1n}$ employed in Eq. (4.2.15) can be seen to signify the directional components of that radiation/photon, with the usual convention that the directional properties refer to the electric field component. Great care has been taken over this interpretation in order to avoid confusion with the polarisation vector associated with the plane wave. Thus far $\boldsymbol{e}_{1n}$, with components n, correspond to laboratory-based vectors with their exact direction to be determined by the precise experimental set-up [102, 103]. As already mentioned, n takes the form of a quasi quantum number and the three unit vectors involved are $\boldsymbol{e}_{1+1}$, $\boldsymbol{e}_{10}$ and $\boldsymbol{e}_{1-1}$.

With the VSH being calculated characterising a particular photon state, in an effort to be consistent throughout the formulation of the equations of this spherical wave approach, it is useful to substitute the laboratory-based unit spherical vectors and instead consider photon-based unit vectors [103]. While still denoting the directional properties of the electric field component (polarisation) of the radiation/photon, their directionality is instead directly correlated with the direction of propagation of the electromagnetic radiation. $\boldsymbol{\Theta}$, $\boldsymbol{\Phi}$ and $\boldsymbol{R}$ are those unit vectors [103]. Employing a spherical polar coordinate system (r, θ, ϕ) with the source of the radiation (an electric or magnetic multipole) situated at the centre, $\boldsymbol{\Theta}$, $\boldsymbol{\Phi}$ and $\boldsymbol{R}$ are orthogonal unit vectors, forming a right-handed coordinate system such that $\boldsymbol{\Theta} \times \boldsymbol{\Phi} = \boldsymbol{R}$ [103]. $\boldsymbol{R}$, the radial unit vector, is directed along the direction of propagation, $\boldsymbol{\Theta}$ is a unit vector in the direction of increasing θ, and $\boldsymbol{\Phi}$ is a unit vector in the direction of increasing ϕ. It should be noted that the spherical polar coordinate system being utilised throughout this formulation follows the ISO convention typically used in physics, such that r gives the radial distance of a point from the origin, θ is the polar angle, that is the angle made with respect to the positive polar axis, which in this case is of the laboratory-based coordinate system and is labelled 0 and ϕ is the azimuthal angle situated in the plane of the remaining directions of the laboratory-based coordinate system, labelled ± 1. Using these photon-based unit vectors, the VSHs can be separated into their three orthogonal components $\Theta_{J,l,M}$, $\Phi_{J,l,M}$ and $R_{J,l,M}$ directed along $\boldsymbol{\Theta}$, Φ and $\boldsymbol{R}$ respectively, such that [103]

$$\boldsymbol{Y}_{J,l,M} = \Theta_{J,l,M}\boldsymbol{\Theta} + \Phi_{J,l,M}\boldsymbol{\Phi} + R_{J,l,M}\boldsymbol{R}. \tag{4.2.18}$$

The relationships of these photon-based vectors with the laboratory-based unit vectors employed in Eq. (4.2.15) are shown in Eqs. (4.2.19a)–(4.2.19c) and apply specifically to an out-going wave/photon [103],

$$\boldsymbol{e}_{1-1} = e^{-i\phi}(\cos\theta\boldsymbol{\Theta} - i\boldsymbol{\Phi} + \sin\phi\boldsymbol{R})/\sqrt{2} \tag{4.2.19a}$$

$$\boldsymbol{e}_{10} = -\sin\theta\boldsymbol{\Theta} + \cos\theta\boldsymbol{R} \tag{4.2.19b}$$

$$\boldsymbol{e}_{1+1} = e^{i\phi}(-\cos\theta\boldsymbol{\Theta} - i\boldsymbol{\Phi} - \sin\theta\boldsymbol{R})/\sqrt{2}. \tag{4.2.19c}$$

Performing the substitution of Eqs. (4.2.19) into Eq. (4.2.15) thus yields the VSHs needed for the description of electromagnetic radiation in terms of coordinates solely dependent on the location of the photon with respect to a source centred at the point of origin of the light. As noted in Ref. [102], the phase of the SSHs and unit vectors used in (4.2.15) is that of Condon and Shortley and it is assumed that the SSHs and unit vectors themselves form respective orthonormal sets.

As evidenced by the quantum numbers, namely J, it is the VSHs (the angular component) that reveal and account for the angular momentum associated with a particular photon. Following the laws of addition of angular momentum in quantum mechanics, J can only take on the values $|l-1| \leq J \leq l+1$ for $l \neq 0$. That is, the total angular momentum quantum number of the resultant state from the coupling of the scalar spherical harmonics, $Y_{l,m}$, with angular momentum l and the unit spherical vectors, $\boldsymbol{e}_{1n}$ with angular momentum 1, is limited to the values $J = |l \pm 1|$ and $J = l$. While this leads to the temptation of interpreting the 1 as the spin polarisation of the photon and subsequently the l as the orbital angular momentum of the light being described through these equations, this is not the case. In fact, the separation of the angular momentum associated with the radiation is not possible within these equations [85]. As previously stated, l, is simply an integer number associated with a particular SSH and selection of appropriate VSHs. Armed with the information on the possible values of J we see that from any one SSH, $Y_{l,m}$, one can only obtain three VSHs, $\boldsymbol{Y}_{l+1,l,M}$, $\boldsymbol{Y}_{l,l,M}$ and $\boldsymbol{Y}_{l-1,l,M}$. Alternatively, it is more common in practice to label these particular VSHs as $\boldsymbol{Y}_{J,J-1,M}$, $\boldsymbol{Y}_{J,J,M}$ and $\boldsymbol{Y}_{J,J+1,M}$, respectively [102, 105]. For the case when $l = 0$, the only VSH is $\boldsymbol{Y}_{1,0,M}$ ($M = 0, \pm 1$), again in accordance with laws of addition of angular momentum in quantum mechanics and when $J = 0$, the only VSH is $\boldsymbol{Y}_{0,1,0}$ since $-J \leq M \leq J$.

Finally, in order to be able to calculate the VSHs via Eq, (4.2.15) one requires the Clebsch–Gordan coefficients. Although it would appear a significant number of Clebsch–Gordan coefficients are required for the calculations considering their dependence on n (three values) and m which in turn depends on l, the total amount is restricted by the fact that, from the law of conservation of the sum of angular momentum projections, $\langle l1mn \,|\, JM \rangle = 0$ unless $m + n = M$ [102, 107]. This strict limitation means that only nine possibilities, each as a function of J and M, are required for the restricted set of VSHs required based on the laws of addition of angular momentum in quantum mechanics, and these are given in Table 4.2.1. This may also be found in Ref. [102].

	$l = J - 1$	$l = J$	$l = J + 1$
$n = -1$	$\left[\frac{(J-M)(J-M-1)}{2J(2J-1)}\right]^{1/2}$	$\left[\frac{(J-M)(J+M+1)}{2J(J+1)}\right]^{1/2}$	$\left[\frac{(J+M+2)(J+M+1)}{2(J+1)(2J+3)}\right]^{1/2}$
$n = 0$	$\left[\frac{(J-M)(J+M)}{J(2J-1)}\right]^{1/2}$	$M\left[\frac{1}{J(J+1)}\right]^{1/2}$	$-\left[\frac{(J+M+1)(J-M+1)}{(J+1)(2J+3)}\right]^{1/2}$
$n = +1$	$\left[\frac{(J+M)(J+M-1)}{2J(2J-1)}\right]^{1/2}$	$-\left[\frac{(J+M)(J-M+1)}{2J(J+1)}\right]^{1/2}$	$\left[\frac{(J-M+2)(J-M+1)}{2(J+1)(2J+3)}\right]^{1/2}$

Table 4.2.1: The Clebsch–Gordan coefficients, $\langle l1mn \mid JM\rangle$, required for use in Eq. (4.2.15) for the coupling of the angular momentum of the scalar spherical harmonics, $Y_{l,m}$ and unit vectors $\boldsymbol{e}_{1n}$, yielding the vector spherical harmonics $\boldsymbol{Y}_{J,l,M}$ for the allowed values of $l = J, J \pm 1$.

In the semi-classical treatment of radiation fields, fields emitted by electric and magnetic multipoles are termed multipole fields [85]. Traditionally, two types of multipole field are identified. In transverse electric (TE) fields the electric field has a vanishing radial component, while in transverse magnetic (TM) fields it is the magnetic field that has a vanishing radial component [85]. When the multipole field is emitted by a magnetic multipole source at the origin it is a TE field [85]. Now, throughout this thesis we have concerned ourselves with molecular or atomic chromophores and this will continue in this chapter. In doing so, any radiation to be considered originates from a fluctuation of electric-charge density and corresponds to a TM field, i.e. it is an electric multipole at the origin [85, 103]. As pointed out by Grinter, others, including Jackson, use the more informative term, electric multipole radiation for such an emitted field [103, 108]. The differentiation of the type of field involved is able to be extended even further by consideration of the VSHs required for the description of the radiation [1]. This distinction determines whether it is the electric field or magnetic field that is being scrutinised. So, for the electric multipole radiation we are most interested in, the VSH $\boldsymbol{Y}_{J,J,M}$ in which $l = J$ describes the emitted magnetic field, $\boldsymbol{B}$ according to Eq. (4.2.20), while the sum of the VSHs $\boldsymbol{Y}_{J,J+1,M}$ and $\boldsymbol{Y}_{J,J-1,M}$ of the form shown in Eq. (4.2.21) yields the electric field [102, 103],

$$\boldsymbol{B} = A_J^B h_J^{(1)}(kr)\boldsymbol{Y}_{J,J,M}(\theta, \phi) \tag{4.2.20}$$

$$\Xi_{J,J\pm1,M} = \sqrt{\frac{J}{2J+1}}\boldsymbol{Y}_{J,J+1,M} + \sqrt{\frac{J+1}{2J+1}}\boldsymbol{Y}_{J,J-1,M}. \tag{4.2.21}$$

A_J^B is simply an amplitude factor that depends on the source and $h_J^{(1)}(kr)$ is a spherical

Hankel function of the first kind. Although it is only electric multipole radiation that is considered in this work, it is noted in passing that the use of the VSH $\boldsymbol{Y}_{J,J,M}$ in which $l = J$ also represents the electric field of magnetic multipole radiation, that is radiation emitted from a magnetic multipole at the source, while the sum of the VSHs $\boldsymbol{Y}_{J,J+1,M}$ and $\boldsymbol{Y}_{J,J-1,M}$, of the same form as Eq. (4.2.21), represents the magnetic field of magnetic multipole radiation [102].

Up until Eq. (4.2.20), the radial component being employed thus far has always been a spherical Bessel function, $j_l(kr)$, a Bessel function of the first kind and of half-integer order [1]. For a source-free field, this is the correct description, determining the phase and polarisation of the field at the surface of a small sphere around the origin, at which the field vanishes [85]. However, as they represent standing waves, these functions are not suitable for the development of the equations presented in this section and we require a representation of travelling waves [102]. For this, the Bessel functions of the first kind can be combined with Bessel functions of the second kind (sometimes referred to as Neumann functions), n_l, to give Bessel functions of the third kind, otherwise known as spherical Hankel functions, $h_l^{(1)}$ and $h_l^{(2)}$ given in (4.2.22) [1],

$$h_l^{(1)} = j_l + in_l \tag{4.2.22a}$$

$$h_l^{(2)} = j_l - in_l. \tag{4.2.22b}$$

As denoted by the superscripts, $h_l^{(1)}$ is a spherical Hankel function of the first kind and $h_l^{(2)}$ is a spherical Hankel function of the second kind. We have already encountered spherical Hankel functions of the first kind in this thesis, in Chapter 2, but only from the perspective of simplifying the equations for the electromagnetic coupling tensors. Their physical significance was not considered. In combination with the time-dependence factor encountered in Eq. (4.2.2) of the form $e^{-i\omega t}$, $h_l^{(1)}$ describes an out-going wave, while the combination with $h_l^{(2)}$ describes an in-coming wave [1, 105]. For the opposite sign in the time-dependence factor, these descriptions are reversed [1, 105]. As we are solely concerned with the nature of emitted radiation in this work, we need only consider spherical Hankel functions of the first-kind, i.e. out-going waves, in the remaining analysis. Highlighted in the the work of Grinter in Ref. [103], incorporating these Hankel functions into Eq. (4.2.21) through a semi-classical treatment yields the equation for the electric field of electric multipole radiation, Eq. (4.2.23),

$$\begin{aligned}\boldsymbol{E} =& A_J^E e^{iM\phi}\frac{1}{\sqrt{2J+1}}\Big\{\sqrt{J+1}h_{J-1}^{(1)}(kr)\boldsymbol{Y}_{J,J-1,M}(\theta,\phi)\\ &-\sqrt{J}h_{J+1}^{(1)}(kr)\boldsymbol{Y}_{J,J+1,M}(\theta,\phi)\Big\},\end{aligned} \tag{4.2.23}$$

where A_J^E is an amplitude factor that depends on the source. Therefore, by merely considering the quantum numbers associated with a source transition and their connection to the parameters J, l and M of the radiation, one can immediately calculate and visualise the electric field, and in doing so easily identify the angular momentum involved, and its exchange between the electronic motion and the light.

If we compare Eq. (4.2.23) with Eq. (3.2.9) in Chapter 3, we see that Eq. (3.2.9), derived from the conventional plane wave description, offers a very generalised approach to modelling the electric field, requiring only the specific nature of the multipolar source as input. On the other hand, Eq. (4.2.23), derived from the SW approach, necessitates a much more informed identification of the nature of the source, via the quantum numbers. This means that the results from this SW approach, although lacking the generality of the conventional plane wave description, provide a prime basis for exploring radiation from atomic transitions and offers more of an insight into the form of emitted radiation. Offering a natural way to consider structured light and angular momentum, it is this form of the electric field and its phase that are to be examined in this chapter.

There is also another advantage to the SW approach compared to the conventional plane wave description. Recalling Eq. (4.2.18) and substituting it into Eq. (4.2.23) gives Eq. (4.2.24),

$$\begin{aligned}\boldsymbol{E} =& A_J^E e^{iM\phi}\frac{1}{\sqrt{2J+1}}\Big\{\sqrt{J+1}h_{J-1}^{(1)}(kr)\left[\Theta_{J,J-1,M}\boldsymbol{\Theta}+\Phi_{J,J-1,M}\boldsymbol{\Phi}+R_{J,J-1,M}\boldsymbol{R}\right]\\ &-\sqrt{J}h_{J+1}^{(1)}(kr)\left[\Theta_{J,J+1,M}\boldsymbol{\Theta}+\Phi_{J,J+1,M}\boldsymbol{\Phi}+R_{J,J+1,M}\boldsymbol{R}\right]\Big\}.\end{aligned} \tag{4.2.24}$$

From this we see that the electric field may easily be decomposed into its parallel/radial component, E_R directed along $\boldsymbol{R}$, the radiation-propagation direction (not necessarily the interatomic separation vector, see Ref. [68]) and its transverse components, E_Θ and E_Φ. For comparison, $E_{||}$ is the notation used to identify the longitudinal component (with respect to the source–detector separation vector) of the electric field from the typical molecular QED formalism, while $E_\perp$ represents the transverse component (with respect to the source–detector separation vector) [72]. The relationship between $E_{||}$ and E_R as well as that between the transverse components E_Θ and E_Φ in this SW approach and $E_\perp$ depends on the orientation of the multipolar source [1]. The individual components of the electric field have not been considered in this work, so they will not be discussed further here, however it is this natural decomposition into the longitudinal and transverse field components that is an advantage of the SW approach compared to the normal plane wave description [105]. More information regarding the decomposition of the electric field can be found in Refs. [36, 68], while for more details in relation to the SW approach see Refs. [1, 103].

Once an expression is determined for the amplitude factor for an electric quadrupole transition, A_2^E, (see Ref. [103]) Eq. (4.2.23) can be seen to be analogous to Eq. (4.2.25), which was derived by Rice *et al.* and subsequently exploited for the work in the previous chapter of this thesis [72],

$$E_\alpha = \Theta_{\beta\gamma} V_{\alpha\beta\gamma}(k, \boldsymbol{R}). \tag{4.2.25}$$

$\Theta_{\beta\gamma}$ refers back to the work in Chapter 3 and is the electric quadrupole moment of the source, $\boldsymbol{R}$ in this equation is the interatomic separation vector and the summation convention over Cartesian coordinates, α, β and γ is employed.

In the complete quantum mechanical description served up by the theory of QED, field operators replace classical fields, with the transverse electric field operator given by Eq. (4.2.26) [36, 104],

$$\boldsymbol{e}^\perp(\boldsymbol{r}) = i \sum_{\boldsymbol{p},n} \left(\frac{\hbar c p}{2\epsilon_0 V}\right)^{\frac{1}{2}} \left\{\boldsymbol{e}_1^{(n)}(\boldsymbol{p}) a^{(n)}(\boldsymbol{p}) e^{i\boldsymbol{p}\cdot\boldsymbol{r}} - \boldsymbol{e}_1^{*(n)}(\boldsymbol{p}) a^{\dagger(n)}(\boldsymbol{p}) e^{-i\boldsymbol{p}\cdot\boldsymbol{r}}\right\}. \tag{4.2.26}$$

Here, $\boldsymbol{e}_1^{(n)}(\boldsymbol{p})$ is the polarisation unit vector, with $\boldsymbol{e}_1^{*(n)}$ being its complex conjugate. V is an arbitrary quantisation volume, ϵ_0 is the electric permittivity in free space and $a^{(n)}(\boldsymbol{p})$ and $a^{\dagger(n)}(\boldsymbol{p})$ are the annihilation and creation operators, respectively, for a mode ($\boldsymbol{p}$, n). The use of $\boldsymbol{p}$ and the altered formatting for the polarisation vector compared to its presence in previous equations presented in this section, have both been done in order to highlight the summation in Eq. (4.2.26) over all possible wave vectors, $\boldsymbol{p}$ and polarisations, n, of the radiation field, such that $\sum_n(\boldsymbol{e}_1^{*(n)})$ is no longer limited to the directions associated with a laboratory-based coordinate system.

It is through these operators that one arrives at Eq. (4.2.25) for the description of the electric field emanating from a quadrupolar source. The work presented in this chapter takes advantage of the practical functionality and intuitiveness offered up by considering spherical polar coordinates and uses Eq. (4.2.23) instead which has been published elsewhere from a semi-classical treatment [102, 103]. Typically in a semi-classical approach the effect of retardation is neglected, something that has to be accounted for in the QED description, manifesting itself in a changed dependence on the interatomic separation vector [1]. The distance dependency in Eq. (4.2.23) is housed within the radial Hankel functions, and since they are solutions of Maxwell's equations, they are fully retarded [1, 103, 105]. Therefore, the fields expressed by Eqs. (4.2.23) and (4.2.20) are fully retarded with Jones *et al.* providing a detailed comparison of their decomposed electric field equations resulting from Eq. (4.2.25) with the work of Rice *et al.*, showing that the SW approach and the conventional plane wave description are consistent with one another [72, 105].

Although it is a semi-classical result that is being utilised in this work, the SW approach, within the context of QED, can just as easily be applied to the field operators. As highlighted in the work of Grinter *et al.* [102, 104], this starts by recasting the exponential term in terms of the SW approach, as in Eq. (4.2.10), by employing the following transformation

$$\boldsymbol{e}_1^{(n)}(\boldsymbol{p})e^{\pm i\boldsymbol{p}\cdot\boldsymbol{r}} \rightarrow 4\pi\sum_J\sum_l\sum_M \Omega_{JlM}^{(n)\pm\Pi}(\boldsymbol{p}), \tag{4.2.27}$$

$$\Omega^{(n)\pm\Pi}_{JlM}(\boldsymbol{p}) = i^l j_l(pr) Y^*_{l,M-n}(\theta',\phi') \left\langle l1M-nn \,|\, JM \right\rangle \boldsymbol{Y}_{J,l,M}(\theta,\phi). \tag{4.2.28}$$

It is noted that Eqs. (4.2.27) and (4.2.28) have been altered from Ref. [1] to avoid some confusion over the appearances of the labels J, l and M and their summation on the opposite side. $\Omega^{\pm(n)\Pi}_{pJlM}(\boldsymbol{p})$ is simply a function describing the created or annihilated photons of the radiation field in terms of the Bessel functions, $j_l(pr)$ and VSHs, $\boldsymbol{Y}_{J,l,M}(\theta,\phi)$ for a wave propagating in the direction defined by angles θ' and ϕ'. As evidenced by the summations over J, l and M, the multipolar contributions to the radiation are now readily separated. It should be noted that all the indices associated with Ω ($\pm, n, \Pi, p, J, l$ and M) are merely labels showing the information incorporated within the function and are not identifying discrete instances of the function itself. Ω^- indicates the complex conjugate of Ω^+ and Π represents the functions' parity, which is important when it comes to determining the spectroscopic selection rules for individual transitions. For a more detailed discussion on parity and selection rules for stimulated electronic transitions see Ref. [102]. Given that $\Omega^{\pm(n)\Pi}_{pJlM}(\boldsymbol{p})$ has been formulated based on Eq. (4.2.10) which is describing a free field, it is only necessary to consider standing waves, hence the use of the spherical Bessel functions in Eq. (4.2.28), as opposed to the Hankel functions described above. Comparing Eqs. (4.2.10) and (4.2.28) we see that the m index associated with the scalar spherical harmonic, $Y_{l,m}(\theta',\phi')$ has been replaced with $M - n$. This has been brought about by the fact that, as noted earlier, $\langle l1mn \,|\, JM\rangle = 0$ unless $m + n = M$, leading to $m = M - n$. Employing this recasting of the $\boldsymbol{e}^{(n)}_1(\boldsymbol{p})e^{\pm i\boldsymbol{p}\cdot\boldsymbol{r}}$ terms leads us to a reformulation of the mode expansion of the operator for the transverse electric field, such that

$$\boldsymbol{e}^{\perp}(\theta,\phi,\boldsymbol{r}) = i\sum_{\boldsymbol{p},n}\sum_{J,l,M}\left(\frac{\hbar cp}{2\epsilon_0 V}\right)^{\frac{1}{2}}\left\{\Omega^{+(n)\Pi}_{pJlM}(\boldsymbol{p})a^{(n)}_{\Omega}(\boldsymbol{p}) - \Omega^{-(n)\Pi}_{pJlM}(\boldsymbol{p})a^{\dagger(n)}_{\Omega}(\boldsymbol{p})\right\}. \tag{4.2.29}$$

The creation and and annihilation operators, $a^{\dagger(n)}_{\Omega}(\boldsymbol{p})$ and $a^{(n)}_{\Omega}(\boldsymbol{p})$ can now be associated with a photon of a particular multipole nature based on Ω, if desired [104]. Eq. (4.2.29) neatly shows the principle behind the SW approach set forth in the work by Grinter *et al.* and analysed in detail above, whereby the plane wave mode expansions employed in the operators of QED theory (the summations over $\boldsymbol{p}$ and n) are expanded in terms of VSHs and BFs [102, 103, 105]. This presents an insightful description for the field operator, which now provides direct information about the multipolar contributions to the radiation and in turn can facilitate the exploration of light and its angular momentum.

The next step to exploring the SW approach within the context of QED would be to apply Eq. (4.2.29) to Eq. (4.2.30)

$$H_{int} = -\sum_{\xi} \Big[\boldsymbol{\mu}(\xi) \cdot \boldsymbol{e}^{\perp}(\theta, \phi, \boldsymbol{r}_{\xi}) + \boldsymbol{\Theta}(\xi) : \nabla \boldsymbol{e}^{\perp}(\theta, \phi, \boldsymbol{r}_{\xi}) \Big] , \tag{4.2.30}$$

and develop the equations in a similar fashion to the work of Rice *et al.* and Andrews *et al*, as previously discussed in Chapter 3 of this thesis, to yield an equation for the electric field that once again explicitly considers the source [68, 72]. Through the same development of theory, a SW approach to the EET process discussed in Chapter 2 could be investigated. Note that $\boldsymbol{\Theta}(\xi)$ in Eq. (4.2.30) is referring to the (transition) quadrupole moment operator for molecule ξ.

The focus of the work presented in this chapter, however, uses the semi-classical result of Eq. (4.2.23), and the spherical polar coordinate system it is built on, to explore the multipolar nature of the electric field through a visualisation of not only itself but also its phase on the surface of a sphere. In doing so, the emphasis is placed on the radiation itself and, unlike in the work of Chapter 3, the source will only be considered through the quantum numbers appearing in Eq. (4.2.23). As previously mentioned, these are determined by the correlation with the selection rules of individual transitions and, as such, only simple, hydrogenic, atomic transitions are considered. The amplitude factor, A_J^E, which depends on the source, is neglected as, since it is only a magnitude, it will not have an impact on the angular description that is being examined through this equation.

4.3 Computational Details

Using the Python programming language, a program has been developed that calculates the electric field, its phase and the magnetic field associated with radiation described by quantum numbers J and M. The data is then subsequently plotted on the surface of a sphere with a radius to be given as a multiple of kr. Initial versions of the code existed in the Jones group thanks to the work of Shalini Narayan and Dale Green. Through the research presented in this chapter, the application has been further expanded and thoroughly tested by the author of this thesis, yielding a final version of the program that has been used to generate the results set forth in the next section. It utilises the Numpy library for mathematical and array operations, the Scipy library for calculation of the SSHs and the plotting library Matplotlib [100, 109, 110]. By merely passing it three key pieces of information for different possible scenarios, this application has made it possible to investigate the suitability of the SW approach, the nature of radiation emanating from a transition dipole and a transition quadrupole and also further contemplate what it means to view the phase of the electric field and how this appears in 3D space.

The code begins by providing dictionaries of the coefficients and l and m values associated with each spherical basis unit vector, $\boldsymbol{e}_{1n}$ for the VSHs from $\boldsymbol{Y}_{0,0,0}$ to $\boldsymbol{Y}_{2,3,-1}$ inclusive according to Table 1 of Ref. [102]. Each dictionary consists of nine key:value pairs, three for each of the three unit vectors. For example, for the VSH $\boldsymbol{Y}_{1,2,0} = (\frac{1}{\sqrt{10}})(\sqrt{3}Y_{2+1} \cdot \boldsymbol{e}_{1-1} - 2Y_{20} \cdot \boldsymbol{e}_{10} + \sqrt{3}Y_{2-1} \cdot \boldsymbol{e}_{1+1})$, the dictionary contains the terms

```
'e1min1_CG': +0.5477, 'e1min1_l': +2, 'e1min1_m': +1

'e10_CG': -0.6325, 'e10_l': +2, 'e10_m': 0

'e1pl1_CG': +0.5477, 'e1pl1_l': +2, 'e1pl1_m': -1
```

whereby `'e1min1'`, `'e10'` and `'e1pl1'` represent $\boldsymbol{e}_{1-1}, \boldsymbol{e}_{10}$, and $\boldsymbol{e}_{1+1}$ respectively. The l and m variations select the appropriate SSHs and the `CG` labels simply represent the coefficients for each $\boldsymbol{e}_{1n}$ term. Rather than carry out the full calculation given by Eq. (4.2.15) each time a VSH is required, a dictionary of the aforementioned dictionaries is created such that, through appropriate labels, specific

VSHs can be selected and calculated in a quick and efficient manner as necessary for each simulation of the fields, i.e.

```
VSH = {'000': Y_000,...,'12+1': Y_12pl1, '120': Y_120,...}
```

to demonstrate just a few.

Although a computation according to Eq. (4.2.15) is no longer required within the code, a calculation of the axial components of the VSHs is still necessary based on the equations given in Table 1 of Ref. [102]. Thus following on from the VSH dictionaries is a section of code for the defining of a function that is later called for the calculation of the requested VSHs. Within this function is a lot of information relating to what is ultimately plotted in the figures in the next section of this chapter. Looking at the equations for the individual VSHs given in Table 1 of Ref. [102] or by considering Eq. (4.2.15), we see that the vector components being calculated are those of the spherical basis unit vectors $\boldsymbol{e}_{1n}$. It has already been highlighted that within the theory it is useful to consider a different set of unit vectors, a set that is photon-based and directly related to the direction of propagation/point of observation. The correlation of the two axis systems was given through Eqs. (4.2.19) with $\boldsymbol{e}_{1-1}, \boldsymbol{e}_{10}$ and $\boldsymbol{e}_{1+1}$ providing a main axis frame and $\boldsymbol{\Theta}$, $\boldsymbol{\Phi}$ and $\boldsymbol{R}$ providing a local axis system at each point on the surface of the sphere. Initially thought to be of use computationally as well, these relationships have been employed within the function for calculating the VSHs, utilising the angles θ and ϕ that define the points where we would like the calculations to be carried out. At first glance of Eqs. (4.2.19), it appears that the angles, θ and ϕ relating the two axis systems are made with respect to the $\boldsymbol{e}_{1n}$ axis suggesting that this is the axis system at the heart of any figure generated. However, by dissecting these equations it is seen that Eqs. (4.2.19) are a combination of two relationships. First is the transformation of the spherical basis unit vectors into the Cartesian basis via Eqs. (4.2.16). Second, is the transformation of the $\boldsymbol{x}, \boldsymbol{y}, \boldsymbol{z}$ axis system into the $\boldsymbol{\Theta}$, $\boldsymbol{\Phi}$ and $\boldsymbol{R}$ coordinate system using the relation

$$\begin{bmatrix} \boldsymbol{x} \\ \boldsymbol{y} \\ \boldsymbol{z} \end{bmatrix} = \begin{bmatrix} \cos\theta\cos\phi & -\sin\phi & \sin\theta\cos\phi \\ \cos\theta\sin\phi & \cos\phi & \sin\theta\sin\phi \\ -\sin\theta & 0 & \cos\theta \end{bmatrix} \begin{bmatrix} \boldsymbol{\Theta} \\ \boldsymbol{\Phi} \\ \boldsymbol{R} \end{bmatrix} \tag{4.3.1}$$

where, $\begin{bmatrix} \boldsymbol{x} \\ \boldsymbol{y} \\ \boldsymbol{z} \end{bmatrix}$ is a vector with Cartesian components and $\begin{bmatrix} \boldsymbol{\Theta} \\ \boldsymbol{\Phi} \\ \boldsymbol{R} \end{bmatrix}$ is a vector with $\boldsymbol{\Theta}, \boldsymbol{\Phi}$ and $\boldsymbol{R}$ components. Now it can be seen that the angles θ and ϕ are actually being made with respect to the Cartesian coordinate system. Thus, within the VSH function, first, the relations in Eqs. (4.2.19) are used to transform the unit vectors. Then the $\boldsymbol{e}_{1n}$ components of the VSHs are calculated in terms of $\boldsymbol{\Theta}, \boldsymbol{\Phi}$ and $\boldsymbol{R}$, and the separate $\boldsymbol{\Theta}, \boldsymbol{\Phi}, \boldsymbol{R}$ components are subsequently summed, respectively, to yield the VSHs solely in terms of $\boldsymbol{\Theta}, \boldsymbol{\Phi}$ and $\boldsymbol{R}$ employing angles that are related to the Cartesian coordinate system. This reliance on angles with respect to the Cartesian coordinate system turns out to be quite useful when it comes to plotting any results as Python, and more specifically Matplotlib [110], require plots and the corresponding data to be cast in terms of the Cartesian coordinate system. Therefore the final step within the VSH function is to transform the VSHs from being in terms of $\boldsymbol{\Theta}, \boldsymbol{\Phi}$ and $\boldsymbol{R}$ to be in terms of $\boldsymbol{x}, \boldsymbol{y}$ and $\boldsymbol{z}$ using the relation given in Eq. (4.3.1). This is an important step that ensures the frame of reference of both the equations/data and the plotting functions of Maplotlib are consistent meaning confidence can be had in the descriptions of the fields that the figures portray. From all of the transformations and relations discussed, it can consequently be understood that, although the set of unit vectors $\boldsymbol{e}_{1n}$ are pivotal to the calculation of the VSHs, the main coordinate systems at play are those shown in Fig. 4.3.1 with the x, y, z system at the centre and a $\boldsymbol{\Theta}, \boldsymbol{\Phi}, \boldsymbol{R}$ system local to each point on the sphere which are themselves defined by the coordinates θ, ϕ and r. With the $\boldsymbol{e}_{1n}$ axis system being reported as a lab-based coordinate system in previous work (see Ref. [103]), or even when simply considered as a set of spherical basis unit vectors, when it comes to interpreting the results given below, it is important to understand that the axis at the centre of the spheres is simply the Cartesian coordinate system.

The remaining sections of code proceed to build the sphere of points at which the calculations will take place, define the values of J, M and $rdist$, that is the radius of

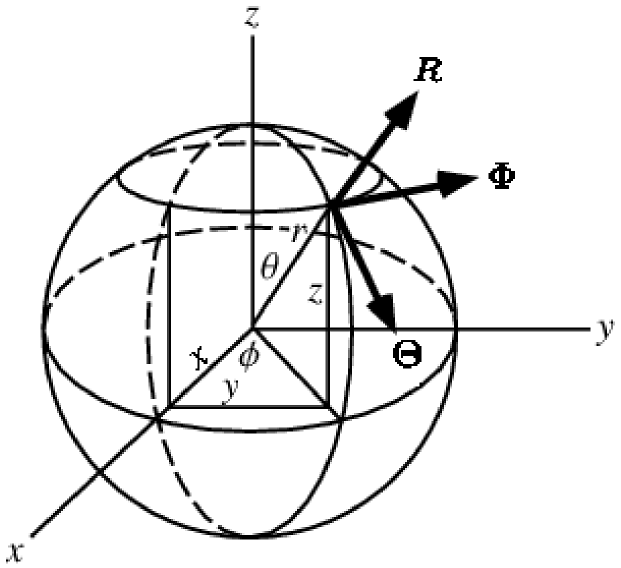

Figure 4.3.1: Schematic of the spherical coordinates, $\mathbf{\Theta}, \mathbf{\Phi}$ and $\boldsymbol{R}$ employed in this work and their connection, via angles θ and ϕ and radius r, to the Cartesian coordinate system at the heart of the sphere. Figure modified from Ref. [111].

the sphere as a multiple of kR, before the x, y and z components of the electric field are calculated from the x, y and z components of the required VSHs via Eq. (4.2.23). It is important to note that, since it is merely an amplitude factor and will not affect the angular nature of the field, the term A_J^E has been excluded from the calculation, thus no transition moment data is required. Although primarily concerned with the electric field in this research, the magnetic field can and is easily calculated using Eq. (4.2.20) for the same set of input variables J, M and $rdist$. Again, the amplitude factor, A_J^B is excluded from the calculation. One nuance to the code that should be highlighted is the fact that due to the size of the arrows plotted on the surface of the sphere, when it comes to looking at the vector fields themselves, fewer points can be calculated. As such, the arrays of θ and ϕ are no longer able to be the same size, meaning for loops have to be employed when calculations that are dependent on θ and ϕ are required. The end result is the generation of a selection of figures of the electric field, its phase and the magnetic field associated with the transition requested. Helpfully, these are all interactive figures. This, therefore allows the user to manipulate the view of the spheres in order to assess the full picture and often provides a means to create more informative and favourable images that highlight significant features. Through this interaction a more complete impression of the emitted fields can be obtained.

The phase of the electric field is also investigated using this program and this is discussed in more detail in the next section. However, it is noted here that since this examines a surface on the face of the sphere, a finer array of points may be used and the arrays of θ and ϕ are the same size.

4.4 Results and Discussion

The primary motivation behind the research presented in this section is to continue the work of the previous chapter, investigating the nature of radiation emitted from a transition quadrupole moment and its connection with structured light. It is postulated that by investigating this area of research through the implementation and thorough examination of the SW approach detailed above (and outline in Refs. [102, 103]), further insights can be gained and the applicability of this alternate approach to describing electromagnetic fields can be showcased. Although it is the quadrupole moment and the electric field that are of most interest in this work, the transition dipole moment and the magnetic field are also briefly inspected for completeness and to verify the code. As mentioned in the previous section, the program that has been written is very much an interactive one and this ability to move the sphere helps provide the viewer with some depth perception of the plot being viewed. Unfortunately, as is the nature with observing some still 2D images of a 3D object, for a few of the electric and magnetic field plots provided in this section, some of the detail is lost. At this stage, the figures presented below have been chosen to take a somewhat wider overview of the sphere in order to highlight the potential of the program itself and showcase as many features as possible.

Before proceeding to examine the fields, it is noted that in Ref. [102] it is stated ‘We shall assume throughout that the VSHs are constructed from normalised SSHs and unit vectors so that no normalisation coefficients need be specified’. The SSHs employed in this work are those within the Scipy library [109]. In an effort to ensure the code is consistent with the equations that have been presented, the orthonormality of the `scipy.special.sph_harm` functions was tested through the relation

$$\int_{\theta=0}^{\pi}\int_{\phi=0}^{2\pi} Y_{lm}Y^{*}_{l'm'}d\Omega = \delta_{ll'}\delta_{mm'}, \tag{4.4.1}$$

where $d\Omega = \sin\theta d\phi d\theta$ and the double integration equals 1 when $l = l'$ and $m = m'$ (matching SSHs) and 0 for everything else. Utilising the function `scipy.integrate.dblquad` to compute the double integral of the function

```
scp.sph_harm(1,2,phi,theta)
*np.conj(scp.sph_harm(1,2,phi,theta))*np.sin(theta),
```

where `scp` is the Scipy library [109] and `np` is the Numpy library [100], we find that the SSHs as defined through the Scipy library are indeed orthonormal.

Switching attention back to the fields, it is once again highlighted that while the electric and magnetic fields calculated in this section are done so with equations analogous to Eqs. (4.2.23) and (4.2.20), respectively, the amplitude factors (A^{E}_{J} and A^{B}_{J}) are excluded from the calculations and no transition moment data is required. We shall start with the simplest case of the fields emanating from an electric dipole transition in order to validate the code.

4.4.1 Electric Dipole Fields — $J = 1$, $M = 0$ (rdist $= 1$)

For the transition $2p_0 \rightarrow 1s$, a transition dipole moment aligned along the z-axis, we identify the quantum numbers of importance to be $J = 1$ and $M = 0$. With $l = 0, 2$ to select the $\boldsymbol{Y}_{1,0,0}$ and $\boldsymbol{Y}_{1,2,0}$ VSHs for the calculation of the electric field and $l = J = 1$ to select the $\boldsymbol{Y}_{1,1,0}$ VSH for the magnetic field, we proceed to generate images of the vector fields in a spherical distribution surrounding the transition dipole moment at a radial distance (`rdist`) where $kr = 1$. The electric field and magnetic field are shown in Fig. 4.4.1.

To ascertain if the fields are being calculated and plotted correctly, it is useful to examine and compare the results with equations provided in Ref. [103]. Considering the electric

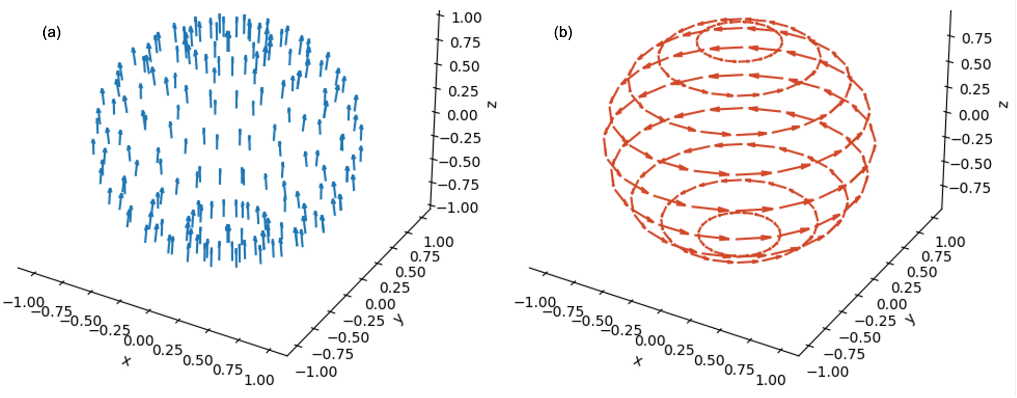

Figure 4.4.1: Plots of the (a) electric and (b) magnetic fields calculated via Eqs. (4.2.23) and (4.2.20), respectively with $J = 1$, $M = 0$ identifying a $p_0 \to s$ transition. The points on the sphere are situated at a radial distance from the centre where $kr = 1$.

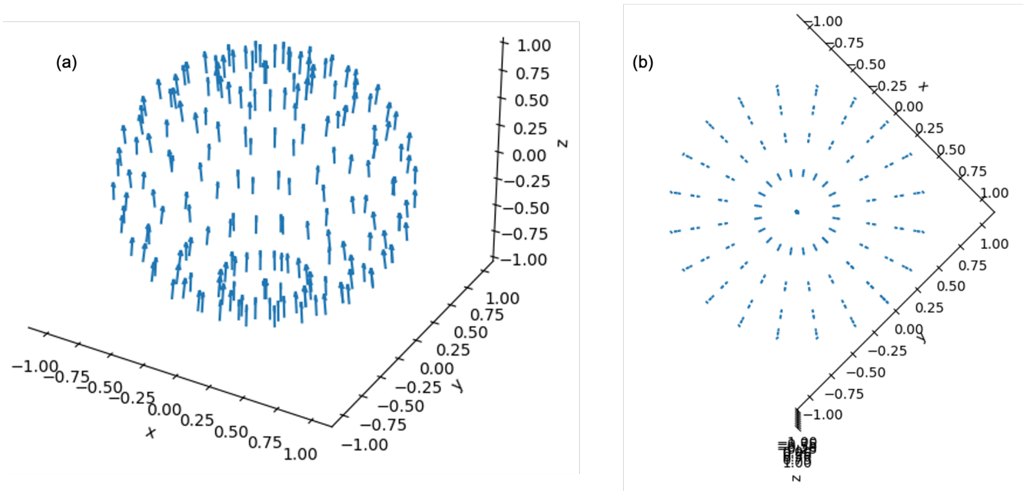

Figure 4.4.2: (a) plot of the electric field emanating from the $p_0 \to s$ transition characterised by the quantum numbers $J = 1$ and $M = 0$ at a radial distance where $kr = 1$ with (b) showing the top-down view.

field to start with, Ref. [103] tells us that for this particular transition, it will only have components in $\boldsymbol{\Theta}$ and $\boldsymbol{R}$ at any given point on the sphere. The equations for these components are given below for simplicity.

$$\boldsymbol{E_R} = A_1^E \frac{1}{\sqrt{6\pi}} \left[h_0^{(1)}(kr) + h_2^{(1)}(kr) \right] \cos\theta \boldsymbol{R}. \tag{4.4.2}$$

$$\boldsymbol{E_\Theta} = -A_1^E \frac{1}{2\sqrt{6\pi}} \left[2h_0^{(1)}(kr) - h_2^{(1)}(kr) \right] \sin\theta \boldsymbol{\Theta}. \tag{4.4.3}$$

We see that both of these equation only rely on the angle θ and we have already established, from careful examination of the unit spherical vector transformations, that θ is the polar angle made to the positive z-axis. It is also recognised that this is the same angle made with respect to the the axis at the centre of the plots as determined by the code. Let us now examine a few specific points on the surface of the sphere. First consider the north pole. Here, $\theta = 0$. Since $\cos 0 = 1$ and $\sin 0 = 0$, Eqs. (4.4.2) and (4.4.3) inform us that the electric field will only contain a radial component associated with the local spherical coordinate system at that point. Looking at the coordinate transformation relationship in Eq. (4.3.1) we can determine at this point (where $\theta = 0$ and $\phi = 0$) what the x, y and z components of the radial component will be.

$$\boldsymbol{E_x} = \sin\theta\cos\phi\boldsymbol{E_R} = \sin(0)\cos(0)\boldsymbol{E_R} = 0 \tag{4.4.4a}$$

$$\boldsymbol{E_y} = \sin\theta\sin\phi\boldsymbol{E_R} = \sin(0)\sin(0)\boldsymbol{E_R} = 0 \tag{4.4.4b}$$

$$\boldsymbol{E_z} = \cos\theta\boldsymbol{E_R} = \cos(0)\boldsymbol{E_R} = \boldsymbol{E_R}. \tag{4.4.4c}$$

Therefore, for the field emanating from a $p_0 \to s$ transition at the north pole position on the sphere the electric field vector consists of only a $\boldsymbol{z}$ component and we would expect to see an arrow pointing straight up. Inspecting Fig. 4.4.1(a) we see exactly that. At the opposite pole, where $\theta = \pi$, the electric field will once again only consist of a radial component. The $\boldsymbol{R}$-axis localised at the south pole is in the opposite direction to the axis localised to the north pole. Thus, using Eq. (4.4.2) we see $\boldsymbol{E_R}$ will be negative since $\cos\pi = -1$ indicating the vector points in the opposite direction to $\boldsymbol{R}$. Using the same relations outlined in Eq. (4.4.4) with $\theta = \pi$, $\phi = 0$ and knowing $\boldsymbol{E_R}$ is negative, we find the electric field vector again only consists of a positive $\boldsymbol{z}$ component. Therefore examination of Fig. 4.4.1(a) should show a vector pointing straight up was found at the north pole. Again, this is precisely what is shown.

Next we consider a point around the equator where $\theta = \pi/2$. Since $\cos(\pi/2) = 0$ and $\sin(\pi/2) = 1$, the electric field vector at any point around the equator will only consist of a $\boldsymbol{\Theta}$ component. Choosing the point on the sphere where $\theta = \pi/2$ and $\phi = \pi/2$, and looking at Fig. 4.3.1 for a guide, the $\boldsymbol{\Theta}$-axis localised at that point will point straight down. Since Eq. (4.4.3) includes a minus sign, we know the electric field vector will point in the opposite direction. Using the equations given in Eq. (4.4.5) we see that the electric field will once again only comprise a $\boldsymbol{z}$ component and, knowing that

$\boldsymbol{E_{\Theta}}$is already negative, the negative sign indicates that the vector points in the positive z direction.

$$\boldsymbol{E_x} = \cos\theta\cos\phi\boldsymbol{E_{\Theta}} = \cos(\frac{\pi}{2})\cos(\frac{\pi}{2})\boldsymbol{E_{\Theta}} = 0 \tag{4.4.5a}$$

$$\boldsymbol{E_y} = \cos\theta\sin\phi\boldsymbol{E_{\Theta}} = \cos(\frac{\pi}{2})\sin(\frac{\pi}{2})\boldsymbol{E_{\Theta}} = 0 \tag{4.4.5b}$$

$$\boldsymbol{E_z} = -\sin\theta\boldsymbol{E_{\Theta}} = -\sin(\frac{\pi}{2})\boldsymbol{E_{\Theta}} = -\boldsymbol{E_{\Theta}}. \tag{4.4.5c}$$

Considering the equations in Eq. (4.4.5), it is clear that at any point around the equator of the sphere (i.e. for any value of ϕ), the electric field vector will be comprised solely of a $\boldsymbol{z}$ component pointing in the positive z direction. Inspection of Fig. 4.4.1(a) shows exactly this. These few checks serve to provide some level of confidence that the code is plotting the electric field correctly.

As for the magnetic field a similar vetting process can be carried out. Via Ref. [103], for the $J = 1$, $M = 0$ transition under investigation, the magnetic field will only have a component directed along $\boldsymbol{\Phi}$ and the equation for which is given below.

$$\boldsymbol{B_{\Phi}} = A_1^B\left(\frac{i\sqrt{3}}{2\sqrt{\pi}}\right)e^{ikr}\left[\frac{1}{kr} + \frac{i}{(kr)^2}\right]\sin\theta\boldsymbol{\Phi}. \tag{4.4.6}$$

As Grinter points out, by only comprising a $\boldsymbol{\Phi}$ component, the magnetic field is orthogonal to the electric field, as required, and this can be seen in Fig. 4.4.1(b) as all of the arrows lie horizontally on the surface of the sphere, i.e. none point inwards or outwards [103]. This also reflects the fact that the magnetic field is entirely transverse with respect to the direction of observation [72]. If we consider any point on the equator where $\theta = \pi/2$, then $\sin\theta = 1$ and the magnetic field will point directly along $\boldsymbol{\Phi}$.

$$\boldsymbol{B_x} = -\sin\phi\boldsymbol{B_{\Phi}} \tag{4.4.7a}$$

$$\boldsymbol{B_y} = \cos\phi\boldsymbol{B_{\Phi}} \tag{4.4.7b}$$

$$\boldsymbol{B_z} = 0. \tag{4.4.7c}$$

Looking at the relations given in Eq. (4.4.7) to determine the $\boldsymbol{x}, \boldsymbol{y}$ and $\boldsymbol{z}$ components of the magnetic field, we see that it will never contain a $\boldsymbol{z}$ component. We therefore expect to see all the vectors of the magnetic field lying in the x, y-plane. A quick check of Fig. 4.4.1(b) confirms that this is what is observed. For $\phi = 0$, the magnetic component will only contain a $\boldsymbol{y}$ component (pointing in the same direction as $\boldsymbol{\Phi}$), while for $\phi = \pi/2$ it will only be comprised of an $\boldsymbol{x}$ component (which points in the opposite direction to $\boldsymbol{\Phi}$). This indicates the direction in which we would expect the arrows to point around the sphere, namely counterclockwise. For values of ϕ at which $\boldsymbol{\Phi}$ doesn't point directly along the x or y axis, the magnetic field will comprise a combination of $\boldsymbol{x}$ and $\boldsymbol{y}$ components meaning one expects to see the arrows curve horizontally around the face of the sphere. For the $p_0 \rightarrow s$ transition, this is how the entirely transverse nature of the magnetic field with respect to the direction of observation manifests itself. Both the directionality of the arrows and their wrapping around the surface are confirmed to be seen by looking at Fig. 4.4.1(b). Finally, Fig. 4.4.1(b) also shows that the magnetic field vectors move in closed loops, an expected result that appears as a consequence of Gauss's law for magnetism, whereby $\nabla \cdot \boldsymbol{B} = 0$. All of these results lead to a strong level of confidence that the code is plotting the magnetic field correctly.

Having garnered some confidence in the working of the code, we now proceed to survey more complex illustrations of the electric and magnetic fields.

4.4.2 Electric Dipole Fields — $\boldsymbol{J = 1}$, $\boldsymbol{M = \pm 1}$ (rdist $= 1$)

Before turning our attention to the fields emanating from an electric quadrupole, two electric dipole transitions, specifically the $p_{-1} \rightarrow s$ transition and the $p_{+1} \rightarrow s$ transition remain. The plots of the electric field associated with each one can be found in Figs. 4.4.3 and 4.4.4, respectively.

The two transitions are associated with light distinguished as left- (p_{+1}) and right- (p_{-1}) circularly polarised. Comparing Figs. 4.4.3(b) and 4.4.4(b), the top-down view of the fields emitted from the p_{-1} and p_{+1} transitions respectively, one can see distinct rotations of the vector fields about the central axis in opposite directions. For the field shown in Fig. 4.4.3 the rotation appears to be clockwise while for that in Fig. 4.4.4 it appears to be counterclockwise. In terms of the standard nomenclature, when looking in the

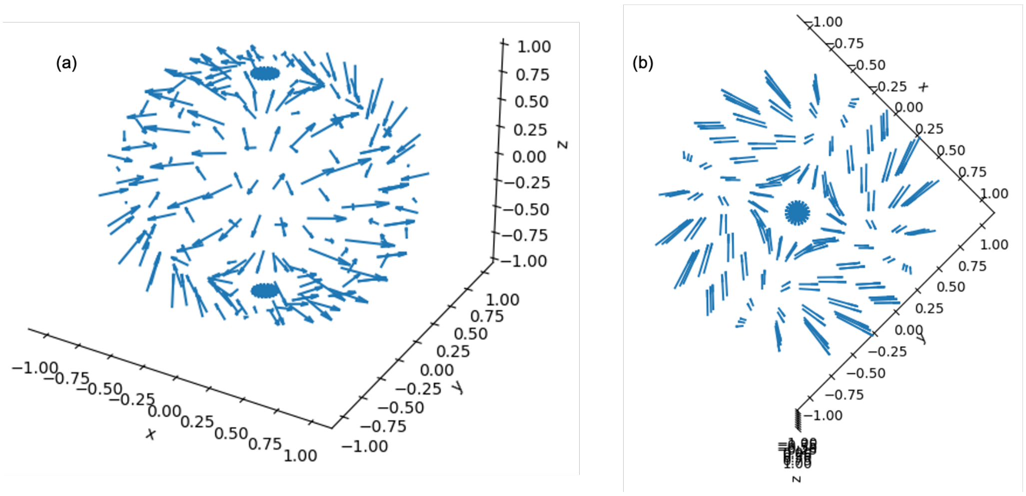

Figure 4.4.3: (a) plot of the electric field emanating from the $p_{-1} \rightarrow s$ transition characterised by the quantum numbers $J = 1$ and $M = -1$ at a radial distance where $kr = 1$ with (b) showing the top-down view.

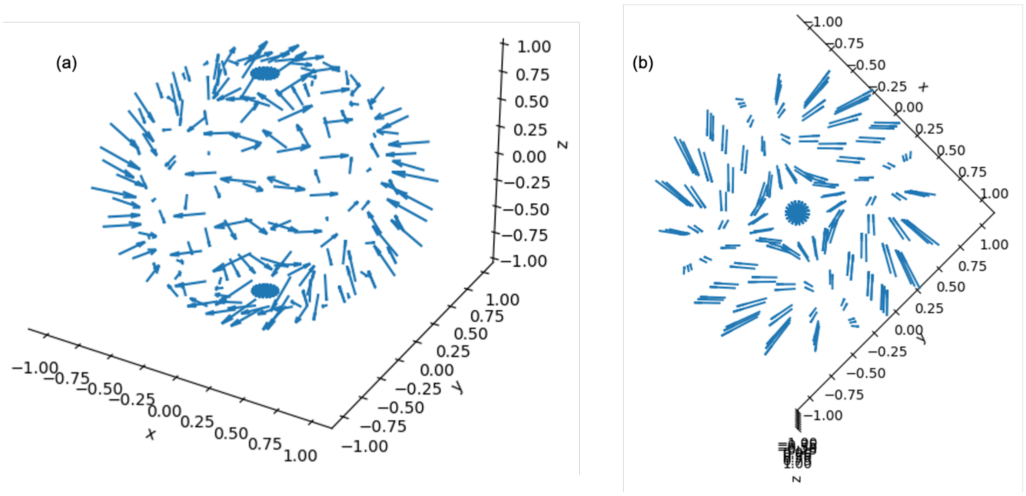

Figure 4.4.4: (a) plot of the electric field emanating from the $p_{+1} \rightarrow s$ transition characterised by the quantum numbers $J = 1$ and $M = +1$ at a radial distance where $kr = 1$ with (b) showing the top-down view.

direction of propagation, left-circularly polarised light $(+1)$ rotates counterclockwise, while right-circularly polarised light (-1) rotates clockwise. Although this relationship appears to be born out correctly in the figures that have been generated, the significance of the central axis is still yet to be fully understood.

The magnetic fields emanating from the two transitions under consideration in this section are given in Fig. 4.4.5 for completeness. They continue to display the purely transverse nature of the magnetic field with respect to the direction of observation and show the vectors exhibiting movement in closed loops. It also appears that one plot is a

90° rotation of the other a characteristic one might expect when considering the p orbitals involved. Once again, these results serve to suggest that the magnetic field is being calculated and plotted correctly.

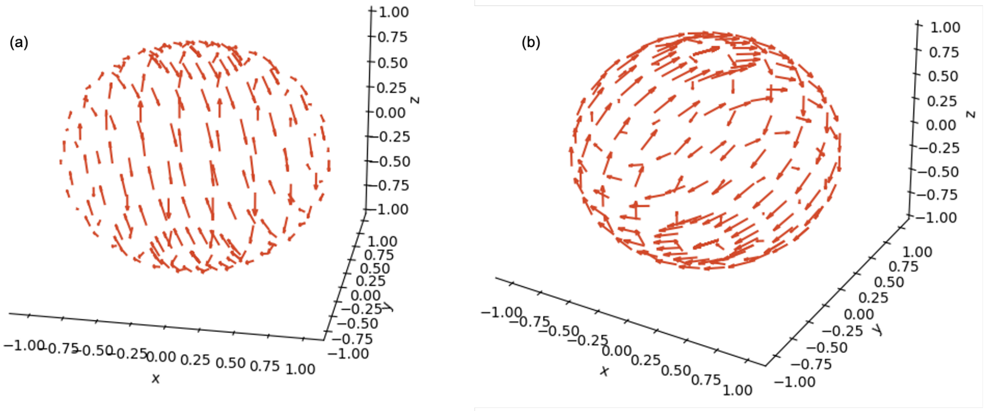

Figure 4.4.5: Plots of the magnetic fields emitted by (a) the $p_{-1} \to s$ transition ($J = 1$ and $M = -1$) and (b) the $p_{+1} \to s$ transition ($J = 1$ and $M = +1$) at a radial distance where $kr = 1$

4.4.3 Electric Quadrupole Fields — $J = 2$ (rdist $= 1.5$)

We now move on to investigate the fields that are emitted from a transition quadrupole moment situated at the heart of the spherical depictions. As discussed in the previous chapter, this involves studying the $3d \to 1s$ transitions of a hydrogen-like atom. Due to our exclusion of the amplitude factor within the equations for the electric and magnetic fields generated from the SW approach, no transition quadrupole moment data is necessary. Instead, we merely consider the quantum numbers associated with any $d \to s$ transition regardless of the energy levels that could be involved. These are $J = 2$ and $M = \pm 2, \pm 1, 0$ associated with the five d-orbitals. Knowing that $l = J - 1, J + 1$ for the electric field and $l = J$ for the magnetic field, the VSHs required for the calculations are $\boldsymbol{Y}_{2,1,M}$, $\boldsymbol{Y}_{2,3,M}$ and $\boldsymbol{Y}_{2,2,M}$. Armed with this information we proceed to plot the vector fields for a spherical distribution of points at a radial distance (`rdist`) where $kr = 1$. At this point it should be mentioned that there is a slight irregularity with the code relating to the radial distance that will require further investigation. Although a length for the arrows is set (to 1) in the plotting command, the size of the arrows changes when the `rdist` variable is changed. If one associates the length of the arrow with the strength of the field at that particular point, then generally the program works in line with the prediction that as you consider points further from the centre, the arrows will get shorter as the strength of the field decreases. When comparing the $J = 1$, $M = 0$ and $J = 2$, $M = 0$ outputs at a radial distance where $kr = 1$ the expected result also appears to hold true. However, when looking at the fields of $J = 2$, $M = +1$ at that same distance, the arrows are longer than those in the depictions of the $J = 1$, $M = +1$ fields and this is not understood. Nevertheless, at this stage it is not an immediate concern as we are far more interested in the angular nature of the fields as opposed to the radial nature, which is solely described through the built-in Hankel functions of the Scipy library [109]. With that said, we start our exploration of the electric field emitted from a transition quadrupole with the $d_0 \rightarrow s$ transition and $J = 2$, $M = 0$ with the output from the code given in Fig. 4.4.6.

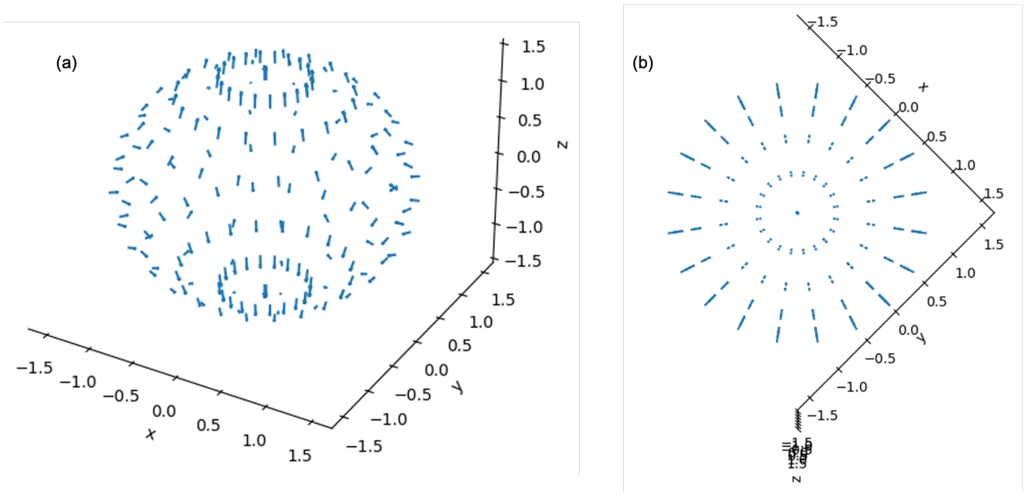

Figure 4.4.6: (a) plot of the electric field emanating from the $d_0 \rightarrow s$ transition characterised by the quantum numbers $J = 2$ and $M = 0$ at a radial distance where $kr = 1.5$ with (b) showing the top-down view.

Rather unremarkable, the overall field broadly speaking shows a similar structure when looking down the z-axis (Fig. 4.4.6(b)) to that associated with the field of the $p_0 \rightarrow s$ transition (Fig. 4.4.2(b)). This is unsurprising given the shapes of the both the d_0 and p_0 orbitals which have symmetry about the z-axis. However, when one looks at the field from a side-on perspective, Fig. 4.4.6(a), it can be seen that the structure is slightly more complex, especially in a region centred around the equator with angular dependencies that are not present in the dipole (Fig. 4.4.2(a)) case.

Moving on to the transitions $d_{-1} \rightarrow s$ with $J = 2$, $M = -1$ (Fig. 4.4.7) and $d_{+1} \rightarrow s$ with $J = 2$, $M = +1$ (Fig, 4.4.8).

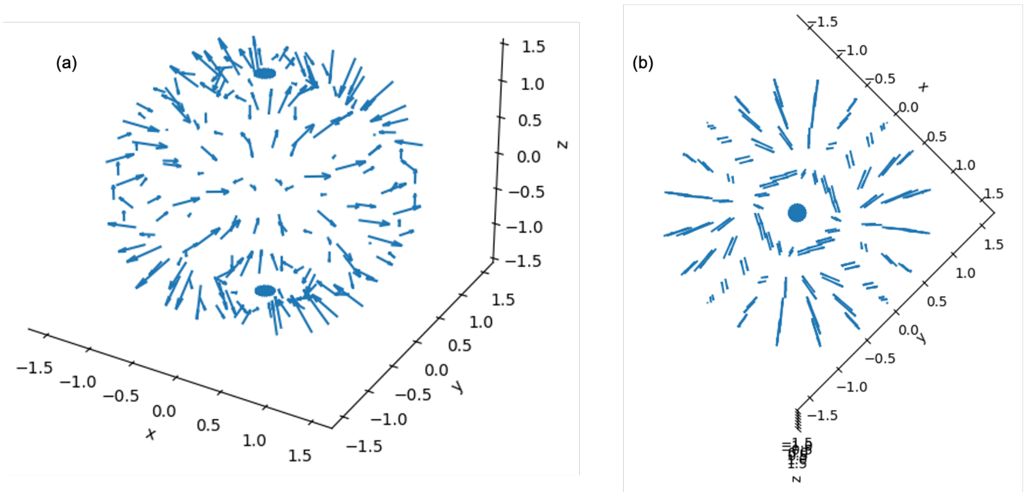

Figure 4.4.7: (a) plot of the electric field emanating from the $d_{-1} \rightarrow s$ transition characterised by the quantum numbers $J = 2$ and $M = -1$ at a radial distance where $kr = 1.5$ with (b) showing the top-down view.

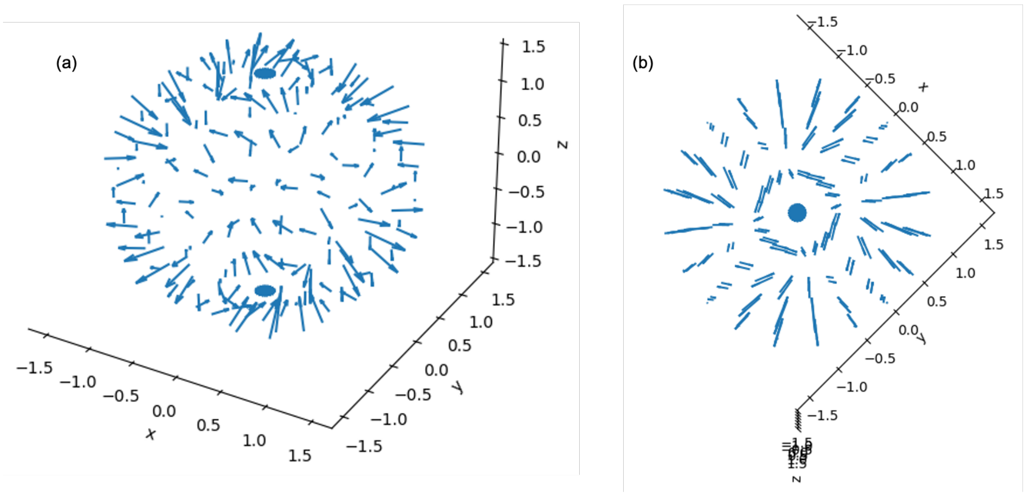

Figure 4.4.8: (a) plot of the electric field emanating from the $d_{+1} \rightarrow s$ transition characterised by the quantum numbers $J = 2$ and $M = +1$ at a radial distance where $kr = 1.5$ with (b) showing the top-down view.

Again, by comparing these with the dipole transitions (Figs. 4.4.3 and 4.4.4) we can make a number of observations. Looking down the z-axis we see broadly similar profiles for the corresponding instances of equivalent values of M, however the existence of any rotations associated with the circular polarisation of the light is not as pronounced. The lack of clarity in the directionality of the arrows in Figs. 4.4.7(b) and 4.4.8(b) may be a consequence of the slightly increased distance from the centre of the sphere at which the points the are plotted. Looking from the side-on perspective, one can again see a more complex field pattern. For example, a closer inspection of the left-hand side (towards the region where x is negative) of Figs. 4.4.8(a) and 4.4.8(a) appears to show that the field associated with the quadrupole transition has both negative and positive radial components, whereas the dipole transition yields a field with predominantly negative radial components. Although not necessarily in terms of the exact pictorial details, it can be said that broadly speaking these results are expected as light emanating from quadrupole transitions is thought to generate much more complex fields.

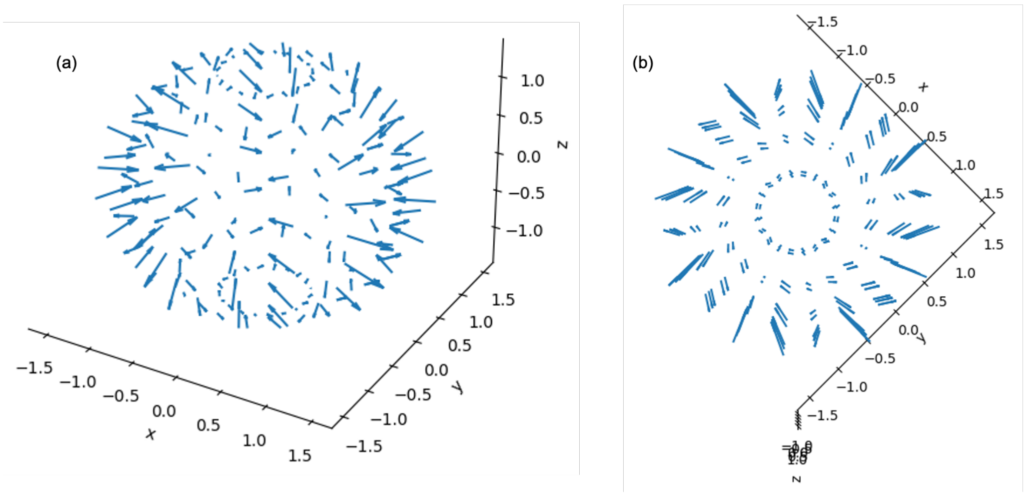

Figure 4.4.9: (a) plot of the electric field emanating from the $d_{-2} \rightarrow s$ transition characterised by the quantum numbers $J = 2$ and $M = -2$ at a radial distance where $kr = 1.5$ with (b) showing the top-down view.

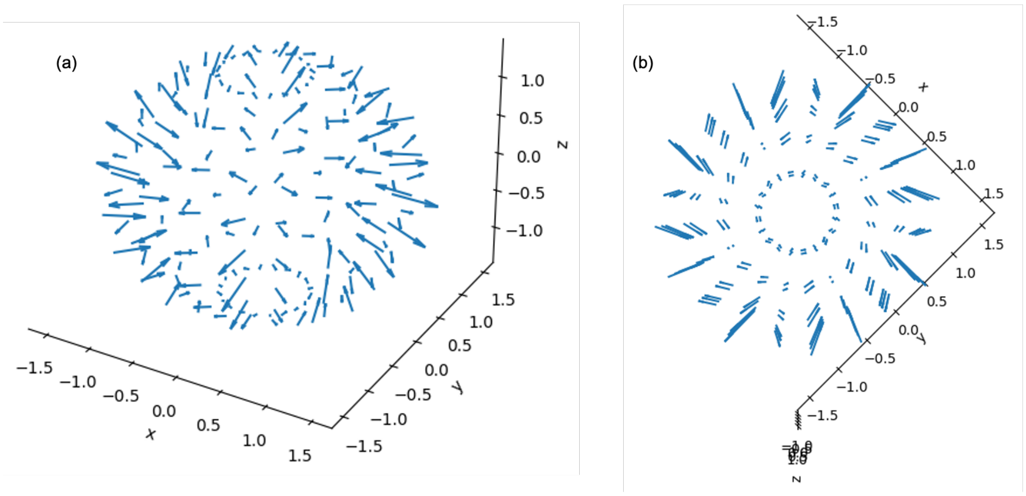

Figure 4.4.10: (a) plot of the electric field emanating from the $d_{+2} \rightarrow s$ transition characterised by the quantum numbers $J = 2$ and $M = +2$ at a radial distance where $kr = 1.5$ with (b) showing the top-down view.

As for transitions $d_{-2} \to s$ with $J = 2$, $M = -2$ (Fig. 4.4.9) and $d_{+2} \to s$ with $J = 2$, $M = +2$ (Fig, 4.4.10), we can now see much clearer indications of rotations about the z-axis. Of course, there are no analogous transitions for the dipole case, but one can again at least see the richness of the field patterns that emerge compared to the dipole generated plots that are possible. Closer inspection of Figs. 4.4.9(b) and 4.4.10(b) almost appear to suggest that there could be two separate sets of rotations occurring within the same image, with one set of arrows (those at points with the same value of ϕ and different values of θ) pointing in one direction and the adjacent set of arrows pointing in the close-to-exact opposite direction. While this would certainly complement the figures seen in Chapter 3 in which the phase of the electric field was seen to have a phase dependence in terms of a number of twists corresponding exactly to the magnetic (orbital) quantum number of that particular transition (Figs, 3.4.7 and 3.4.3), it is by no means obvious when looking at the field as presented here. A far more extensive analysis is required to exhaust the numerous viewing angles, radial distances and close-up images that are possible with the program that has been created. In this way it is hoped that the work presented here could serve to provide a useful tool for visualising and understanding the electric fields emanating from transition quadrupole moments in particular. In turn it is believed that some new and interesting insights can be captured.

Finally, the magnetic fields emanating from the five $d \to s$ transitions have been included for completeness and are shown in Fig. 4.4.11.

4.4.4 Phase of the Electric Field

Following on from the work of Chapter 3, one of the key motivators behind attempting the implementation of the SW approach for describing electromagnetic fields was to be able to further explore and understand the phase of the electric field as a means to exhibit the signatures of orbital angular momentum, especially with regards to the transition quadrupole moment. Now the electric fields have been calculated we can try to calculate and plot its phase. As noted in Section 4.3, a finer array of points should be used compared to the plotting of the arrows of the vector field in order to obtain a

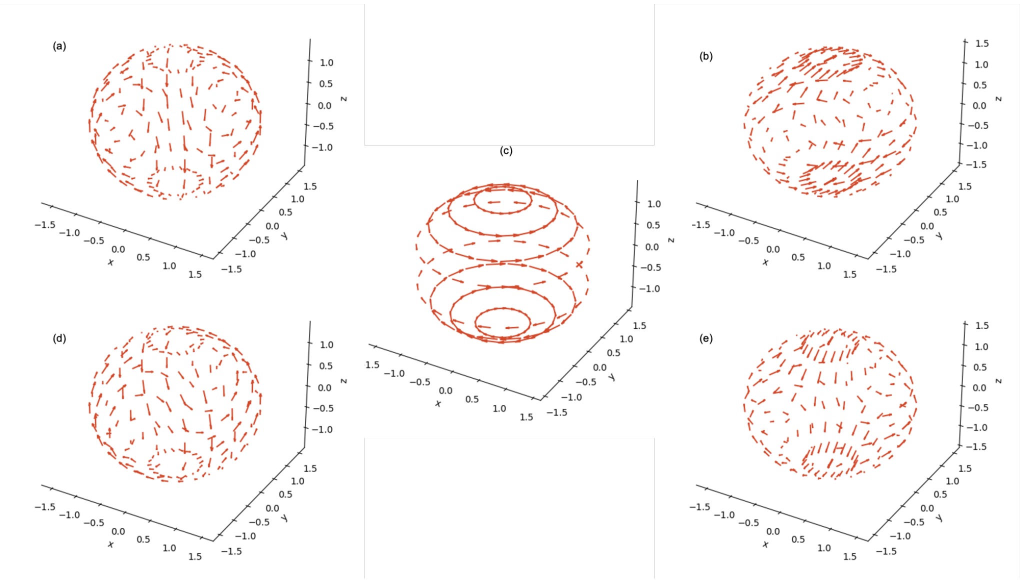

Figure 4.4.11: Plots of the magnetic fields emitted by (a) the $d_{+2} \to s$ transition ($J = 2$ and $M = +2$), (b) the $d_{+1} \to s$ transition ($J = 2$ and $M = +1$), (c) the $d_0 \to s$ transition ($J = 2$ and $M = 0$), (d) the $d_{-2} \to s$ transition ($J = 2$ and $M = +-$) and (e) the $d_{-1} \to s$ transition ($J = 2$ and $M = -1$) at a radial distance where $kr = 1$.

smoother image of the phase on the face of the sphere. As such a separate calculation of the electric field is required, however this is done in exactly the same way just with a finer array of points.

In the previous chapter the phase of the electric field was calculated by taking the argument of its separate Cartesian components, consistent with the method practised in Refs. [72, 95, 96]. The same calculation has been implemented in the code by employing the `angle` function from the Numpy library [100]. As before, it is the argument of the z component that is taken. To help assess the code, we start by plotting the phase of the z component of the electric field associated with the $p_0 \to s$ dipole transition with $J = 1$ and $M = 0$. This is shown in Fig. 4.4.12.

Before rendering the image in Fig. 4.4.12, the data has been normalised bringing the values into the range between 0 and 1 through the calculation

$$X' = \frac{X - X_{min}}{X_{max} - X_{min}}, \tag{4.4.8}$$

where X is the individual values of the phase data. Built-in colour maps from the Matplotlib library [110] based on the data were used to colour the face of the sphere

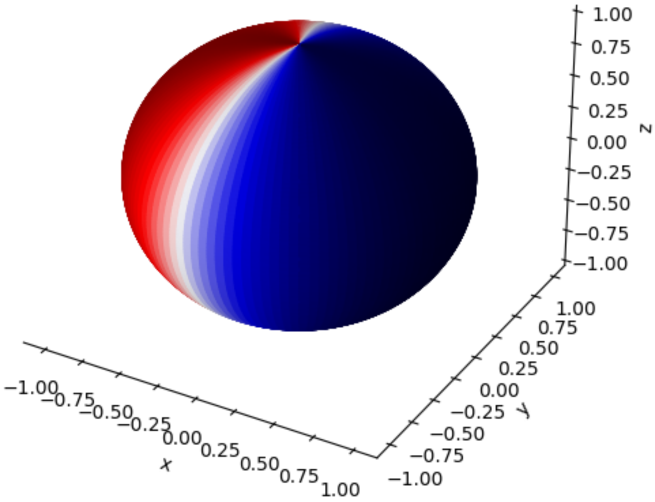

Figure 4.4.12: Plot of the phase (argument) of the z component of the electric field associated with the emission from the dipolar $p_0 \to s$ transition with $J = 1$ and $M = 0$ at a radial distance where $kr = 1$. The built-in Seismic colour map of the Matplotlib library [110] has been used to colour the face of the sphere.

and initial tests using the SSHs as well as the phase data indicated that more detailed plots were generated after the data was normalised. Comparing Fig. 4.4.12 with the equivalent figure of Fig. 3.4.2 in Chapter 3, somewhat surprisingly we do not see the concentric circles about the z-axis that we would be expecting from Fig. 3.4.2. If we look at Fig. 4.4.1(a), then we see, starting at the north pole and moving down either side (left and right) as we look at it, the arrows gradually point further away from the z-axis as you move down. This split across each hemisphere down the y-axis appears to be what is portrayed in Fig. 4.4.12.

One question mark regarding the difference between Figs. 4.4.12 and 3.4.2 is the colour map used. In Fig. 3.4.2 the `Hue` colour function in Mathematica [99] was employed while in Fig. 4.4.12 it was the `Seismic` colour map of the Python Matplotlib library [110]. As such, a way was found to generate a new colour map based on the Hue Saturation Value (hsv) of the phase data. After the initial plot with this colour map was generated, it is was determined that normalisation of the data was applicable here as well. The output is shown in Fig. 4.4.13.

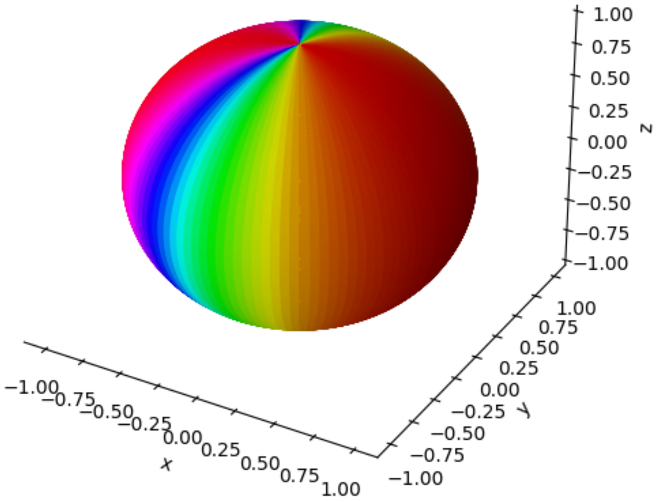

Figure 4.4.13: Plot of the phase (argument) of the z component of the electric field associated with the emission from the dipolar $p_0 \to s$ transition with $J = 1$ and $M = 0$ at a radial distance where $kr = 1$. A new colour map has been generated based on the hue (the hsv) of the phase data and subsequently applied to the face of the sphere.

Broadly similar to Fig. 4.4.12, Fig. 4.4.13, shows the same pattern but with slightly more detail in terms of colour changes. The figures suggest that the phase of the electric field is unchanging for a given of value of ϕ, and is different for a given value of θ. This last impression regarding the relationship to θ is inconsistent with that seen in Fig. 3.4.2. Closer examination of Fig. 4.4.1(a) does appear to show that the arrows situated at points in a circle with the same θ value are each angled equally away from the z-axis. This certainly supports the image seen in Fig. 3.4.2. With this in mind, it was deemed sensible to attempt to plot the electric field as in Fig. 4.4.1(a), but colour the arrows with the same normalised argument of the z component data used in Fig. 4.4.13, along with associated hsv colour map. The result is seen in Fig. 4.4.14.

Looking at Fig. 4.4.14 we clearly see that the arrows at points with the same value

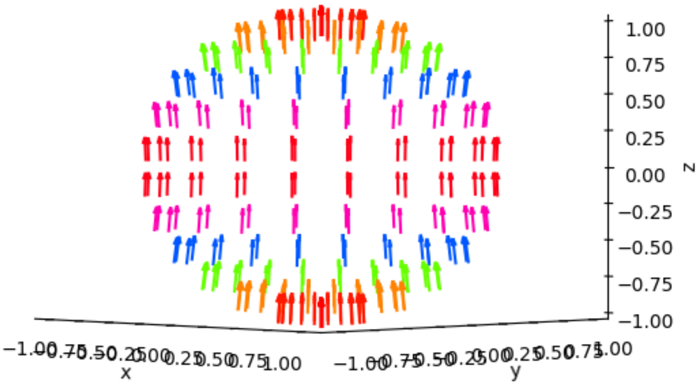

Figure 4.4.14: Plot of the electric field emanating from the $p_0 \rightarrow s$ transition characterised by the quantum numbers $J = 1$ and $M = 0$ at a radial distance where $kr = 1$ with the arrows coloured according to the normalised argument of the $\boldsymbol{z}$ component.

for θ are coloured identically. Rather than being an issue with the phase calculation or the code itself, this may suggest that there is an inherent discrepancy in the way that Matplotlib [110] takes the data and applies it to colour the face of the surface of a sphere. Unfortunately, this is a point that requires more understanding and would be the subject of further work. However, a brief attempt at an alternative way of calculating the phase of the electric field for this particular example does appear to support this suspicion. Given the plane nature of the viewpoint in the plots in Chapter 3, it was impulsively considered to calculate the angle between the $\boldsymbol{y}$ and $\boldsymbol{x}$ components of the electric field and plot that. To do so one simply takes the inverse tan ($arctan$) of $\frac{\boldsymbol{y}}{\boldsymbol{x}}$, however since $arctan$ cannot distinguish between the four quadrants of the Cartesian coordinate plane, programatically, the `arctan2` function of the Numpy library [100] has to be used. The resultant plot is shown in Fig. 4.4.15. As can be seen, this does indeed show the concentric rings about the z-axis we were originally expecting.

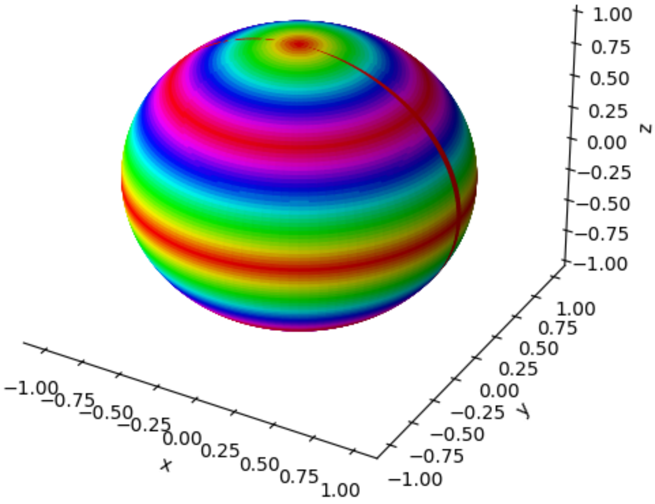

Figure 4.4.15: Plot of the phase of the electric field through the arctan calculation of the $\boldsymbol{y}$ component over the $\boldsymbol{x}$ component and subsequent normalisation. The field is that associated with emission from the dipolar $p_0 \rightarrow s$ transition with $J = 1$ and $M = 0$ at a radial distance where $kr = 1$. The colour map based on the hue (the hsv) of the data has been used to colour the face of the sphere.

However, contemplating the calculation more deeply, we realise that finding the angle between the $\boldsymbol{y}$ component and the $\boldsymbol{x}$ component of each vector is to calculate the angle in the x, y-plane for each arrow. Examination of Fig. 4.4.1(a) suggests that at points with a given value of θ, the x, y-angle changes. Once again by plotting the normalised $arctan$ generated colour map as the colour of the arrows in Fig. 4.4.16, we show this to be the case.

So, even though it is exactly the same calculation being carried out to generate the appropriate colour map, the two results show different projections of the data. Considering Figs. 4.4.13, 4.4.14, 4.4.15 and 4.4.16 all together does seem to give the impression that when used to colour the face of the surface of the sphere, the colour map data is being applied in a different direction to what was expected. All of this leads to the question of what angle is of most importance when considering the phase of the

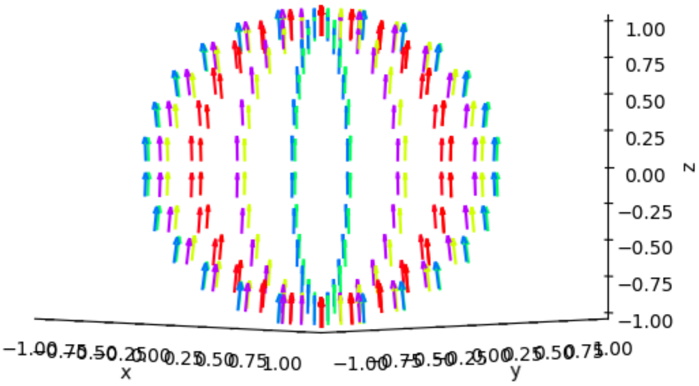

Figure 4.4.16: Plot of the electric field emanating from the $p_0 \rightarrow s$ transition characterised by the quantum numbers $J = 1$ and $M = 0$ at a radial distance where $kr = 1$. The arrows are coloured using a colour map based on the normalised data from the Arctan calculation of the $\boldsymbol{y}$ component over the $\boldsymbol{x}$ component of the electric field.

electric field, and what angle was examined in the other publications that presented the phase [72, 95, 96]? Therefore, at this stage, the calculation and plotting of the phase of the electric field does require far more careful consideration and no real insights or conclusions can be garnered. However, it is hoped that a few detailed inspections of the code and further experimentation in the future will lead to some swift results and provide some interesting perspectives of the electric field and its phase.

4.4.5 Future Investigations

A final aspect of this research that requires further investigation relates to the uncertainty raised earlier relating to the significance of the central axis in all of the plots. Whether talking about left-/right- circularly polarised light or contemplating the orbital angular momentum associated with electromagnetic radiation, the description is always given through consideration of the progression of the phase of the electric field along the direction of propagation. It would therefore be interesting to continue viewing the phase on the surface of the sphere, but rather than do so by calculating an angle made to any axis, do so through a calculation of the angle made between the electric field vector and the vector associated with the point on the sphere, i.e. the direction of observation. Code has been added that makes an attempt at doing this, however, far more analysis is required before reliable results can be generated. In pondering the importance of the central z-axis, one premise initially put forward was that it was an axis of symmetry, much in the same way as Williams *et al.* described the figures in their work with chromophore arrays [95, 96]. However, this rekindled some of the same misgivings that were briefly discussed in Chapter 3 relating to the implication of viewing the electric field associated with the orbitals, or in this case VSHs, of a complex space on a real axis generated by computer programs. Further work can therefore be carried out to calculate combinations of the spherical basis VSHs to create real VSHs and plot the electric fields created when those are considered. While this creates ambiguity regarding the value of M for the resulting VSHs, it is hoped that with more figures and information, a more definitive interpretation could be reached. The way the code is currently constructed makes this quite awkward for the generation of the fields emitted from electric quadrupole moments, nevertheless efforts have been made to do so for fields associated with electric dipole moments. These results and their reliability, however, are still very much in their infancy and require much more verification and analysis.

What the figures relating to the phase have shown is that more effort is required to establish how the plotting commands are executed and this in turn should help to discern the true nature of the plots we seek. It is then hoped that a greater comprehension of the phase of the electric field can be achieved, both with regards to its calculation and visualisation. Initially found by simply taking the argument of a complex number to yield the notion of the phase as the angle made to the positive real axis in the complex plane, this work has raised questions concerning how this angle relates to the phase of a wave/field (and our view of it), what it may mean to only consider a particular Cartesian component of the electric field, and what angles/directions are truly important when contemplating the phase. All in all, although there is a lot that remains unanswered and unclear within this research, there continues to be plenty of avenues for further investigation and a strong prospect of generating some fundamental and genuinely interesting insights into the phase of the electric field, structured light and their connections to the electric quadrupole transition moment.

5

Conclusion

Throughout this thesis computational models, developed on the basis of the unified theory of RET built through the framework of molecular quantum electrodynamics, have been used to investigate the influence and significance of the transition quadrupole moment. It started with a study into the specific effects seen on the coupling between two species and has led to intriguing work exploring the very nature of light itself, creating tools that can be used in the future to gain fundamental insights.

In Chapter 2 we saw the specific orientational and positional dependency of the next highest order terms in the description of the coupling between two J-aggregate dye molecules. Although in a broader picture much of the influence of the dipole-quadrupole terms was overwhelmed by the typical dipole-dipole coupling, the inspection of a pair of chromophores showed these extra terms can have a significant impact. Not only that, but the effects could be seen at distances that are appreciable in the construction of some nanomaterials. The results therefore highlight the importance of the transition quadrupole moment in accurate descriptions of the coupling that governs EET, and also possible design cues for efficient materials. With the model created, more conclusions could be reached by carrying out future studies that examine more relevant transitions/molecules to the transition quadrupole moment, such as hexahelicenes or chiral molecules. Being able to better understand the directional aspects of RET would be of high significance for the application of RET in biomolecules.

Chapter 3 saw the start of the shift in thinking from looking at the effect of the quadrupole to instead examining the fundamental characteristics of transitions governed by a quadrupole moment through the calculation of the electric field. By visualising the phase of the electric field associated with emission from each of the five $3d$ orbitals of the hydrogen atom, the conversation was started regarding angular momentum, structured light and the transition quadrupole moment. Two key questions arose from this; (1) is the phase (as we plot here) able to discriminate between spin angular momentum and orbital angular momentum, and (2) what is the significance of the central axis and how is the law of conservation of angular momentum followed? This all motivated the work in the final chapter.

Finally, Chapter 4 built on the experiences captured through Chapter 3 by finding an alternative, more intuitive and computationally useful way to now not only plot the electric and magnetic fields, but also offer a different perspective on the phase of the electric field seen in Chapter 3. In conjunction, an examination of the so-called spherical wave approach was carried out, identifying its suitability to create a program that allows for the quick and easy modelling of the fields, simply by providing two quantum numbers and a radial distance. Ultimately, more time and effort is needed to have confidence in the plots of the phase of the electric field, however, the groundwork has been set. A fundamental issue related to the angular momentum of light arose in the context of this work. It highlights the fact that a photon emanating from a quadrupole transition can be absorbed by a dipole transition. On first take this sounds nonsensical as when considering purely electronic processes it would appear that the law of conservation of angular momentum is violated. However, because the photon is absorbed at a single point (at a specific θ and ϕ on the surface of the sphere in the computational model), all angular information is lost and the photon will give only one unit of angular momentum to a dipole transition. Future work could develop the model to explore whether the other unit is lost (possibly mechanically to the centre of mass of the atom). This fact also highlights the question regarding the significance of the axis if that is about which the angular nature of the light is determined. Therefore, further investigations into the angle with respect to which the phase is examined could be investigated, in part by code that has already been implemented that considers the direction of observation. All of these possibilities from the computational program that has been developed could lead to some fascinating insights and result in a better practical understanding of various optical processes.

Bibliography

[1] R. Grinter and G. A. Jones, “Resonance energy transfer: The unified theory via vector spherical harmonics”, *J. Chem. Phys.* **145**, 074107 (2016).

[2] R. E. Blankenship, “Origin and early evolution of photosynthesis”, *Photosynth. Res.* **33**, 91 (1992).

[3] R. Croce and H. van Amerongen, “Natural strategies for photosynthetic light harvesting”, *Nat. Chem. Biol.* **10**, 492 (2014).

[4] D. Narzi, D. Bovi, P. De Gaetano, and L. Guidoni, “Dynamics of the Special Pair of Chlorophylls of Photosystem II”, *J. Am. Chem. Soc.* **138**, 257 (2016).

[5] D. L. Andrews and A. A. Demidov, eds., *Resonance Energy Transfer* (Wiley, Chichester, 1999).

[6] D. Mauzerall and N. L. Greenbaum, “The absolute size of a photosynthetic unit”, *Biochim. Biophys. Acta - Bioenerg.* **974**, 119 (1989).

[7] V. Sundström, T. Pullerits, and R. van Grondelle, “Photosynthetic Light-Harvesting: Reconciling Dynamics and Structure of Purple Bacterial LH2 Reveals Function of Photosynthetic Unit”, *J. Phys. Chem. B* **103**, 2327 (1999).

[8] R. S. Knox, “Electronic excitation transfer in the photosynthetic unit: Reflections on work of William Arnold”, *Photosynth. Res.* **48**, 35 (1996).

[9] R. J. Cogdell and J. G. Lindsay, "Can photosynthesis provide a 'biological blueprint' for the design of novel solar cells?", *Trends Biotechnol.* **16**, 521 (1998).

[10] J. M. Anna, G. D. Scholes, and R. van Grondelle, "A Little Coherence in Photosynthetic Light Harvesting", *BioScience* **64**, 14 (2014).

[11] R. van Grondelle, J. P. Dekker, T. Gillbro, and V. Sundström, "Energy transfer and trapping in photosynthesis", *Biochim. Biophys. Acta - Bioenerg.* **1187**, 1 (1994).

[12] J.-L. Brédas, D. Beljonne, V. Coropceanu, and J. Cornil, "Charge-Transfer and Energy-Transfer Processes in π-Conjugated Oligomers and Polymers: A Molecular Picture", *Chem. Rev.* **104**, 4971 (2004).

[13] G. S. Engel, T. R. Calhoun, E. L. Read, T.-K. Ahn, T. Mančal, Y.-C. Cheng, R. E. Blankenship, and G. R. Fleming, "Evidence for wavelike energy transfer through quantum coherence in photosynthetic systems", *Nature* **446**, 782 (2007).

[14] G. D. Scholes, G. R. Fleming, A. Olaya-Castro, and R. van Grondelle, "Lessons from nature about solar light harvesting", *Nat. Chem.* **3**, 763 (2011).

[15] L. A. Pachón and P. Brumer, "Computational methodologies and physical insights into electronic energy transfer in photosynthetic light-harvesting complexes", *Phys. Chem. Chem. Phys.* **14**, 10094 (2012).

[16] G. D. Scholes, X. J. Jordanides, and G. R. Fleming, "Adapting the Förster Theory of Energy Transfer for Modeling Dynamics in Aggregated Molecular Assemblies", *J. Phys. Chem. B* **105**, 1640 (2001).

[17] B. P. Krueger, G. D. Scholes, and G. R. Fleming, "Calculation of Couplings and Energy-Transfer Pathways between the Pigments of LH2 by the ab Initio Transition Density Cube Method", *J. Phys. Chem. B* **102**, 5378 (1998).

[18] G. D. Scholes and K. P. Ghiggino, "Electronic Interactions and Interchromophore Excitation Transfer", *J. Phys. Chem.* **98**, 4580 (1994).

[19] G. D. Scholes, "Long-Range Resonance Energy Transfer in Molecular Systems", *Annu. Rev. Phys. Chem.* **54**, 57 (2003).

[20] C.-P. Hsu, “The Electronic Couplings in Electron Transfer and Excitation Energy Transfer”, *Acc. Chem. Res.* **42**, 509 (2009).

[21] Z.-Q. You and C.-P. Hsu, “Theory and calculation for the electronic coupling in excitation energy transfer”, *Int. J. Quantum Chem.* **114**, 102 (2014).

[22] T. Förster, “Zwischenmolekulare Energiewanderung und Fluoreszenz”, *Ann. Phys.* **437**, 55 (1948).

[23] D. L. Andrews and J. M. Leeder, “Resonance energy transfer: when a dipole fails.”, *J. Chem. Phys.* **130**, 184504 (2009).

[24] D. Beljonne, C. Curutchet, G. D. Scholes, and R. J. Silbey, “Beyond Förster Resonance Energy Transfer in Biological and Nanoscale Systems”, *J. Phys. Chem. B* **113**, 6583 (2009).

[25] D. L. Andrews, D. S. Bradshaw, R. D. Jenkins, and J. Rodríguez, “Dendrimer light-harvesting: intramolecular electrodynamics and mechanisms.”, *Dalton Trans.* 10006 (2009).

[26] K. Zheng, K. Žídek, M. Abdellah, N. Zhu, P. Chábera, N. Lenngren, Q. Chi, and T. Pullerits, “Directed Energy Transfer in Films of CdSe Quantum Dots: Beyond the Point Dipole Approximation”, *J. Am. Chem. Soc.* **136**, 6259 (2014).

[27] R. Baer and E. Rabani, “Theory of resonance energy transfer involving nanocrystals: the role of high multipoles.”, *J. Chem. Phys.* **128**, 184710 (2008).

[28] B. Mennucci and C. Curutchet, “The role of the environment in electronic energy transfer: a molecular modeling perspective.”, *Phys. Chem. Chem. Phys.* **13**, 11538 (2011).

[29] G. D. Scholes, C. Curutchet, B. Mennucci, R. Cammi, and J. Tomasi, “How solvent controls electronic energy transfer and light harvesting.”, *J. Phys. Chem. B* **111**, 6978 (2007).

[30] A. Muñoz Losa, C. Curutchet, B. P. Krueger, L. R. Hartsell, and B. Mennucci, “Fretting about FRET: failure of the ideal dipole approximation.”, *Biophys. J.* **96**, 4779 (2009).

[31] J. E. Frost and G. A. Jones, “A quantum dynamical comparison of the electronic couplings derived from quantum electrodynamics and Förster theory: application to 2D molecular aggregates”, *New J. Phys.* **16**, 113067 (2014).

[32] J. S. Avery, “The retarded dipole-dipole interaction in exciton theory”, *Proc. Phys. Soc.* **89**, 677 (1966).

[33] E. A. Power and S. Zienau, “Coulomb gauge in non-relativistic quantum electrodynamics and the shape of spectral lines”, *Philos. Trans. R. Soc. London. Ser. A, Math. Phys. Sci.* **251**, 427 (1959).

[34] R. G. Woolley, “Molecular quantum electrodynamics”, *Proc. R. Soc. London. A. Math. Phys. Sci.* **321**, 557 (1971).

[35] D. P. Craig and T. Thirunamachandran, “Radiation–Molecule Interactions in Chemical Physics”, in, Vol. 16, edited by P.-O. Löwdin, Advances in Quantum Chemistry (Academic Press, 1982), pp. 97–160.

[36] D. P. Craig and T. Thirunamachandran, *Molecular Quantum Electrodynamics: An Introduction to Radiation Molecule Interactions*, Dover Edit (Dover Publications, INC., Mineola, New York, 1998).

[37] D. L. Andrews, “A unified theory of radiative and radiationless molecular energy transfer”, *Chem. Phys.* **135**, 195 (1989).

[38] G. J. Daniels, R. D. Jenkins, D. S. Bradshaw, and D. L. Andrews, “Resonance energy transfer: The unified theory revisited”, *J. Chem. Phys.* **119**, 2264 (2003).

[39] M. P. E. Lock, D. L. Andrews, and G. A. Jones, “On the nature of long range electronic coupling in a medium: Distance and orientational dependence for chromophores in molecular aggregates”, *J. Chem. Phys.* **140**, 044103 (2014).

[40] G. A. Jones and D. S. Bradshaw, “Resonance Energy Transfer: From Fundamental Theory to Recent Applications”, *Front. Phys.* **7**, 100 (2019).

[41] A. Dreuw and M. Head-Gordon, “Single-Reference ab Initio Methods for the Calculation of Excited States of Large Molecules”, *Chem. Rev.* **105**, 4009 (2005).

[42] S. Tretiak and S. Mukamel, “Density Matrix Analysis and Simulation of Electronic Excitations in Conjugated and Aggregated Molecules”, *Chem. Rev.* **102**, 3171 (2002).

[43] D. L. Andrews, C. Curutchet, and G. D. Scholes, “Resonance energy transfer: Beyond the limits”, *Laser Photon. Rev.* **5**, 114 (2011).

[44] G. D. Scholes, R. D. Harcourt, and G. R. Fleming, “Electronic Interactions in Photosynthetic Light-Harvesting Complexes: The Role of Carotenoids”, *J. Phys. Chem. B* **101**, 7302 (1997).

[45] K. F. Wong, B. Bagchi, and P. J. Rossky, “Distance and Orientation Dependence of Excitation Transfer Rates in Conjugated Systems: Beyond the Förster Theory”, *J. Phys. Chem. A* **108**, 5752 (2004).

[46] M. E. Madjet, A Abdurahman, and T Renger, “Intermolecular Coulomb Couplings from Ab Initio Electrostatic Potentials: Application to Optical Transitions of Strongly Coupled Pigments in Photosynthetic Antennae and Reaction Centers”, *J. Phys. Chem. B* **110**, 17268 (2006).

[47] W. J. D. Beenken and T. Pullerits, “Excitonic coupling in polythiophenes: Comparison of different calculation methods”, *J. Chem. Phys.* **120**, 2490 (2004).

[48] J. C. Chang, “Monopole effects on electronic excitation interactions between large molecules. I. Application to energy transfer in chlorophylls”, *J. Chem. Phys.* **67**, 3901 (1977).

[49] A. P. Alivisatos, W. Gu, and C. Larabell, “Quantum dots as cellular probes.”, *Annu. Rev. Biomed. Eng.* **7**, 55 (2005).

[50] A. R. Clapp, I. L. Medintz, and H. Mattoussi, “Förster resonance energy transfer investigations using quantum-dot fluorophores.”, *Chemphyschem* **7**, 47 (2006).

[51] V. I. Klimov, A. A. Mikhailovsky, X. Su, A. Malko, J. A. Hollingsworth, C. A. Leatherdale, H.-J. Eisler, and M. G. Bawendi, “Optical Gain and Stimulated Emission in Nanocrystal Quantum Dots”, *Science* **290**, 314 (2000).

[52] P. V. Kamat, “Quantum Dot Solar Cells. Semiconductor Nanocrystals as Light Harvesters”, *J. Phys. Chem. C* **112**, 18737 (2008).

[53] A. Nozik, “Quantum dot solar cells”, *Phys. E Low-dimensional Syst. Nanostructures* **14**, 115 (2002).

[54] I. Robel, V. Subramanian, M. Kuno, and P. V. Kamat, “Quantum Dot Solar Cells. Harvesting Light Energy with CdSe Nanocrystals Molecularly Linked to Mesoscopic TiO_2 Films”, *J. Am. Chem. Soc.* **128**, 2385 (2006).

[55] G. D. Scholes and D. L. Andrews, “Resonance energy transfer and quantum dots”, *Phys. Rev. B* **72**, 125331 (2005).

[56] C. R. Kagan, C. B. Murray, M. Nirmal, and M. G. Bawendi, “Electronic Energy Transfer in CdSe Quantum Dot Solids”, *Phys. Rev. Lett.* **76**, 3043 (1996).

[57] C. Curutchet, A. Franceschetti, A. Zunger, and G. D. Scholes, “Examining Förster Energy Transfer for Semiconductor Nanocrystalline Quantum Dot Donors and Acceptors”, *J. Phys. Chem. C* **112**, 13336 (2008).

[58] G. Beane, K. Boldt, N. Kirkwood, and P. Mulvaney, “Energy Transfer between Quantum Dots and Conjugated Dye Molecules”, *J. Phys. Chem. C* **118**, 18079 (2014).

[59] G. Wang, Q. Peng, and Y. Li, “Lanthanide-doped nanocrystals: synthesis, optical-magnetic properties, and applications.”, *Acc. Chem. Res.* **44**, 322 (2011).

[60] H. Wang, C.-k. Duan, and P. A. Tanner, “Visible Upconversion Luminescence from $Y_2O_3 : Eu^{3+}, Yb^{3+}$”, *J. Phys. Chem. C* **112**, 16651 (2008).

[61] I. T. Weber, I. A. A. Terra, A. J. G. de Melo, M. A. d. M. Lucena, K. A. Wanderley, C. d. O. Paiva-Santos, S. G. Antônio, L. A. O. Nunes, F. A. A. Paz, G. F. de Sá, S. A. Júnior, and M. O. Rodrigues, “Up-conversion properties of lanthanide-organic frameworks and how to track ammunitions using these materials”, *RSC Adv.* **2**, 3083 (2012).

[62] P. Selvin, “Lanthanide-Based Resonance Energy Transfer”, *IEEE J. Sel. Top. Quantum Electron.* **2**, 1077 (1996).

[63] D. Geißler, S. Linden, K. Liermann, K. D. Wegner, L. J. Charbonnière, and N. Hildebrandt, "Lanthanides and Quantum Dots as Förster Resonance Energy Transfer Agents for Diagnostics and Cellular Imaging", *Inorg. Chem.* **53**, 1824 (2014).

[64] M. O. Rodrigues, J. D. L. Dutra, L. A. O. Nunes, G. F. de Sá, W. M. de Azevedo, P. Silva, F. A. A. Paz, R. O. Freire, and S. A. Júnior, "$Tb^{3+} \rightarrow Eu^{3+}$ Energy Transfer in Mixed-Lanthanide-Organic Frameworks", *J. Phys. Chem. C* **116**, 19951 (2012).

[65] O. Malta, "Mechanisms of non-radiative energy transfer involving lanthanide ions revisited", *J. Non. Cryst. Solids* **354**, 4770 (2008).

[66] D. L. Andrews and R. D. Jenkins, "A quantum electrodynamical theory of three-center energy transfer for upconversion and downconversion in rare earth doped materials", *J. Chem. Phys.* **114**, 1089 (2001).

[67] R. D. Jenkins, G. J. Daniels, and D. L. Andrews, "Quantum pathways for resonance energy transfer", *J. Chem. Phys.* **120**, 11442 (2004).

[68] D. L. Andrews and D. S. Bradshaw, "Virtual photons, dipole fields and energy transfer: a quantum electrodynamical approach", *Eur. J. Phys.* **25**, 845 (2004).

[69] G. D. Scholes and D. L. Andrews, "Damping and higher multipole effects in the quantum electrodynamical model for electronic energy transfer in the condensed phase", *J. Chem. Phys.* **107**, 5374 (1997).

[70] S. Valleau, S. K. Saikin, M.-H. Yung, and A. A. Guzik, "Exciton transport in thin-film cyanine dye J-aggregates", *J. Chem. Phys.* **137**, 034109 (2012).

[71] I. S. Gradshteyn and I. M. Ryzhik, *Table of Integrals, Series, and Products*, edited by D. Zwillinger and V. Moll, 8th (Elsevier, 2015).

[72] E. M. Rice, D. S. Bradshaw, K. Saadi, and D. L. Andrews, "Identifying the development in phase and amplitude of dipole and multipole radiation", *Eur. J. Phys.* **33**, 345 (2012).

[73] A. Salam, “A general formula for the rate of resonant transfer of energy between two electric multipole moments of arbitrary order using molecular quantum electrodynamics”, *J. Chem. Phys.* **122**, 044112 (2005).

[74] L. C. Dávila Romero and D. L. Andrews, “A retarded coupling approach to intermolecular interactions”, *J. Phys. B At. Mol. Opt. Phys.* **42**, 085403 (2009).

[75] S. Mukamel, *Principles of Nonlinear Optical Spectroscopy*, Paperback (Oxford University Press, New York, New York, 1999), p. 576.

[76] P. C. Hariharan and J. A. Pople, “The influence of polarization functions on molecular orbital hydrogenation energies”, *Theor. Chim. Acta* **28**, 213 (1973).

[77] M. J. Frisch, G. W. Trucks, H. B. Schlegel, G. E. Scuseria, M. A. Robb, J. R. Cheeseman, G Scalmani, V Barone, B Mennucci, G. A. Petersson, H Nakatsuji, M Caricato, X Li, H. P. Hratchian, A. F. Izmaylov, J Bloino, G Zheng, J. L. Sonnenberg, M Hada, M Ehara, K Toyota, R Fukuda, J Hasegawa, M Ishida, T Nakajima, Y Honda, O Kitao, H Nakai, T Vreven, J. A. Montgomery Jr., J. E. Peralta, F Ogliaro, M Bearpark, J. J. Heyd, E Brothers, K. N. Kudin, V. N. Staroverov, R Kobayashi, J Normand, K Raghavachari, A Rendell, J. C. Burant, S. S. Iyengar, J Tomasi, M Cossi, N Rega, J. M. Millam, M Klene, J. E. Knox, J. B. Cross, V Bakken, C Adamo, J Jaramillo, R Gomperts, R. E. Stratmann, O Yazyev, A. J. Austin, R Cammi, C Pomelli, J. W. Ochterski, R. L. Martin, K Morokuma, V. G. Zakrzewski, G. A. Voth, P Salvador, J. J. Dannenberg, S Dapprich, A. D. Daniels, Ö. Farkas, J. B. Foresman, J. V. Ortiz, J Cioslowski, and D. J. Fox, *Gaussian 09, Revision C.01*, Gaussian Inc. Wallingford, CT, 2009.

[78] R. Dennington, T. Keith, and J. Millam, *GaussView Version 5*, Semichem Inc. Shawnee Mission KS, 2009.

[79] B. Simmen, E. Mátyus, and M. Reiher, “Electric transition dipole moment in pre-Born–Oppenheimer molecular structure theory”, *J. Chem. Phys.* **141**, 154105 (2014).

[80] S. Bernadotte, A. J. Atkins, and C. R. Jacob, “Origin-independent calculation of quadrupole intensities in X-ray spectroscopy.”, *J. Chem. Phys.* **137**, 204106 (2012).

[81] C. Díaz, Y. Vesga, L. Echevarria, I. G. Stará, I. Starỳ, E. Anger, C. Shen, M. El Sayed Moussa, N. Vanthuyne, J. Crassous, A. Rizzo, and F. E. Hernández, “Two-photon absorption and two-photon circular dichroism of hexahelicene derivatives: a study of the effect of the nature of intramolecular charge transfer”, *RSC Adv.* **5**, 17429 (2015).

[82] K. Bakke, “On the interaction between an electric quadrupole moment and electric fields”, *Ann. Phys.* **524**, 338 (2012).

[83] D. L. Andrews, “Optical angular momentum: Multipole transitions and photonics”, *Phys. Rev. A* **81**, 033825 (2010).

[84] B. S. Davis, L. Kaplan, and J. H. McGuire, “On the exchange of orbital angular momentum between twisted photons and atomic electrons”, *J. Opt.* **15**, 035403 (2013).

[85] D. L. Andrews, ed., *Structured Light and Its Applications: An Introduction to Phase-Structured Beams and Nanoscale Optical Forces* (Academic Press, Burlington, MA, 2008).

[86] D. L. Andrews and M. Babiker, eds., *The Angular Momentum of Light* (Cambridge University Press, Cambridge, 2012).

[87] A. Afanasev, C. E. Carlson, and A. Mukherjee, “Off-axis excitation of hydrogenlike atoms by twisted photons”, *Phys. Rev. A* **88**, 033841 (2013).

[88] A. Afanasev, C. E. Carlson, and A. Mukherjee, “High-multipole excitations of hydrogen-like atoms by twisted photons near a phase singularity”, *J. Opt.* **18**, 074013 (2016).

[89] C. T. Schmiegelow, J. Schulz, H. Kaufmann, T. Ruster, U. G. Poschinger, and F. Schmidt-Kaler, “Transfer of optical orbital angular momentum to a bound electron”, *Nat. Commun.* **7**, 12998 (2016).

[90] X. Zang and M. T. Lusk, “Twisted molecular excitons as mediators for changing the angular momentum of light”, *Phys. Rev. A* **96**, 013819 (2017).

[91] M. Babiker, C. R. Bennett, D. L. Andrews, and L. C. Dávila Romero, “Orbital Angular Momentum Exchange in the Interaction of Twisted Light with Molecules”, *Phys. Rev. Lett.* **89**, 143601 (2002).

[92] A. Afanasev, C. E. Carlson, C. T. Schmiegelow, J. Schulz, F. Schmidt-Kaler, and M. Solyanik, “Experimental verification of position-dependent angular-momentum selection rules for absorption of twisted light by a bound electron”, *New J. Phys.* **20**, 023032 (2018).

[93] S. Bougouffa, “Quadrupole absorption rate for atoms in circularly-polarized optical vortices”, *Results Phys.* **27**, 104541 (2021).

[94] K. A. Forbes, “On the transfer of optical orbital angular momentum to matter”, (2021).

[95] M. D. Williams, M. M. Coles, K. Saadi, D. S. Bradshaw, and D. L. Andrews, “Optical Vortex Generation from Molecular Chromophore Arrays”, *Phys. Rev. Lett.* **111**, 153603 (2013).

[96] M. D. Williams, M. M. Coles, D. S. Bradshaw, and D. L. Andrews, “Direct generation of optical vortices”, *Phys. Rev. A* **89**, 033837 (2014).

[97] A. Salam, *Molecular Quantum Electrodynamics: Long-Range Intermolecular Interactions* (John Wiley & Sons, Inc., Hoboken, NJ, USA, 2010).

[98] D. H. Berman, “An extinction theorem for electromagnetic waves in a point dipole model”, *Am. J. Phys.* **71**, 917 (2003).

[99] Wolfram Research, Inc., *Mathematica, Version 11.1*, Champaign, IL, 2017.

[100] C. R. Harris, K. J. Millman, S. J. van der Walt, R. Gommers, P. Virtanen, D. Cournapeau, E. Wieser, J. Taylor, S. Berg, N. J. Smith, R. Kern, M. Picus, S. Hoyer, M. H. van Kerkwijk, M. Brett, A. Haldane, J. F. del Río, M. Wiebe, P. Peterson, P. Gérard-Marchant, K. Sheppard, T. Reddy, W. Weckesser, H. Abbasi, C. Gohlke, and T. E. Oliphant, “Array programming with NumPy”, *Nature* **585**, 357 (2020).

[101] E. W. Weisstein, *"Spherical Hankel Function of the First Kind." From MathWorld — A Wolfram Web Resource — https://mathworld.wolfram.com/SphericalHankelFunctionoftheFirstKind.html.*

[102] R. Grinter, "Photon angular momentum: selection rules and multipolar transition moments", *J. Phys. B: At. Mol. Opt. Phys.* **41**, 095001 (2008).

[103] R. Grinter, "Characterizing emitted electromagnetic radiation: the vector-spherical-harmonic/Bessel-function description", *J. Phys. B: At. Mol. Opt. Phys.* **47**, 075004 (2014).

[104] R. Grinter and G. A. Jones, "Interpreting angular momentum transfer between electromagnetic multipoles using vector spherical harmonics", *Opt. Lett.* **43**, 367 (2018).

[105] G. A. Jones and R. Grinter, "The plane- and spherical-wave descriptions of electromagnetic radiation: a comparison and discussion of their relative merits", *Eur. J. Phys.* **39**, 053001 (2018).

[106] M. Weissbluth, *Atoms and Molecules* (Academic Press, London, 1978).

[107] V. P. Krainov, H. R. Reiss, and B. M. Smirnov, "Appendix B: Clebsch–Gordan Coefficients", in *Radiat. process. at. phys.* (John Wiley & Sons, Ltd, 1997), p. 235.

[108] J. D. Jackson, *Classical Electrodynamics*, 1st (John Wiley & Sons, Inc., New York; London, 1962).

[109] P. Virtanen, R. Gommers, T. E. Oliphant, M. Haberland, T. Reddy, D. Cournapeau, E. Burovski, P. Peterson, W. Weckesser, J. Bright, S. J. van der Walt, M. Brett, J. Wilson, K. J. Millman, N. Mayorov, A. R. J. Nelson, E. Jones, R. Kern, E. Larson, C. J. Carey, İ. Polat, Y. Feng, E. W. Moore, J. VanderPlas, D. Laxalde, J. Perktold, R. Cimrman, I. Henriksen, E. A. Quintero, C. R. Harris, A. M. Archibald, A. H. Ribeiro, F. Pedregosa, P. van Mulbregt, A. Vijaykumar, A. P. Bardelli, A. Rothberg, A. Hilboll, A. Kloeckner, A. Scopatz, A. Lee, A. Rokem, C. N. Woods, C. Fulton, C. Masson, C. Häggström, C. Fitzgerald, D. A. Nicholson, D. R. Hagen,

D. V. Pasechnik, E. Olivetti, E. Martin, E. Wieser, F. Silva, F. Lenders, F. Wilhelm, G Young, G. A. Price, G.-L. Ingold, G. E. Allen, G. R. Lee, H. Audren, I. Probst, J. P. Dietrich, J. Silterra, J. T. Webber, J. Slavič, J. Nothman, J. Buchner, J. Kulick, J. L. Schönberger, J. V. de Miranda Cardoso, J. Reimer, J. Harrington, J. L. C. Rodríguez, J. Nunez-Iglesias, J. Kuczynski, K. Tritz, M. Thoma, M. Newville, M. Kümmerer, M. Bolingbroke, M. Tartre, M. Pak, N. J. Smith, N. Nowaczyk, N. Shebanov, O. Pavlyk, P. A. Brodtkorb, P. Lee, R. T. McGibbon, R. Feldbauer, S. Lewis, S. Tygier, S. Sievert, S. Vigna, S. Peterson, S. More, T. Pudlik, T. Oshima, T. J. Pingel, T. P. Robitaille, T. Spura, T. R. Jones, T. Cera, T. Leslie, T. Zito, T. Krauss, U. Upadhyay, Y. O. Halchenko, and Y. Vázquez-Baeza, “SciPy 1.0: fundamental algorithms for scientific computing in Python”, *Nat. Methods* **17**, 261 (2020).

[110] J. D. Hunter, “Matplotlib: A 2D Graphics Environment”, *Comput. Sci. Eng.* **9**, 90 (2007).

[111] E. W. Weisstein, *”Spherical Coordinates.” From MathWorld — A Wolfram Web Resource — https://mathworld.wolfram.com/SphericalCoordinates.html.*